Design of a Hermetically Sealed MEMS Resonator with Electrostatic Actuation and Capacitive Third Harmonic Sensing

By

Eric B. Newton

B.S. Engineering Physics and Mathematics
University of Wisconsin – Madison 2009

Submitted to the Department of Mechanical Engineering
in Partial Fulfillment of the Requirements for the Degree of

Master of Science in Mechanical Engineering

at the

MASSACHUSETTS INSTITUTE OF TECHNOLOGY

February 2012

Signature of Author: _____
Department of Mechanical Engineering
January 20, 2012

Certified by: _____
Carol Livermore
Visiting Scientist
Thesis Supervisor

Accepted by: _____
David Hardt
Professor of Mechanical Engineering
Chairman, Committee for Graduate Students

Design of a Hermetically Sealed MEMS Resonator with Electrostatic Actuation and Capacitive Third Harmonic Sensing

By

Eric Newton

Submitted to the Department of Mechanical Engineering

on January 20, 2012, in Partial Fulfillment of the

Requirements for the Degree of Master of Science in

Mechanical Engineering

ABSTRACT

A microscale beam resonator has been designed and fabricated for use as a modular pressure sensor for vacuum applications. The device dimensions have been optimized to provide measurable signals with low noise. Electrostatic actuation and sensing are both performed using only one pair of electrodes. The motion of the cantilever changes the capacitance of the actuation electrodes at a frequency three times that of the actuation signal. This method allows the desired motion to be picked out using a lock-in amplifier with minimal interference from other unwanted signals such as parasitic leakage and noise. Unlike previous work, packaging and electrical contacts have been integrated into the fabrication to create a hermetically sealed device that can easily be incorporated into other MEMS designs.

Most resonators operate in vacuum because air damping at higher pressures greatly decreases both resonant frequency and quality factor. This loss is directly related to the pressure of the surrounding air, and therefore has been used in this design to measure the pressure. While the relationship is not linear, it is one-to-one. This means that once the device has been characterized, pressure can be determined uniquely over a range from atmospheric pressure down to ~10^{-3} Torr.

The device was fabricated from two SOI wafers using standard wafer processing techniques. This means that unlike previous work, it can be readily integrated into other designs via wafer bonding. A single access port on the base provides a connection between the otherwise hermetically sealed sensor and other devices. To prevent squeeze film damping from limiting the motion of the beam, the cantilever tip has been perforated with an array of holes and a cavity was etched above where the cantilever will oscillate. Electrical contact can easily be made with the device as fabricated, so no additional packaging is necessary.

While the fabricated devices are hermetically sealed, resonance was never detected due to a combination of factors including: poor wafer bonding, parasitic leakage, a Schottky barrier at one terminal and a design error that led to an unexpectedly high frequency and quality factor. Modifications to the current design are proposed that should eliminate these problems in the next iteration.

Thesis Supervisor: Carol Livermore

Title: Visiting Scientist

Acknowledgements

I feel quite lucky to have had such a gratifying Master's experience. Throughout the last two and a half years, I have been surrounded by people who were both very knowledgeable and happy to offer their advice on all sorts of questions. I would like to thank them for their support – I would not have finished without their help.

First and foremost, I would like to thank my adviser, Professor Carol Livermore, who has been a great mentor and friend. She has provided me with constant support and guidance from the moment I stepped onto campus. Her cheerful demeanor made our weekly meetings a pleasure, and she was always happy to discuss my problems in my research, both large and small. I would also like to thank my new adviser Professor Martin Schmidt for taking me into his research group for my PhD and offering sage advice to help me finish this project.

I would also like to thank all of my labmates for their friendship and support throughout the last two years. Aalap, Feras, Frances, Gunjan, Lei and Nader: you have always been willing to listen to me vent frustrations with research and life, and I have greatly enjoyed our many birthdays, group dinners and especially the trip to Acadia. Thank you Feras and Lei for your advice on microfabrication. And a particularly large thank you to Aalap, who collaborated with me on the micropump project, for our long discussions about both of our projects.

I also thank Professor Tayo Akinwande, Dr. Hanqing Li and Dr. Luis Velasquez-Garcia and the rest of the micropump team. They provided advice and technical help throughout the design, fabrication, and testing process. I also want to thank the MTL staff for training in the clean room. I am particularly thankful to Dennis Ward and Bernard Alemariu, who gave crucial insight into my fabrication process and helped troubleshoot problems when processing did not go as planned. I would like to thank Dr. Nicki Watson and the Whitehead Institute for allowing me to use their Critical Point Drier. My devices could not have been fabricated without her help. The project was financially supported by Professor Livermore, the Mechanical Engineering Department of MIT (through a one year Presidential Fellowship) and DARPA.

Finally, I'd like to acknowledge my parents, sister brother and girlfriend Rocio for the continuous moral support they have provided me with throughout this process. I always look forward to talking with and seeing you guys, and I could not have made it through these last two years without you all.

Table of Contents

List of Figures

List of Notation

Q	Quality Factor [-]
U_s	Energy stored per cycle [J]
U_d	Energy Dissipated per cycle [J]
ω_0	Angular frequency or resonator[rad/s]
Q_{clamp}	Quality factor due to clamping and support losses [-]
γ_n	Constant of proportionality in $Q_{clamp}$for nth mode of vibration [-]
L	Length of cantilever beam [m]
t	Thickness of cantilever beam [m]
E	Young's modulus [Pa]
E_1	Elastic modulus [Pa]
E_2	Loss modulus [Pa]
Q_{vol}	Volumetric quality factor [-]
$Q_{surface}$	Surface quality factor [-]
w	Width of cantilever beam [m]
δ	Thickness of surface layer for $Q_{surface}$ [m]
E_{1s}	Elastic Modulus for $Q_{surface}$[Pa]
E_{2s}	Loss Modulus for $Q_{surface}$ [Pa]
Q_{TED}	Thermoelastic Dissipation Quality Factor [-]
ξ	Constant used in Q_{TED} [-]
C_p	Specific heat of silicon at constant pressure [J/K]
ρ	Density of silicon [kg/m^3]
T	Temperature [K]
α_T	Coefficient of thermal expansion [m/K]
k_{Si}	Thermal conductivity of silicon [W\(m-K)]
Kn	Knudsen number [-]
λ	Mean free path [m]
L_c	Characteristic Length [m]
k_B	Boltzmann Constant [J/K]
d	Diameter of molecules [m]
p	Pressure [Pa]
$Q_{p,viscous}$	Pressure quality factor for viscous regime [-]
μ	Dynamic viscosity [Pa-s]
M	Molar mass of gas surrounding beam [kg/mol]
R	Ideal Gas constant [J/(mol-K)]
$Q_{p,molecular}$	Pressure quality factor for molecular regime [-]

Q_{total}	Sum of all quality factors [-]
$F_{damping}$	Damping force [N]
c	Coefficient of damping [N-s/m]
v	Velocity [m/s]
F_{sphere}	Damping force on a sphere [N]
F_{dish}	Damping force on a dish [N]
r	Radius [m]
c_{beam}	Damping coefficient of beam [N-s/m]
V	Volume [m^3]
p_a	Atmospheric pressure [Pa]
a	Radius of cells in perforated plate [m]
b	Radius of holes in perforated plate [m]
g	Current gap between cantilever and base electrode [m]
A_c	Area of annular region in each cell of perforated plate [m^2]
β	Ratio of b/a [-]
N	Number of holes in perforated plate [-]
c_{sqfilm}	Squeeze film damping of perforated plate [N-s/m]
ξ_β	Function of β used in calculation of c_{sqfilm} [-]
F_e	Electrostatic force [N]
ϵ_0	Permittivity of free space [F/m]
A	Area of actuation for cantilever [m^2]
V	Actuation voltage [V]
g	Current gap [m]
U_e	Electric potential energy [J]
k	Cantilever spring stiffness [N/m]
k_{system}	Stiffness of entire system [N/m]
x	Displacement[m]
γ	Damping factor [1/s]
F_0	Magnitude of oscillatory force [N]
A_0	Magnitude of oscillatory acceleration [m/s^2]
Ω	Angular frequency of oscillatory force [rad/s]
m	Mass [kg]
x_s	Specific solution to displacement differential equation [m]
X_0	Magnitude of forced displacement [m]
θ	Phase of forced oscillation
X_{max}	Maximum forced displacement (at resonance) [m]
Ω_{max}	Actuation frequency corresponding to max forced displacement

	[rad/s]
u	Beam displacement [m]
I	Second moment of inertia [m^4]
F_e'	Electric force per unit length [N/m]
$\phi_n(x)$	Spatial dependence of the nth mode of vibration [m]
$\eta_n(t)$	Time dependence of the nth mode of vibration [s]
α_m	Normalization constant for mth mode of vibration [-]
δ_{mn}	Kronecker delta [-]
κ_n	Eigenvalues for the nth spatial mode of vibration [-]
m_n	Modal mass for the nth mode of vibration [kg]
c_n	Modal damping for the nth mode of vibration [N-s/m]
k_n	Modal stiffness for the nth mode of vibration [N/m]
q_n	Modal force for the nth mode of vibration [N]
l	Actuation length [m]
$\delta(x)$	Dirac delta function [-]
V_{AC}	Magnitude of actuation voltage [V]
U_{max}	Maximum beam displacement [m]
α	Angle of twist per unit length [rad/m]
T	Net torque on beam [N-m]
G	Shear Modulus [Pa]
R	Resistance [Ω]
ν	Poisson Ratio [-]
ρ_{ij}	Resistivity tensor [Ω-m]
J_i	Current density in the i direction [A/m^2]
ρ_{ij}^0	Resistivity tensor of unstressed material [Ω-m]
π_{ijkl}	Piezoresistivity tensor [Ω-m/Pa]
σ_{kl}	Stress tensor [Pa]
π_l	Lateral piezoresistive coefficient [1/Pa]
π_t	Transverse piezoresistive coefficient [1/Pa]
σ_l	Lateral stress [Pa]
σ_t	Transverse stress [Pa]
M	Bending moment in cantilever [N-m]
y	Perpendicular distance from neutral axis [m]
R_{square}	Resistance for a square of material [Ω]
R'	Total resistance over doped region of piezoresistor [Ω]
R'_{path}	Integrated resistance of one path of piezoresistor [Ω]

w_{path}	Width of piezoresistor path [Ω]
x_1	Starting x value for resistive path [m]
x_2	Ending x value for resistive path [m]
y_1	Starting y value for resistive path [m]
y_2	Ending y value for resistive path [m]
R_{lead}	Approximate resistance of one path [Ω]
$R_{isolation}$	Isolation between neighboring leads [Ω]
C	Capacitance [F]
Q_e	Charge [C]
$i(t)$	Current [A]
$i_3(t)$	Third harmonic current [A]
C_0	Un-actuated capacitance of cantilever [F]
u_n	Beam deflection due to damping noise [m]
C'	Capacitance with damping noise variations [F]
v_n	Johnson noise [V]
i'	Current with Johnson noise contribution [A]
u_g	Displacement due to gravity [m]
a_g	Gravitational acceleration [m/s^2]
F_{grav}	Gravitational force on beam per unit length [N/m]
σ	Squeeze number [-]
ω_{max}	Maximum allowable resonance frequency [rad/s]
R_1	Resistance of first electrode [Ω]
R_2	Resistance of second electrode [Ω]
Z_{res}	Impedance of resonator path [Ω]
R_{p1}	Resistance of first electrode [Ω]
C_{p1}	First parasitic capacitance [F]
C_{p2}	Second parasitic capacitance [F}
C_{p3}	Third parasitic capacitance [F}
Z_{over}	Impedance of parasitic path over top through the cap [Ω]
R_{p2}	Second parasitic resistance [Ω]
C_{p4}	Fourth parasitic capacitance [Ω]
Z_{around}	Impedance of parasitic path around via through device layer [Ω]
C_{p5}	Fifth parasitic capacitance [F]
Z_{under}	Impedance of parasitic path around via through bulk silicon [Ω]
$i_2(t)$	Second Harmonic Current [A]
$f_2(V_{AC})$	Scaling function for the second harmonic for biased actuation [-]

$f_3(V_{AC})$	Scaling function for the third harmonic for biased actuation [-]

1 Introduction

Interest in Micro Electromechanical Systems (MEMS) has been growing, with increasing applications for MEMS accelerometers, strain gauges, and microphones. At the interface with biology, BioMEMS have been able to make their way into medical applications from as basic as biochemical sensing to a miniaturized polymerase chain reaction (PCR) device used to amplify DNA segments [1]. Many of these technologies have been made possible by leveraging the techniques and materials used to make integrated circuits (ICs), such as photolithography, thin film deposition, doping and many varieties of dry and wet chemical etches. These devices, like ICs, are fabricated on the wafer level with many chips per wafer, allowing expensive processes can be spread out over a large number of units and decreasing the total cost per device. Additionally, since MEMS use many of the same processes as ICs, electronics can be integrated on chip.

1.1 Motivation for Pressure Sensor

Many microscale devices, such as resonators, require a vacuum environment to operate or damping will lower the quality factor and resonance frequency [2], [3]. Other devices, such as a proposed chip-scale mass spectrometer [4], gas chromatograph [5], or functionalized resonant sensors [6] take gas samples from the environment at higher pressure, and decrease the pressure, often to vacuum levels, before measuring the samples. It is useful to know the pressure inside these devices in order to estimate the damping on the resonators and resonant sensors or to determine when the pressure has been pumped down sufficiently for measurements.

The objective of this project is to design a simple resonant pressure sensor for integration with other MEMS for vacuum applications, such as those described above. In particular, this device is intended for use in a multi-stage microscale vacuum pump, and will be used to determine when to transition from one stage to the next. The metrics for a successful design, derived from the overall requirements for the vacuum pump, are:

- Minimum pressure sensing range from: 760 Torr – 1 Torr
- Self-contained (no large external actuators or sensors)
- Fabricated with standard clean room procedures (to facilitate integration)
- Low power (<0.25 W)
- Low volume (<0.5 cm^3)

1.2 Review of Pressure Sensing with MEMS Resonators

Applications for beam resonators are as varied as varied as very high frequency (VHF) filters [7], reference frequency sources for CMOS circuits [8], and many types of sensors. Some examples of these sensors are: very sensitive forces can be measured with atomic force microscopy and similar techniques with attonewton sensitivity [9], inertial balances can measure mass down to the change of a single atom [10], [11], many types of biological and chemical agents [6], and (the focus of this section) pressure [12–20].

All of these sensors rely on the measured quantity; whether that is forces, mass, chemicals, or pressure, coupling into the motion of the beam and changing the resonance frequency. Since the change in the resonance frequency decreases in magnitude as the quality factor (Q) increases, the quality factor is often used as the measurement parameter. Resonant sensors are more precise at higher frequencies and Q values. Fixed-free microscale beam resonators with Q values as high as 177,000 at frequencies of 19kHz have been reported [21], though much higher frequencies [22] and higher Q values [20] have been achieved for other geometries.

There are many ways to measure pressure with MEMS resonators. Sensing generally falls into two categories:

1) The resonator is isolated in vacuum from the target pressure, usually by a deformable membrane. Changes in support structure cause a change in the beam, usually either increasing the stress or changing the shape, causing a shift in resonance frequency [15–17], [23].
2) The pressure can be sensed directly as the pressure changes affect the damping on the beam and thus the resonance frequency. This works well for low pressure measurement [12], [13], [20].

Several of the more prominent designs from the literature are described in this section.

Consider one of these membrane sensors [15] in particular. The resonator is fabricated on a thin membrane with vacuum on the resonant side and the target pressure on the back side. The resonator consists of a block mass suspended on four straight flexures attached to the membrane. Actuation and sensing is achieved through comb capacitors on all four sides of the mass (orthogonal sense and drive). As the pressure increases, the membrane deforms and the tensile stress in the flexures increases, causing the resonance frequency to increase. This design works well for large pressures, but does not work well for low pressures (below ~0.1 bar) because the magnitude of the pressure change (and thus the strain) is too low.

In a similar idea, another plate resonator pressurizes the inside of a hollow plate with the exterior at vacuum [14]. As the internal pressure changes, the plate deforms and the resonance frequency changes.

There are many types of resonant sensors that measure pressure directly through air damping and its effect on quality factor. Several canonical examples will be discussed below.

A common pressure sensor involves a simple cantilever beam vibrating in the direction of to its thinnest dimension [2], [12], [13].

The simplest of these devices [2] was fabricated a two-step process in which the beams are patterned and then undercut using KOH to leave a large cavity beneath the resonators. Actuation was performed externally by vibrating the entire chip with a speaker, and sensing is performed optically with a laser focused on the tip of the beam.

A similar design was created in on an SOI wafer in order to prevent thin film stresses from affecting the beams [12]. In this case the actuator is an external piezoelectric disk, and the motion is optically sensed by reflecting a laser off of the tip.

In another design cantilevers were created on an SOI wafer that vibrate laterally (in the plane of the device layer) [13]. One set of electrodes wired bonded directly to the device layer allow electrostatic actuation and capacitive sensing utilizing a third harmonic sensing method discussed in [24] and in more detail in Section 3.2.3.1 later in this thesis. A trench was etched in the device layer down to the buried oxide to electrically isolate the cantilever electrode from the other actuation electrode.

Another type of resonant frequency-based pressure sensor employs the torsional mode of vibration, such as in [20]. A large plate is suspended on two tethers and rotates on the supports (like a see-saw). The device was actuated by an external lateral excitation created by a piezoelectric, and the motion was sensed optically. Pure torsion causes no volume change, lowering the internal losses due to resonance. This allows a larger pressure sensing range.

A summary of these sensors is shown below in Table 1-1 below.

Table 1-1 - Resonant Pressure sensor summary

Description of Sensor	Topology	Actuation	Sensing	Pressure Range	Sensitivity
Diaphragm resonator [15]	Tethered plate on a pressurized diaphragm	Electrostatic (comb capacitor)	Electrostatic (comb capacitor)	~0.1bar-3.5bar	8.8kHz/bar
Simple Cantilever Resonator [2]	Fixed-free cantilever beam	Speaker	Optical	1 Pa - 100kPa	Not listed, varies with pressure
Stress free Cantilever Resonator [12]	Fixed-free cantilever beam	External Piezoelectric	Optical	0.1Pa - 100kPa	Not listed, varies with pressure
Electrostatic Cantilever Resonator [13]	Fixed-free cantilever beam	Electrostatic	Electrostatic "third harmonic sensing" [24]	0.1Pa – 100kPa	Not listed, varies with pressure
Torsional Resonator [20]	Rotating plate on tethers	External Piezoelectric	Optical	0.1mbar – 1bar	Not listed, varies with pressure

External actuators, such as piezoelectrics or speakers, and optical sensing are quite common because they require no additional fabrication steps to integrate.

1.3 Proposed Design

The operation principle for the proposed device is simple, and similar to previous resonant pressure sensors [2], [12], [13], [20]. A cantilever beam is actuated at resonance. The damping on the beam, and the corresponding quality factor, are directly dependent on the damping over a range of pressures from atmospheric down to 10^{-2} Torr. At a given pressure, one must simply match the current resonant frequency to the corresponding pressure.

Several innovations set this device apart from other resonant pressure sensors. It uses the same electrostatic actuation and capacitive third harmonic sensing as [13], [24], but in the proposed design the resonant cantilever is contained in a hermetically sealed cavity with a single access hole to connect it to the target pressure. Additionally, the entire device is

fabricated with standard wafer processing techniques and can easily be integrated into other designs through wafer bonding.

1.4 Outline of Thesis

This thesis presents a MEMS sensor that detects pressure through changes in the quality factor of a resonant cantilever beam. The test chamber is hermetically sealed with a single set of electrodes for actuation and sensing. The different stages involved in the development of the device are discussed, starting with modeling and design, then fabrication, testing, and finally a new proposed design to overcome the shortcomings of the first attempt.

In this chapter, the motivation for a modular pressure sensor was discussed.

Chapter 2 lays out the relationship between damping and quality factor. Many loss factors are discussed, including clamping losses, bulk dissipation, surface losses, and thermoelastic dissipation. Damping losses at a range of pressures are discussed and the viscous damping coefficient for a resonant cantilever beam (with holes) is derived and analyzed.

Chapter 3 compares many actuation and sensing methods before justifying the selection of electrostatic actuation and sensing. Dynamics of a forced spring-mass-damper are analyzed, and compared to the full motion of an oscillating cantilever beam based on the Euler-Bernoulli beam equation. Several constraints and assumptions arising from physical and fabrication limitations are analyzed to reduce the number of independent device parameters. A summary of the device design is presented.

Chapter 4 describes the fabrication process. The wafer level die layout is discussed, along with the purpose of each device variation. The process flow for each stage of fabrication is discussed, along with relevant masks and cartoons showing the device cross-sections at each major processing step.

Chapter 5 discusses the test setup and experimental procedure. The test jig, pressure control system and electronic measurement system are described. Experimental data are presented, along with proposed explanations for the failure of testing to detect resonance. Problems included: device layer peeling, parasitic leakage, rectification of the actuation signal, and the presence of a significant third harmonic component in the actuation source.

Chapter 6 proposes a new design aimed at removing the problems discovered in the first build. Suggestions include: improved bonding procedures, several design modifications that improve isolation between terminals and lower the resonance frequency of the beam, and adding metal contacts. A summary of the new design is presented.

2 Operation Principle – How Quality Factor Relates to Damping

In this section, air damping and other important loss factors for a vibrating cantilever beam are discussed in detail, with a focus on how pressure affects the damping losses in both the viscous and molecular regimes. Viscous damping on the freely oscillating beam and squeeze film damping in the narrow actuation gap are also discussed.

2.1 Pressure Dependence Predictions

Quality factor (Q) is commonly used to describe the efficiency of a resonator. Q is defined as

$$Q = 2\pi \frac{U_s}{U_d} \tag{2.1}$$

where U_s is the energy stored per cycle and U_d is the energy dissipated.

A resonator with quality factor of ½ is critically damped, indicating that the motion will not oscillate but rather exponentially decay. Lower Q values indicate more damping (and faster decay), while resonators with higher Q will oscillate before coming to rest.

For measurement in the lab, a more useful definition of Q valid for higher frequencies is

$$Q = \frac{\omega_0}{\Delta\omega} \tag{2.2}$$

where ω is the damped resonance frequency and $\Delta\omega$ is the range of frequencies for which the output is at least half the maximum (also called full width at half max).

Many factors contribute to the overall energy loss [12], [25]: clamping/support losses, bulk dissipation, surface losses, thermoelastic dissipation (TED), and most importantly at high pressures – air damping. Each of these loss mechanisms will be described below.

2.1.1 Clamping and support losses

The supporting region around a resonator is never perfectly rigid. The motion of the resonator can couple into the surrounding region and cause energy losses. For a fixed-free cantilever beam this loss can be analytically determined as

$$Q_{clamp} = \gamma_n \left(\frac{L}{t}\right)^3 \tag{2.3}$$

where γ is a constant for the nth vibrational mode, L is the length of the beam and t is the thickness. In our case we will be considering the first mode, where γ_1 = 2.232 [25].

2.1.2 Bulk Dissipation

No real material is perfectly elastic. The complex Young's modulus $E = E_1 + iE_2$ takes that into account, where E_1 is the material stiffness (elastic portion) and E_2 is the loss modulus (viscous portion). E_2 represents the energy lost through bulk deformation of the volume of the material, usually manifested as heat. The volume quality factor can be written as [25]

$$Q_{vol} = \frac{E_1}{E_2}. \tag{2.4}$$

The loss modulus for silicon is very low, making it an excellent resonator material [18].

2.1.3 Surface Losses

At the surface of the resonator the atomic lattice is disrupted and there may be surface contamination. There is always a thin native oxide on silicon. This doesn't store much energy, but it can noticeably increase the energy dissipation. If we consider a layer of thickness δ and complex Young's modulus $E_s = E_{1s} + iE_{2s}$ then the quality factor due to surface losses from the thin film would be [25]

$$Q_{surface} = \frac{wt}{2\delta(3w+t)}\frac{E_{1s}}{E_{2s}}. \tag{2.5}$$

2.1.4 Thermoelastic Dissipation

Thermoelastic dissipation (TED) can also play a significant role. Stretching causes material to cool down while compression causes it to heat up. Oscillations will therefore create temperature gradients that cause irreversible heat flow in the resonator. The TED contribution can be calculated as follows [25]

$$Q_{TED} = \frac{C_p\rho}{E\alpha_T^2 T}\left[\frac{6}{\xi^2} - \frac{6}{\xi^3}\frac{\sinh\xi + \sin\xi}{\cosh\xi + \cos\xi}\right], \tag{2.6}$$

$$\xi = w\sqrt{\frac{\rho C_p \omega_o}{2k_{Si}}}, \tag{2.7}$$

where α_T, C_p and k_{Si} are the coefficient of thermal expansion, specific heat and thermal conductivity of the cantilever material, T is the absolute temperature (in K) of the air, and ω_0 is the resonance frequency of the cantilever.

2.1.5 Fluid Damping Losses

The amount of damping depends greatly on the pressure of the air surrounding the vibrating beam. This leads to a pressure dependence in the quality factor for the beam. The

Knudsen number Kn is a useful way to separate various damping mechanisms at different pressures. It is defined as

$$Kn = \frac{\lambda}{L_c} = \frac{k_B T}{\sqrt{2}\pi d^2 p L_c} \tag{2.8}$$

where λ is the mean free path of a the gas, L_c is the relevant length scale (width of the cantilever beam or thickness of the gap), k_B is the Boltzmann constant, d is the diameter of the molecules, and p is the ambient pressure.

For $Kn < 0.1$, molecules are close enough together that the gas is dominated by inter-molecular interactions. This is known as the viscous regime. Under these conditions, the fluid can be modeled as a continuum and damping can be determined using the Navier-Stokes equation. The no-slip boundary condition is still valid.

There is no closed form solution for a vibrating cantilever beam. However, a common approximation is to model the beam as a row of oscillating beads and use the standard damping coefficient for a sphere (neglecting sphere-sphere interaction). This gives a quality factor of [12]

$$Q_{p,viscous} = \frac{2\rho_b t w^2 \omega_o}{6\mu w + \frac{3}{2}\pi w^2 \sqrt{2\mu \frac{M}{RT}\omega_o p}} \tag{2.9}$$

where μ is the dynamic viscosity of the surrounding gas, M is the molar mass of the gas and R is the gas constant. It can be seen from the equation that for larger pressures a $p^{-1/2}$ term dominates, and as pressure decreases $Q_{viscous}$ approaches a constant value.

At low pressure, when $Kn > 10$, the molecules rarely collide and they need to be modeled using the kinetic theory of gases. In this regime, air damping has a negligible effect on the cantilever motion. All energy losses can be attributed to a momentum transfer between the vibrating beam and colliding molecules. The quality factor in this rarified gas is [12]

$$Q_{p,molecular} = \frac{\rho_b t \omega_o}{4}\sqrt{\frac{\pi}{2}}\sqrt{\frac{RT}{M}}\frac{1}{p}. \tag{2.10}$$

Note that there is still a pressure dependence because there are simply fewer molecules to hit at lower pressures.

In between the viscous and the free molecular regimes (pressures where $0.1 < Kn < 10$), quality factor is influenced by both momentum transfer and viscous losses.

The overall Q of the system can be determined through summing the inverses of all contributing quality factors, as follows

$$\frac{1}{Q_{total}} = \frac{1}{Q_{pressure}} + \frac{1}{Q_{clamp}} + \frac{1}{Q_{volume}} + \frac{1}{Q_{surface}} + \cdots = \sum_i \frac{1}{Q_i}. \tag{2.11}$$

It can easily be seen that the smallest Q values will have the largest impact. From atmospheric pressure down to around 10^{-2} Torr, losses due to damping dominate. At pressures below 10^{-3} Torr damping continues to decrease but other losses intrinsic to the resonator design (volume, surface, clamping, TED, etc) become more important. This can be seen in Figure 2-1 below.

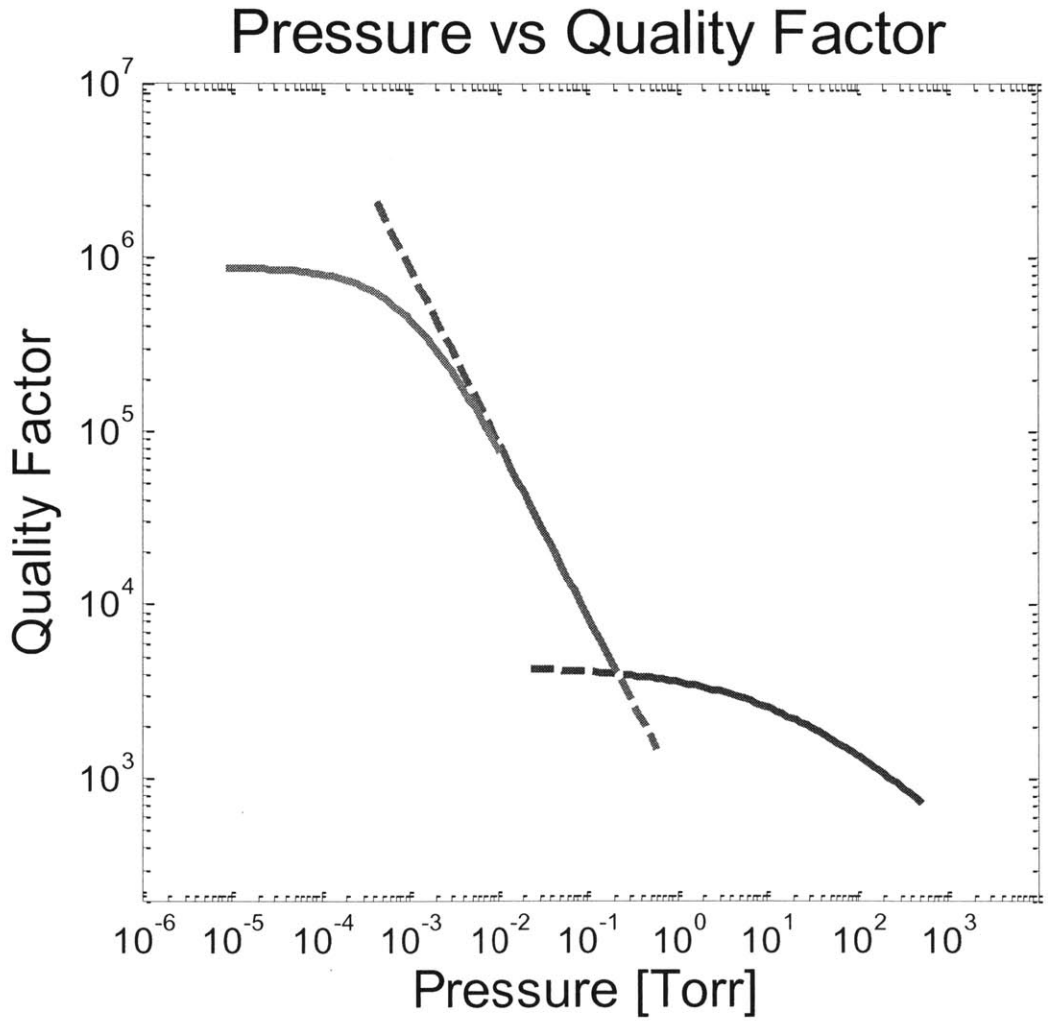

Figure 2-1 Pressure dependence of Quality Factor. Blue indicates the viscous regime, green is the free molecular regime and at low pressures, red indicates that intrinsic effects (clamping, volume, surface, TED, etc) dominate pressure loss. The transition between viscous and molecular damping has not been shown, though a smooth transition between 1 Torr and 10^{-1} Torr is expected.

2.2 Damping on a cantilever beam

Damping on a resonant cantilever comes from two sources: viscous drag (resistance to motion from the surrounding fluid) and squeeze film damping (air "trapped" between cantilever and a nearby surface).

2.2.1 Drag

First, we will consider drag. The surrounding fluid exerts a force on an object because of the velocity difference between the boundary layer at the object's surface and the fluid further away. The damping force is proportional to the velocity of the object, and is generally written with a damping coefficient c as follows

$$F_{damping} = cv\,. \tag{2.12}$$

The drag force can be analytically determined for several basic shapes in an infinite viscous fluid, such as a sphere

$$F_{sphere} = 6\pi\mu r v\,, \tag{2.13}$$

or a flat disk

$$F_{disk} = 16\mu r v\,, \tag{2.14}$$

where in both cases μ is the fluid viscosity, r is the radius and v is the relative velocity of the object to the surrounding fluid.

It should be noted that there is not closed form solution for drag damping for a rectangular cantilever, but a common approximation [26] is described here. We can model the cantilever beam as a series of disks with a diameter equal to the width of the beam, as shown in Figure 2-2.

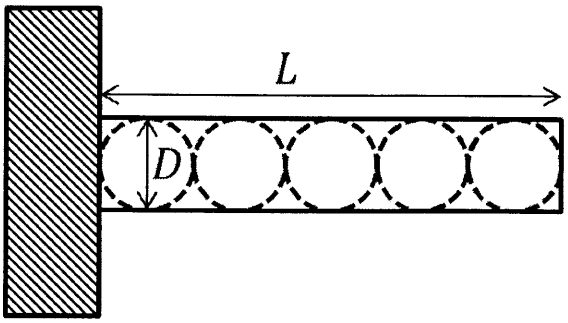

Figure 2-2 - Visualization of the disk approximation for a vibrating cantilever beam.

The drag coefficient of a single disk is given by

$$c_{disk} = 8\mu D\,, \tag{2.15}$$

where μ is the dynamic viscosity of the fluid, and D is the diameter of disk. The number of disks over the entire length is L/D, so the drag coefficient of the beam can be approximated as

$$c_{beam} = 8\mu L\,. \tag{2.16}$$

2.2.2 Squeeze Film Damping

When the gap between two moving surfaces is small, fluid in between the surfaces must flow into or out of the gap as the distance between the surfaces changes. The resistance to this fluid motion is called squeeze film damping.

The pressure distribution for a pair of circular plates informs the analysis for the actual 3D plates. If we assume for simplicity that the fluid is incompressible (which is reasonable for small deflections at high frequencies), then the rate of change of a volume element V is 0

$$\frac{dV}{dt} = 0 = \pi r^2 \frac{dg}{dt} + 2\pi r g \frac{dr}{dt} \tag{2.17}$$

where r is the radius from the center, g is the gap between the plates, and t is time. The radial velocity is

$$\frac{dr}{dt} = -\frac{1}{2}\frac{r}{g}\frac{dg}{dt}. \tag{2.18}$$

The Bernoulli equation can be used to determine the pressure

$$p(r) = p_a + \frac{1}{8}\rho\left(\frac{r}{g}\frac{dg}{dt}\right)^2 \tag{2.19}$$

where p_a is atmospheric pressure. The pressure increases as r^2, with a maximum in the center of the plate. This makes sense: it is clear that the fluid at the edge of the plate is unimpeded and can move freely, while the fluid at the center must push against all of the fluid under the plate. Additionally, the magnitude of the maximum pressure increases with the vertical velocity of the plate squared as well. This effect can dominate the motion for large plates, especially if they are moving rapidly.

To help mitigate squeeze film damping, large plates are often perforated. This allows air to flow from the front side to the back and prevents large pressure from building up in between the surfaces. To model the pressure distribution for a perforated plate, the surface is broken into annular cells as shown in Figure 2-3.

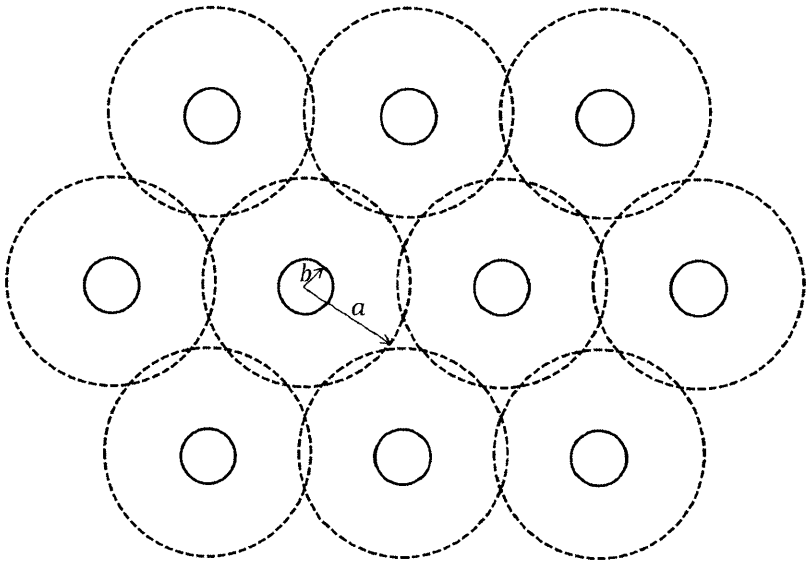

Figure 2-3 - Approximation of a perforated plate with annular cells

Since the edge of the annulus is not actually an edge in the plate, special boundary conditions must be used. The pressure at a hole is low, because there is no resistance to flow, while the pressure is greatest at the edge of a cell. Symmetry between cells allows us to set the slope of the pressure to 0 at this point. Thus

$$P(b) = 0 \text{ and} \tag{2.20}$$

$$\frac{dP}{dr}(a) = 0. \tag{2.21}$$

The pressure distribution can be solved in each annulus by considering the results from before. Integrating over the pressure field gives a squeeze film force, from which the drag coefficient can be calculated as follows

$$c_{sqfilm} = \frac{3\mu A_c^2}{2\pi g^3}(4\beta^2 - \beta^4 - 4\ln(\beta) - 3)N \tag{2.22}$$

where A_c is the area of each annular cell, and $\beta = b/a$, and g is the gap height and N is the number of holes. It is worthwhile to compare the relative magnitudes of the damping coefficients. Taking the ratio, with the area for A substituted in the perforated plate equation and $\xi_\beta = (4\beta^2 - \beta^4 - 4\ln(\beta) - 3)$ we get

$$\frac{c_{sqfilm}}{c_{beam}} = \left(\frac{3\mu\pi^2 a^4}{2\pi g^3}\,\xi_\beta N\right)\left(\frac{1}{8\mu L}\right) = \frac{3\pi}{16}\,\xi_\beta N\left(\frac{a^4}{g^3 L}\right) \tag{2.23}$$

where

$$N = \left(\frac{1}{\pi a^2}\right) lw\,. \tag{2.24}$$

The ratio simplifies to

$$\frac{c_{sqfilm}}{c_{beam}} = \frac{3}{16}\,\xi_\beta \left(\frac{lwa^2}{g^3 L}\right). \tag{2.25}$$

The spacing between holes (and thus a) is determined by deciding the amount of the plate that should be holes

$$ratio_{holes} = \frac{A_{holes}}{A_{plate}} = \frac{\pi b^2}{\pi a^2} = \frac{b^2}{a^2} \tag{2.26}$$

With the inner radius (b) set to the minimum (safely) resolvable size (about 2μm radii holes),

$$a = \sqrt{ratio_{holes}}\,b\,. \tag{2.27}$$

An estimate of this ratio can be made by choosing reasonable dimensions based on fabrication and design limitations. The gap is limited to 2.5 μm because stress in the sacrificial oxide causes it to peel for thicker films. The ratio of holes to actuation area must be kept small to ensure that the proper actuation force is applied. For this estimate, the ratio will be assumed to be 10. Larger numbers of small holes decrease the squeeze film damping further. However it is difficult to DRIE etch narrow holes. Let b = 2 μm (⇒ a = 6.3 μm), which is small, but safely etched. For this ratio of b/a, $\xi_\beta \approx 2$. Finally, to ensure beam-like behavior, $l = w = L/5$. With these substitutions,

$$\frac{c_{sqfilm}}{c_{beam}} \approx \frac{24L}{625} \tag{2.28}$$

where the $24/625$ factor has units of μm^{-1}. All devices considered have $L \in$ [500 μm, 1500 μm], which places the damping ratio roughly ϵ [20, 55]. This suggests that damping is dominated by the squeeze film effects at the end of the beam. This means that if the squeeze film damping is low enough that it won't impede the motion of the beam, then overall damping won't either. This does not mean that damping will have a negligible effect on the quality factor, but rather that it doesn't have an undue effect on the beam's motion.

The gap can only be made smaller and the holes can only get larger (see the fabrication limits above), both of which increase the squeeze film damping. Similarly, increasing l increases

the area (and thus N), while decreasing l decreases the output signal, and as such squeeze film damping will only become more prominent.

3 Design and Optimization

With a general design in mind (a resonant cantilever beam in a hermetically sealed cavity) and detection principle (quality factor is uniquely determined by the surrounding pressure), it remains to be determined: 1) how to actuate the cantilever beam and 2) how to sense its motion.

3.1 Assessment of Actuation Methods

There are many possible methods for actuating a cantilever beam, each coming with its own set of benefits and limitations as will be discussed below. Beyond assessing whether the actuation method would work for this design, if this pressure sensor is to be combined with other MEMS devices, actuation should occur within the device. Large external equipment should not be required, such as lasers or large external actuators. However, most MEMS devices are electrically powered and often have signal processing, so these external features are allowed.

3.1.1 Thermal, Magnetic and Piezoelectric Actuation

Thermal actuation typically involves a beam of two materials with different coefficients of thermal expansion. Since they are attached, neither material can expand at its desired rate, leading to a stress distribution that causes the beam to bend. This is commonly used in thermostats, but the slow heating/cooling time prohibits large scale use on the macro scale. However, microscale devices have much larger surface area to volume ratios, and can heat and cool much more quickly, with a maximum frequency on the order of 3kHz [27]. Actuation is often achieved through resistive heating, allowing actuators to be easily fabricated along with existing electronics. However, even the increased frequency of microscale cooling does not create a resonator that is fast enough for the design parameters.

A variant on thermal actuation involves heating the beam with a laser, rather than resistively. This has the added benefit that it can be integrated into any optical sensing techniques without any added equipment. However, it places some restrictions on the fabrication process because there must be an optical path to the cantilever, in addition to the switching time limitations mentioned above.

Magnets can in principle be used to actuate small structures. They can achieve large forces. However commercial magnets are too large and difficult to integrate into MEMS, and fabricating magnets in the clean room is very difficult. Fabricating an electromagnet on a wafer has been done [28] but is quite challenging, while an external field defeats the purpose of a self-contained device. Additionally, the switching time for MEMS electromagnetic actuators is too low, with an estimated values similar to thermal bimorphs (<3kHz) [27].

Piezoelectric actuation is also commonly used in MEMS. By applying a voltage across a piezoelectric material, extremely large forces can be exerted to drive small displacements at high rates, up to the MHz range for a piezoelectric bimorph beam [27]. However, this runs into many of the same limitations of magnets. Commercial piezos are too large for this design and hard to interface with a microscale structure. While cleanroom processes exist for depositing lead zirconate titanate (PZT) and other piezoelectric films, the processes have low yield and are not compatible with many other cleanroom processes. Additionally, high temperatures must be avoided. Some commercial piezos can withstand temperatures as high as 820°C, though most are limited to <400°C [29]. Neither temperature is high enough for a quality fusion bond.

3.1.2 Electrostatic Actuation

Electrostatic actuation is a common method of actuation in MEMS [30]. The operating principle is simple – charge up two plates near each other and electrical attraction will exert a force on both objects. This has been used in devices as varied as Texas Instrument's Digital Micromirror Device (DMD) [1] to MEMS microphones [31], and is regularly used to actuate resonators. The force can be greatly increased by combining multiple interleaved charged fingers to create a comb drive [27].

Electrostatics can exert large forces over short distances with very fast switching time, which make it a great option for a fast, high frequency (thus stiff) resonator. Additionally, fabrication is relatively simple compared to the other actuation methods – a single doping step can give both plates the necessary conductance.

However, an unexpected source of impedance in the actuation circuit, such as higher contact resistance, can cause an unanticipated decrease in voltage across the actuation gap if connected in series. Additionally, if sensing electrically as well, parasitic signals can interfere with the measured signal. Parasitic paths in series with the actuation circuit, caused by poor isolation between the terminals, allow the actuation voltage to interfere with the measured output signal.

Additionally, the electrostatic force F_e is nonlinear, which leads to some interesting effects. For parallel plates, the force F_e and electrical potential energy U_e, respectively, are

$$F_e = \frac{\epsilon_0 A V^2}{2g^2} \text{ and} \tag{3.1}$$

$$U_e = \frac{\epsilon_0 A V^2}{g} \tag{3.2}$$

where $\epsilon_0$is the permittivity of free space, A is the area of actuation, V is the actuation voltage, and g is the current gap between plates. While the system is in equilibrium, the spring force $F_s = k(g_0 - g)$ balances F_e as follows

$$\sum F = 0 = \frac{\epsilon_0 A V^2}{2g^2} - k(g_0 - g)\,. \tag{3.3}$$

Taking the derivative with respect to g yields the spring constant for the system (how much additional actuation force is needed to cause a small change in the gap)

$$k_{system} = -\frac{3\epsilon_0 A V^2}{2g^3} + k\,. \tag{3.4}$$

As expected, with no actuation voltage the spring constant reduces to the stiffness of the beam. However, increasing the voltage actually decreases the apparent stiffness of the system, a phenomenon known as spring softening.

If we solve for the voltage from the sum of the forces above and substitute, we can see that k_{system} becomes negative when actuated beyond $g_0/3$. This point is unstable, any additional voltage will cause the beam to snap in. This instability is known as pull-in. This greatly limits the operating range for an electrostatic device. Since the stiffness decreases faster the closer the deflection is to the critical value, it is wise to only operate at small deflections. Both spring softening and pull-in can be seen below in Figure 3-1 for a silicon beam with dimensions of 1100μm x 220μm x 15μm.

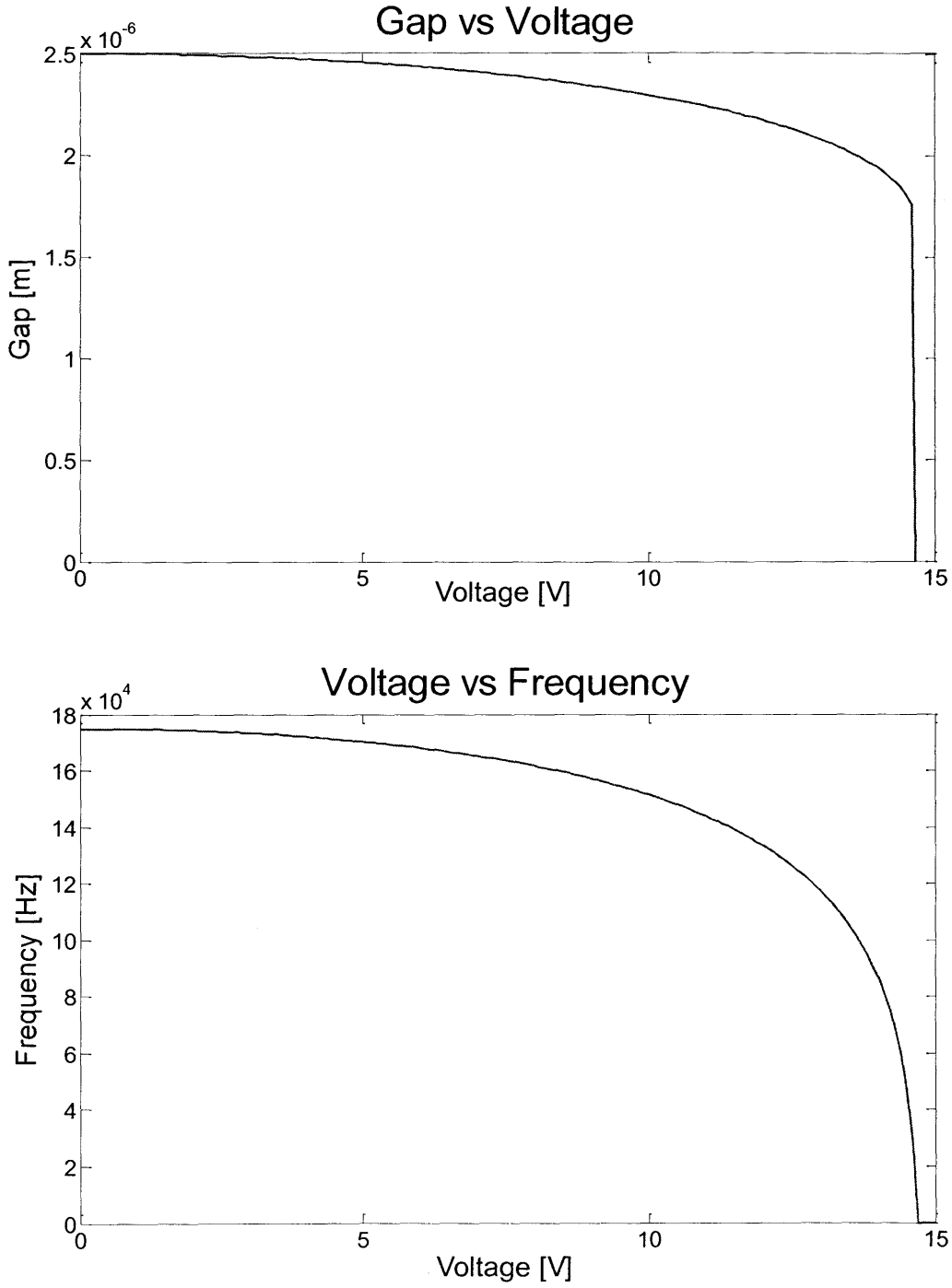

Figure 3-1 - (top) The nonlinear nature of electrostatic actuation can be seen in the first plot. Pull-in occurs at 14.65V, and can be seen in the first plot as the point where the gap goes to 0. (bottom) Spring softening caused by the decrease in the overall spring coefficient. Results are shown for an 1100μm x 220μm x 15μm silicon beam with a 2.5μm gap.

While electrostatic actuation can have lower actuation voltages or parasitic interference if the full circuit is not modeled correctly, and exhibits considerable nonlinear behavior, both of these problems can be avoided with careful design. Careful isolation and integrating the sensing into the actuation (see Third Harmonic Sensing below) can negate many of the harmful parasitic effects. By operating with small deflections, the full nonlinear behavior can be approximated as linear (with a Taylor expansion) around the neutral point with an electrostatically softened spring constant.

A summary of these actuation methods is shown below in Table 3-1.

Table 3-1: Comparison of Actuation Methods

Actuation	Pros	Cons
Electrostatic	-Easiest fabrication -Fast switching -Internal actuation (with external voltage source)	-Parasitic effects on other circuits -pull-in instability -nonlinear response
Thermal	-Internal actuation (with external voltage source)	-Slow -Many materials temperature sensitive -Bilayer beams more complex to fab
Optical heating	-If sensing optically, no need for interconnects	-Same as thermal, plus: -External actuation source (laser)
Piezoelectric	-Internal actuation (with external voltage source) -Fast -Large Forces -Controlled displacements	-Difficult to integrate
Magnetic	-Strong forces	-If external: difficult to integrate and large external actuator -If internal: difficult to fabricate -Slow switching

After considering all the actuation options, electrostatic actuation was chosen for the pressure sensor. All of the other options are either limited in operation or increase the

difficulty of device fabrication. Additionally, several of them require external actuators or equipment to operate, which is not compatible with a modular pressure sensor. While electrostatic actuation isn't perfect either, the limitations can be worked around with a careful design and by limiting deflection to a small range, and actuation can be achieved solely with an externally applied voltage.

3.1.3 Beam Bending

3.1.3.1 Forced oscillations with damping

Before analyzing the full Euler-Bernoulli equation for dynamic beam bending, it is instructive to examine resonance for the case of forced oscillations of a linear spring (spring constant k) with damping (damping coefficient c). A general differential equation describing the motion is

$$\ddot{x} + 2\gamma\dot{x} + \omega_0^2 x = A_0 \sin(\Omega t) \tag{3.5}$$

where $\gamma = c/2m$ is the damping factor, $\omega_0 = \sqrt{k/m}$ is the resonance frequency, $A_0 = F_0/m$ is the magnitude of the acceleration for a force of F_0 and Ω is the forcing frequency. The solution to this equation is given by:

$$x(t) = x_s(t) + X_0 \sin(\Omega t + \theta) \tag{3.6}$$

where $x_s(t)$ is the specific solution (transient), and X_0 is the magnitude of the forced vibration. We want to consider the motions for $t \gg 1/\gamma$ after which the transient vibrations have died out. Substituting $x(t)$ back into the differential equation, at large enough time we can say that the magnitude and phase can be written as

$$X_0 = \frac{A_0}{\sqrt{(\omega_0^2 - \Omega^2)^2 + 4\gamma^2\Omega^2}} \text{ and} \tag{3.7}$$

$$\tan(\theta) = \frac{2\gamma\Omega}{\Omega^2 - \omega_0^2}. \tag{3.8}$$

These are plotted in Figure 3-2 (magnitude X_0) and Figure 3-3 (phase θ).

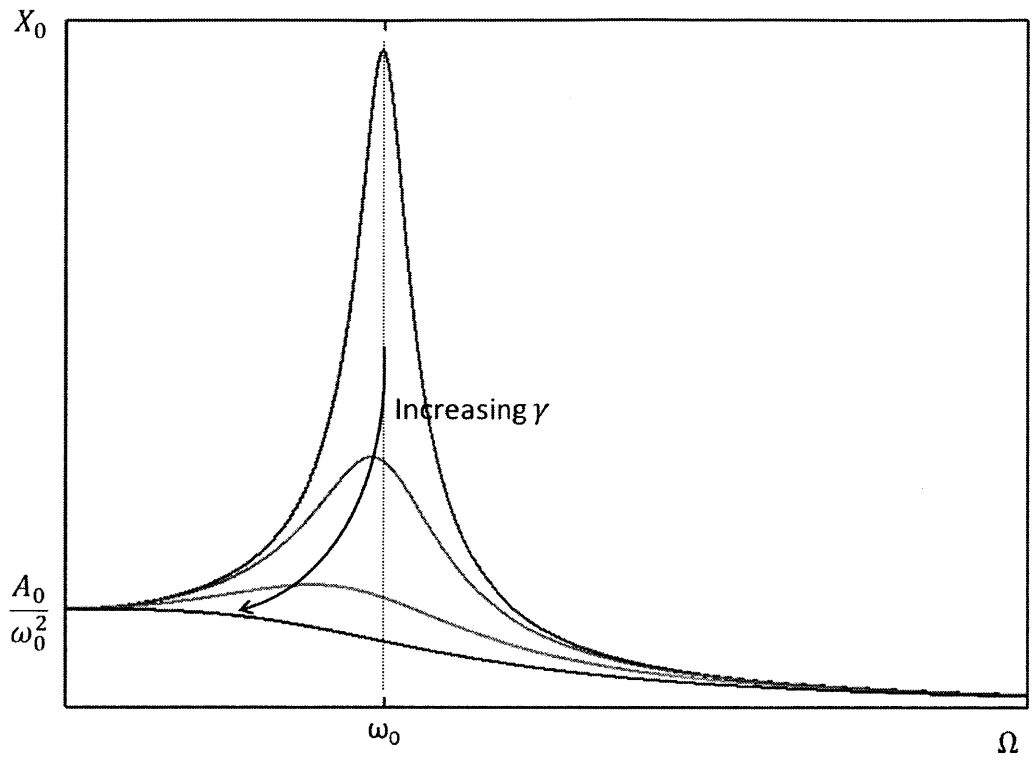

Figure 3-2 - Magnitude of resonance for several different levels of damping.

Typical measurement of the resonance peak assumes that peak width is the frequency range between which $X_0 \geq \frac{X_{max}}{\sqrt{2}}$. This width, for small γ, is

$$\Delta\Omega = \frac{\omega_0}{Q}. \tag{3.9}$$

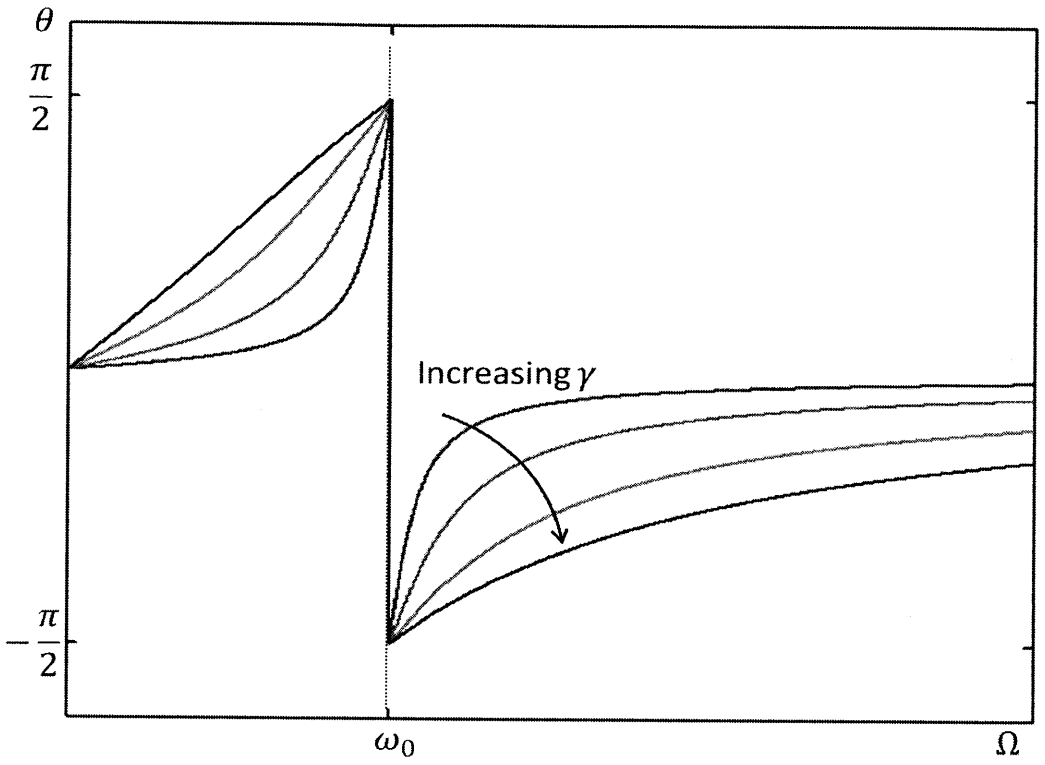

Figure 3-3 - Phase response for several levels of damping

The maximum displacement for a given damping factor can be found by setting the derivative of X_0 to 0.

$$X_{max} = \frac{A_0}{2\gamma\sqrt{\omega_0^2 - \gamma^2}} = \frac{2A_0Q^2}{\omega_0^2\sqrt{4Q^2 - 1}} \tag{3.10}$$

The forcing frequency that corresponds to the maximum value is

$$\Omega_{max} = \omega_0\sqrt{1 - \frac{1}{2Q^2}}. \tag{3.11}$$

For high quality factors, this reduces to

$$X_{max} = \frac{A_0Q}{\omega_0^2} = \frac{(F_0/m)}{(k/m)}Q = \frac{F_0}{k}Q \text{ and} \tag{3.12}$$

$$\Omega_{max} = \omega_0\,. \tag{3.13}$$

While the mechanics of a damped moving beam actuated by a distributed load are certainly more intricate than those of a simple forced spring-mass-damper system, it will be assumed

that they are close enough to approximate the maximum deflection the same way: find the static deflection and multiply by the quality factor.

It may also be possible to monitor resonance by measuring the phase.

3.1.3.2 *Displacement of a Vibrating Beam: Euler Bernoulli Equation*

The actuation of the actual beam will occur along a small section at the end of the beam. This is neither a point load nor a fully distributed load, but the deflection is somewhere in between. These two cases will be analyzed using the Euler-Bernoulli beam bending equation to find bounds on the deflection. First, we consider a distributed load as follows

$$\rho wt\frac{\partial^2 u(x,t)}{\partial t^2}+c\frac{\partial u(x,t)}{\partial t}+EI\frac{\partial^4 u(x,t)}{\partial x^4}=F_e' \tag{3.14}$$

where ρ is the density of the beam, w is the beam width, t is the beam thickness, $u(x,t)$ is the beam displacement, c is the overall damping coefficient, E is Young's modulus, I is the second moment of inertia, and F_e' is a distributed force/length along the beam. The electrostatic force per unit length can be approximated with a Taylor expansion in x around g_0 (where $u(x,t)=0$) as follows

$$F_e'=\frac{\epsilon_0 wV(t)^2}{2\big(g_0-u(x,t)\big)^2}\approx\frac{\epsilon_0 wV(t)^2}{2g_0^2}+\frac{\epsilon_0 wV(t)^2}{g_0^3}u(x,t)\,. \tag{3.15}$$

If we assume the motion of the beam can described by a generalized separable displacement of the form

$$u(x,t)=\sum_{n=1}^{\infty}\phi_n(x)\eta_n(t) \tag{3.16}$$

where $\phi_n(x)$ and $\eta_n(t)$ are the spatial and time dependence of the nth mode of vibration, then the differential equation can be written as

$$\rho wt\phi_n(x)\frac{\partial^2\eta(t)}{\partial t^2}+c\phi_n(x)\frac{\partial\eta(t)}{\partial t}+EI\eta(t)\frac{\partial^4\phi_n(x)}{\partial x^4}-\frac{\epsilon_0 wV(t)^2}{g_0^3}\phi_n(x)\eta_n(t)=\frac{\epsilon_0 wV(t)^2}{2g_0^2}. \tag{3.17}$$

In general, $\phi_n(x)$ can be chosen to be orthogonal, i.e.

$$\int_0^L\phi_m(x)\phi_n(x)dx=\alpha_m\,\delta_{mn} \tag{3.18}$$

where α_m is a normalization constant for the mth mode and δ_{mn} is the Kronecker delta. Since we are actuating at the tip (and damping is relatively low), the motion will be dominated by the first mode, given below

$$\phi_1(x) = \cosh\left(\frac{\kappa_1 x}{L}\right) - \cos\left(\frac{\kappa_1 x}{L}\right) - \left(\frac{\cosh(\kappa_1)+\cos(\kappa_1)}{\sinh(\kappa_1)+\sin(\kappa_1)}\right)\left(\sinh\left(\frac{\kappa_1 x}{L}\right) - \sin\left(\frac{\kappa_1 x}{L}\right)\right) \quad (3.19)$$

where κ_1 = 1.875 is the eigenvalue for the first spatial mode of vibration for a fixed free beam. The differential equation can be simplified by lumping the spatial variations into constants (though the voltage varies with time). This can be done by multiplying the equation by $\phi_n(x)$ and integrating over the span of the beam, and noting that $\frac{\partial^4 \phi_n(x)}{\partial x^4} = \kappa_n \phi_n(x)$

$$m_n \ddot{\eta}_n + c_n \dot{\eta}_n + k_n \eta = q_n \quad (3.20)$$

where modal mass (m_n), damping (c_n), stiffness (k_n), and force (q_n) are given below as:

$$m_n = \rho w t \alpha_n\,, \quad (3.21a)$$

$$c_n = c\alpha_n\,, \quad (3.21b)$$

$$k_n = EI\kappa_n^4 \alpha_n - \frac{\epsilon_0 w V(t)^2}{g_0^3}\alpha_n\,, \text{and} \quad (3.21c)$$

$$q_n = \frac{\epsilon_0 w V(t)^2}{2g_0^2}\int_0^L \phi_n(x)dx\,. \quad (3.21d)$$

For a point load, a similar procedure is used. The electric force over the entire actuation area is assumed to be concentrated at the tip at $x = L$, and can be written as

$$F_e = \frac{\epsilon_0 w l V(t)^2 \delta(x-L)}{2\left(g_0 - u(x,t)\right)^2} \approx \frac{\epsilon_0 w l V(t)^2 \delta(x-L)}{2g_0^2} + \frac{\epsilon_0 w l V(t)^2 \delta(x-L)}{g_0^3}u(x,t) \quad (3.22)$$

where l is the actuation length and $\delta(x-L)$ is the Dirac delta function (centered at L). This form of the electrostatic force leaves the mass and damping constants the same, but stiffness and force must be rewritten as

$$k_n = EI\kappa_n^4 \alpha_n - \frac{\epsilon_0 w l V(t)^2}{g_0^3}\phi_n(L)^2 \text{ and} \quad (3.23)$$

$$q_n = \frac{\epsilon_0 w l V(t)^2}{2g_0^2}\phi_n(L)\,. \quad (3.24)$$

The second term in the stiffness in both cases is the spring softening term, and it remains small for low voltages and small deflections. Assuming that k_n is constant reduces this to a basic

linear ODE with a time varying forcing term. If we apply a sinusoidal actuation voltage, approximated as

$$V(t) = V_{AC}\sin(\Omega t)\,. \tag{3.25}$$

where Ω is the actuation frequency. The forcing term and displacement for a distributed load

$$q_n = \frac{\epsilon_0 w}{2g_0^2}\phi_n(x)\frac{V_{AC}^2}{2}(1-\sin(2\Omega t)) \text{ and} \tag{3.26}$$

$$u(x,t) = U_{max}\sin(\Omega t+\theta)\phi_n(x) \tag{3.27}$$

where U_{max} is the maximum beam displacement. Similar to the simpler forced oscillation case we have

$$U_{max} = \frac{A_0}{\sqrt{(\omega_0^2-\Omega^2)^2+4\gamma^2\Omega^2}}, \tag{3.28}$$

$$\tan(\theta) = \frac{2\gamma\Omega}{\Omega^2-\omega_0^2}, \tag{3.29}$$

$$A_0 = \frac{|q_n|}{m_n} = \frac{\epsilon_0}{4g_0^2}\frac{V_{AC}^2}{\rho t\alpha_n}\phi_n(x)\,, \tag{3.30}$$

$$\omega_0 = \sqrt{\frac{k_n}{m_n}} = \sqrt{\frac{EI\kappa_n^4 - \frac{\epsilon_0 w V_{AC}^2}{g_0^3}}{\rho wt}}\,, \text{and} \tag{3.31}$$

$$\gamma = \frac{c_n}{2m_n} = \frac{c}{2\rho wt}. \tag{3.32}$$

For a point load it is the same except for the q_n, A_0, and ω_0 terms which are given by

$$q_n = \frac{\epsilon_0 lw}{2g_0^2}\phi_n(L)\frac{V_{AC}^2}{2}(1-\sin(2\Omega t))\,, \tag{3.33}$$

$$A_0 = \frac{|q_n|}{m_n} = \frac{\epsilon_0 l}{4g_0^2}\frac{V_{AC}^2}{\rho t\alpha_n}\phi_n(L)\,, \text{and} \tag{3.34}$$

$$\omega_0 = \sqrt{\frac{k_n}{m_n}} = \sqrt{\frac{EI\kappa_n^4 - \frac{\epsilon_0 w V_{AC}^2}{g_0^3}\frac{\alpha_n}{\phi_n(L)^2}}{\rho wt}}. \tag{3.35}$$

As before, the maximum displacement U_{max} at high Q is

$$U_{max} = \frac{A_0 Q}{\omega_0^2} = Q\frac{q_n}{k_n}\phi_n(x)\,. \tag{3.36}$$

For comparison, the displacement $u(x)$ for the realistic static bending case (distributed load over the actuation region, the derivation is in Appendix A) is given by:

$$u(x) = \begin{cases} -\dfrac{F_e' x^2 l}{12EI}(6L - 3l - 2x), & x < L - l \\ -\dfrac{F_e'}{24EI}(x^4 - 4x^3 L + 6x^2 L^2 + 4x(L-l)^3 - (L-l)^4), & x \geq L - l \end{cases} \tag{3.37}$$

$$U_{max} = \frac{-F_e' l}{24EI}(8L^3 - 6L^2 l + l^3) \tag{3.38}$$

The shape of the first harmonic is very similar to that of the stationary, simple beam bending case, as shown below in Figure 3-4. It can readily be seen that the dynamic solutions have a higher maximum deflection due to spring softening. This difference between static and dynamic deflections becomes greater as the voltage (and maximum deflection) increase.

Another trend is that for the same magnitude of total force ($F_{total} = \Sigma F_i$), the more concentrated the load is towards the tip, the higher the deflection because the overall moment is higher. This means that the point load and fully distributed load form conservative upper and lower bounds for the actual dynamic solution.

In order to simplify further analysis, the static point load beam deflections (with a factor of safety) will be used as an approximate value for optimization. This is a reasonable approximation because the point load solutions overestimate the realistic loading situation, while static loading underestimates the deflection. For the case of a 1100 μm x 220 μm x 15 μm beam actuated by a voltage of 14V, the Euler-Bernoulli max deflection is 0.415 μm for a point load and 0.130 μm for a distributed load. For static deflections, a distributed load causes 0.120 μm deflection, a point load leads to a 0.321 μm deflection, and the combined loading case has a deflection of 0.273 μm.

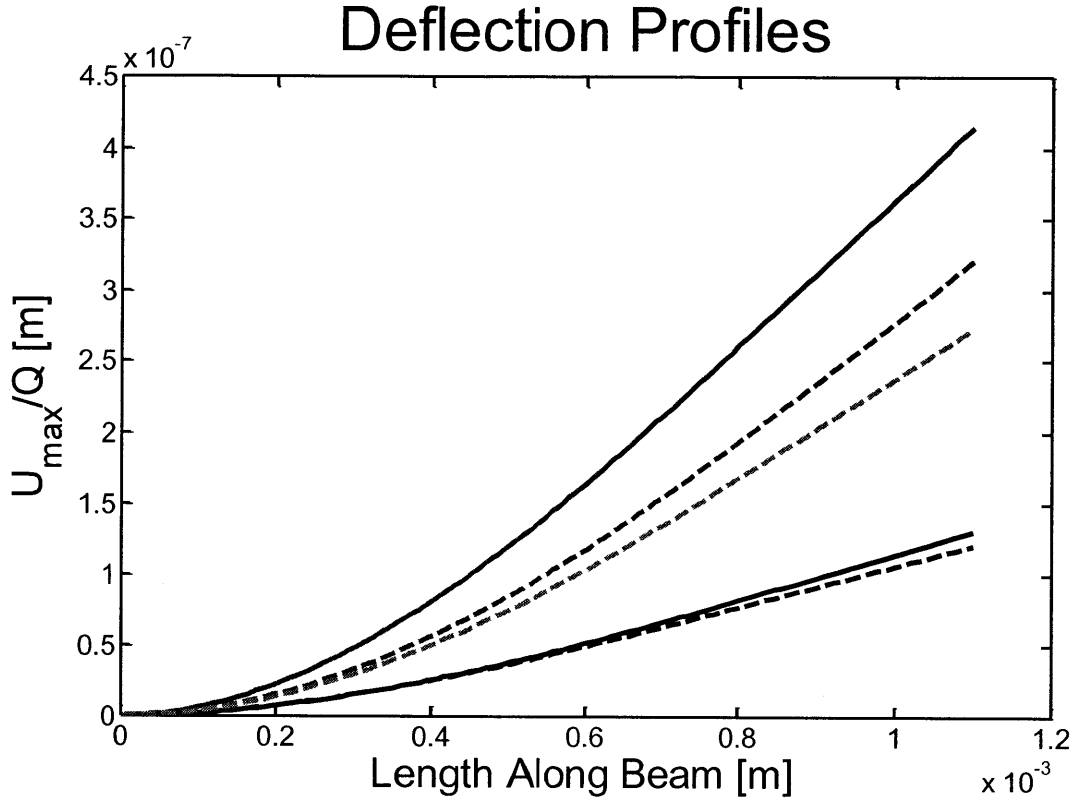

Figure 3-4 - Deflection of cantilever beams under various loading conditions for a 1100 μm x 220 μm x 15 μm beam actuated by a voltage of 14V. Solid lines are solutions to the Euler-Bernoulli equation; dashed lines are static solutions using basic beam theory with a constant force (no gap dependence). Blue indicates a point load at the end, red is the realistic situation with a distributed load over the actuation region, and black is a fully distributed load. The total force applied is the same across all loading conditions, so the distributed load for the black curves was l/L times the actual distribution.

3.1.4 Further analysis of the capacitive design

Now that an actuation method has been chosen, some further analysis is in order to make sure that everything will work out as planned.

3.1.4.1 Torsion from Misalignment

The electrostatic actuation design requires alignment of electrodes in two separate wafers. With perfect alignment, the moment due to the distributed actuation load balances across the beam and sums to zero. However, slight misalignment creates a net moment at the actuation end of the cantilever as shown in Figure 3-5 below.

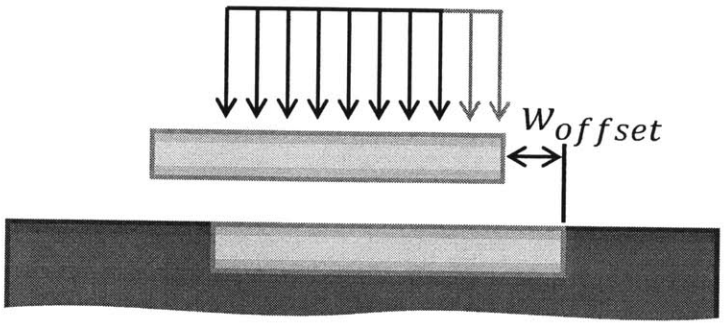

Figure 3-5: Unbalanced actuation forces caused by misalignment are shown in red. Doped regions are shown in orange, undoped silicon in gray.

This misalignment creates a torque at the end of the beam. For torsion in thin rectangular beams, the angle of twist per unit length, α, is often approximated by:

$$\alpha = \frac{3T}{16Gt^2w} \tag{3.39}$$

where T is the net torque on the ends of the beam and G is the shear modulus. The rotation due to various actuation voltages and offsets is shown in Figure 3-6 below. Electrostatic force (and the resulting torque) was calculated due to the amount of overlap between cantilever tip and the other actuation plate. While there is some force exerted beyond the edges, this is insignificant compared to the attraction from the main overlapping region, and the edge effect will be neglected for this approximation.

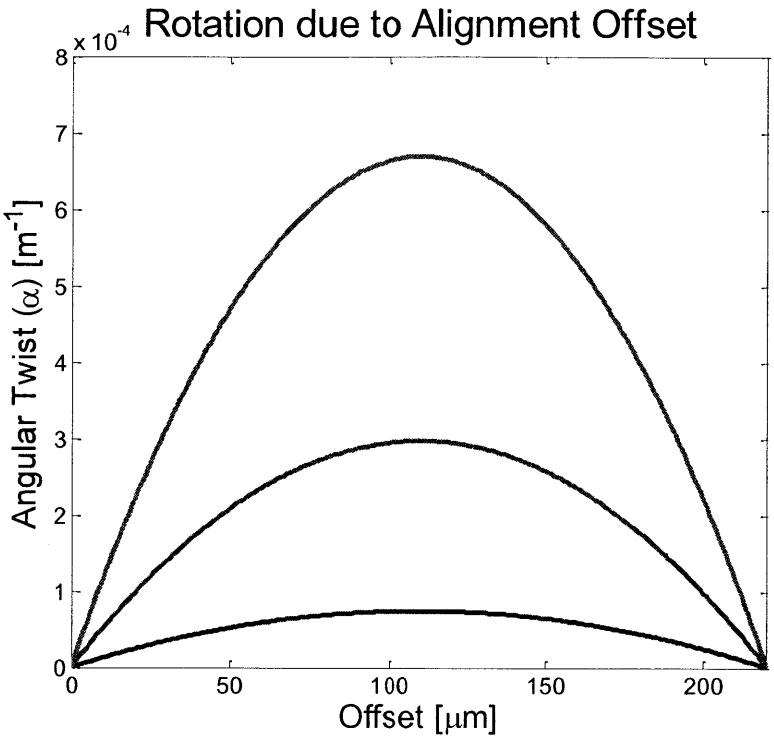

Figure 3-6 - Angular twist for 5V (blue), 10V (green) and 15 V (red) with a 15μm thick , 220μm wide beam.

Since α is per unit length, the actual angle at the actuation end is on the order of 10^{-7} radians even for large voltages and offsets. This leads to a difference in displacement between the two sides of the beam of order 10^{-11}m, which is well below the displacement of the beams and can thus be neglected. Thinner beams (required for lower frequency designs) would have more torsion. However, for a beam of order 1mm long and 200μm wide to bend more than 5nm (still small, but approximately 1% of the intended deflection), it would need to be under 1μm thick.

3.1.4.2 ***Resistance of Beam to Fracture***

Since the beams have a high resonance frequency, it is unlikely that any outside vibrations will cause significant oscillations. However, it is still worth considering how sensitive the cantilevers are to outside shocks.

One extreme situation would be placing that shows the durability of the cantilevers is to consider the forces on the beam if it were placed in the spin drier. The wafer experiences rotational velocities on the order of 2000-3000 rpm. The maximum centripetal forces would be on the outer dies, where the distance from the center is at a maximum of 7.5cm. An upper bound for the stresses experienced by the beam would consider the full centripetal force due to be applied as a point load at the tip of the cantilever. This load allows for the stresses to be calculated using beam theory. For a 1100μm x220μm x15μm beam, rotating at 3000rpm, the

bending stresses are of 4.12 MPa on the top and bottom of the beam if the force is parallel to the thin axis, and 281kPa along the wide axis. While there is a stress concentration at the base of the beam along the wide axis, it would need to magnify the force 72 times to reach the fracture strength of silicon around 300MPa.

3.2 Analysis of Sensing Methods

There are many possible methods for sensing a moving cantilever beam, each coming with its own set of benefits and limitations as will be discussed below.

3.2.1 Optical

Optical sensing involves focusing a laser on the tip of the cantilever through a transparent top wafer (likely pyrex), and measuring changes in the reflected light using a photodiode. An obvious benefit to this sensing method is that it places very few restrictions on the fabrication process. There are no piezoelectric films or integrated magnets, just a transparent top wafer. Additionally, this technique could be used with any actuation method because the laser should have minimal interaction with the internal workings of the device. The exception would be thermal actuation, where the heating caused by the laser is desired and causes the beam deflection.

The tradeoff for less complicated fabrication is that the sensing requires an external measurement device (a laser) to operate. This does not meet the objective of having a self-contained pressure sensor.

3.2.2 Piezoresistive

This design incorporates the piezoresistive properties of Si, or the relationship between stress and resistivity in the material. A winding conductor is patterned on the cantilever beam. Actuation causes stresses in the beam, and this can be seen as small changes in resistance across the conductor.

3.2.2.1 Background

Many macroscale strain sensors usually use piezoresistivity to measure strain. The sensors consist of a soft pad with an embedded metal resistor. The resistor typically winds back and forth to increase its active length. The pad is firmly attached to the measured surface, and as the object deforms, so does the resistor.

The change in resistance comes from both geometry (the length changes and the cross-section of the material changes due to the Poisson effect) and the piezoresistive change, as shown below:

$$\frac{\Delta R}{R} = (1 + 2\nu + \pi E)\epsilon \tag{3.40}$$

where ν is the poisson ratio, π is the piezoresistive coefficient in the strain direction, and E is the Young's modulus. For most metals, π is negligible so the relative change in resistance is at most 2ϵ.

Silicon, however, is a much better piezoresistive material. Stress deforms the band structure of Si, causing a much higher value for π. For this reason, the sensitivity for silicon strain gauges can be 50-100 times greater than similar metal gauges. Silicon has the added benefit that it is almost perfectly elastic, so the sensor does not deform over time.

However, electronic behavior in silicon is not isotropic (like the Poisson effect is in metals) and must be modeled with tensors. The electric field in a material is related to current density through the resistivity tensor:

$$E_i = \rho_{ij} J_j \,. \tag{3.41}$$

However, resistivity itself is related to stress through the piezoresistivity tensor:

$$\rho_{ij} = \rho_{ij}^0 + \pi_{ijkl}\sigma_{kl} \tag{3.42}$$

where ρ_{ij}^0 is the unstressed resistivity and π_{ijkl} is the resistivity tensor. Silicon has diamond symmetry, so there are only three independent piezoresistive coefficients. Written in 6 by 6 matrix shorthand, these are π_{11}, π_{12}, π_{44} shown below

$$\Delta\rho = \begin{bmatrix} \pi_{11} & \pi_{12} & \pi_{12} & 0 & 0 & 0 \\ \pi_{12} & \pi_{11} & \pi_{12} & 0 & 0 & 0 \\ \pi_{12} & \pi_{12} & \pi_{11} & 0 & 0 & 0 \\ 0 & 0 & 0 & \pi_{44} & 0 & 0 \\ 0 & 0 & 0 & 0 & \pi_{44} & 0 \\ 0 & 0 & 0 & 0 & 0 & \pi_{44} \end{bmatrix} \begin{bmatrix} \sigma_{11} \\ \sigma_{22} \\ \sigma_{33} \\ \sigma_{23} \\ \sigma_{13} \\ \sigma_{12} \end{bmatrix} \tag{3.43}$$

The constants have the following values in silicon oriented along the <100> direction

Constant	p-type Si [10^{-11} Pa^{-1}]	n-type Si [10^{-11} Pa^{-1}]
π_{11}	6.6	-102.2
π_{12}	-1.1	53.4
π_{44}	138.1	-13.6

It can easily be seen that in this orientation, p-type silicon is largely unaffected by tensile stresses (such as those caused in bending). However, rotating from a piezoresistor aligned along a <100> direction to a <110> direction yields drastically different results. The tensor rotation yields only two significant coefficients: the longitudinal piezoresistive coefficient

$\pi_L = 71.8 \text{ x } 10^{-11} \approx \frac{\pi_{44}}{2}$ and the transverse coefficient $\pi_T = -66.3 \text{ x } 10^{-11} \approx -\frac{\pi_{44}}{2}$, with all shear contributions being negligible.

This simplifies the analysis and allows us to concentrate solely on the bending stresses rather than any shear effects. The change in resistance of a p-type piezoresistor in this orientation would be

$$\frac{\Delta R}{R} = \pi_l \sigma_l + \pi_t \sigma_t \,. \tag{3.44}$$

3.2.2.2 ***Optimization of beam stress***

A few assumptions:

- While the beam would be moving, and solutions to the Euler-Bernoulli equation give more accurate deflections, we will use basic beam theory for simplicity.
- The deflection due to resonance can be approximated as the Q times the static beam deflection
- Since the normal stresses along the beam will be orders of magnitude greater than any other stress, we will only consider only them here.
- We will assume that the piezoresistors are close enough together that they all experience the same normal stress.
- Assume electrostatic actuation

The normal stress along the length of a bending beam is

$$\sigma = \frac{My}{I}, \tag{3.45}$$

where M is the moment, y is the perpendicular distance from the neutral axis, and I is the second moment of inertia of a cross section of the beam. For a rectangular cross-section, $I = wt^3/12$. From elementary beam bending, we know that

$$M(x) = -EI\frac{d^2u}{dx^2}, \tag{3.46}$$

where E is Young's modulus and u is the vertical deflection of the beam. The electrostatic force F_e at the end is an applied distributed load

$$F_e' = \frac{\varepsilon_0 V^2 w}{2g^2}, \tag{3.47}$$

where V is the total applied voltage, w is the width of the beam and g is the gap height. In order to ensure beam-like behavior, rather than plate-like behavior, it is necessary that the beam width be small, as given by

$$w \leq \frac{L}{5}, \tag{3.48}$$

where L is the length of the beam. One final constraint: the device must not pull-in. With a factor of safety of 2, this means that

$$2QU_{max} \leq \frac{g}{3} \tag{3.49}$$

Several design principles can be determined from the structure of the equations and constraints for any form of beam deflection.

First, we can determine the critical dimensions affecting the stress at the base of the beam where the piezoresistors are located. The total force applied by electrostatic actuation is

$$F_{total} = F_e l = \frac{\varepsilon_0 V^2 w l}{2g^2}, \tag{3.50}$$

where l is the length of the actuator and ε_0 is the permittivity of free space. Let us assume that $l = \zeta L$ where ζ is a constant. This greatly simplifies the approximations for beam displacement, and will be relaxed later. The moment arm for a constant distributed force can be placed at the center of the distribution. It follows that the moment due to the electrostatic force is then

$$M = F_{total}\left(L - \frac{l}{2}\right) \propto \frac{V^2 L^2 w}{g^2}. \tag{3.51}$$

For a constant distributed load from base to tip, beam theory always gives a spring constant that is proportional to the L^4; for a point load at the tip, the spring constant is proportional to L^3. For the moment let's consider actuating along the entire beam, so the maximum deflection U_{max} goes as

$$U_{max} \propto \frac{F_e L^4}{I} \propto \left(\frac{V^2 w}{g^2}\right)\left(\frac{L^4}{I}\right). \tag{3.52}$$

Large U_{max} leads to larger stresses and a larger signal. The pull-in instability is the limiting factor here. The instability occurs when the deflection reaches one third of the gap (though in reality it is unwise to actuate anywhere near pull-in). This means that once you

choose a safe deflection range (say, 10% of the gap), you can take the maximum displacement to be proportional to the un-actuated gap:

$$U_{max} \propto g_0 . \tag{3.53}$$

With this, we can combine the above equations to describe the relative magnitude of the beam stress in terms of design parameters as follows

$$I \propto \frac{wL^4V^2}{g^3}. \tag{3.54}$$

For any I this can be substituted into the stress to get

$$\sigma \propto \left(\frac{V^2L^2w}{g^2}\right)\left(\frac{g^3}{wL^4V^2}\right)y = \left(\frac{g}{L^2}\right)y . \tag{3.55}$$

This leads to some important conclusions. First, neither the applied voltage nor the width play a role in the stress. This makes sense - increasing voltage merely increases the deflection, but that is already limited by the gap. Also, any additional electrostatic force due to extra width is balanced by extra stiffness from the cantilever spring.

Secondly, short, thick devices with large gaps are favored. Again, this makes sense – shorter beams would have a higher radius of curvature for a comparable deflection. Additionally, large gaps allow larger deflections.

Even relaxing the simplification that $l \propto L$ doesn't change the push towards small L. In the limit that $l \rightarrow L$, the loading is fully distributed and

$$U_{max} \propto L^4 , \tag{3.56}$$

and the math follows similar to above, with stress proportional to L^{-2}. In the limit where $l \rightarrow 0$, the loading resembles a point load (although when $l = 0$, there is no loading at all), and

$$U_{max} \propto L^3 \tag{3.57}$$

This leads to a stress of

$$\sigma \propto \frac{g}{L}y . \tag{3.58}$$

The more realistic situation where a distributed load is applied to a portion of the beam would lead to a combination of the two (a polynomial with 3rd and 4th order terms for displacement). Either way, smaller cantilevers yield higher stresses.

3.2.2.3 ***Analysis of Piezoresistive Design***

The piezoresistor would consist of a long winding doped region at the base of the cantilever, similar to macroscale strain gauges, as shown in Figure 3-7 below.

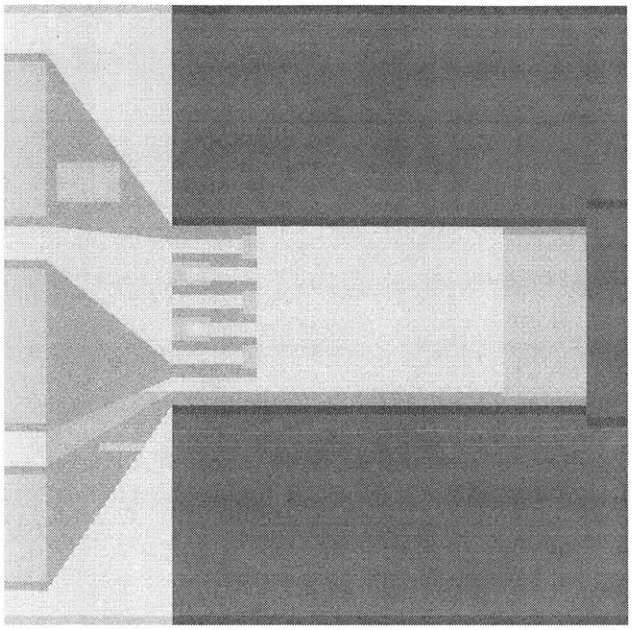

Figure 3-7

Two dimensional squares of resistance can be used to calculate the overall resistance of the winding pattern. The length and width cancel, leaving the resistance for a square of any side length as

$$R_{square} = \frac{\rho}{t} \tag{3.59}$$

A few other considerations must be taken into account:

1. The winding of the resistor cannot be spaced to closely or the limits in lithography coupled with spreading due to diffusion in subsequent heating steps will cause shorting of the resistor.

2. In the bends, the current is running transverse to the main tensile stress. Since π_T is negative and approximately the same magnitude as the longitudinal coefficient, each bend cancels out one square of resistance.

3. Extra space must be left for the actuation electrode. This will prevent any stray signals from crossing over to the piezoresistive sensor. Additionally, if the actuation shorts out, the entire device is dead, while if one bend of the resistor shorts just the sensitivity decreases. The extra space adds an additional factor of safety to prevent that.

To calculate the resistance of the doped resistor, let us divide the beam into units of width where the size of the unit is yet to be determined. Two units will be used for the actuation electrode, and two more to separate it from the resistor. Let each section of the resistor be one unit wide, with one unit of separation. The resistor must start and end at the base of the beam, so an increase in the number of winds must include four units. To put this in perspective, a 200um wide beam could have eight 10.5um wide paths.

The resistivity will vary with the stress in the beam, so the overall resistance will require integrating over the doped region as follows.

$$R' = \int_V \rho dV = \int_{x_1}^{x_2} \int_{y_1}^{y_2} (\rho^0 + \pi\sigma) w dy dx \tag{3.60}$$

where R' is the new resistance. This gives a resistance for one path of

$$R'_{path} = R + w_{path}\pi_L \frac{F_{total}\left(L - \frac{l}{2}\right)(x_2^2 - x_1^2)(y_2^2 - y_1^2)}{I}. \tag{3.61}$$

This shows several important features for this sensor. First, the regions closest to the base of the beam have the highest stress and sensitivity. Similarly, the surface of the beam has the highest stresses and sensitivity. In fact, if the doped region passes over the neutral axis ($y = 0$), the resistance change actually decreases. In the extreme case where doping extends across the entire beam, the resistance stays constant because the top is in tension while the bottom compresses.

3.2.2.4 ***Difficulties***

One of the primary difficulties with the piezoresistive design is achieving sufficient isolation between the separate paths in the cantilever. While the resistivity difference is quite high between doped silicon in the piezoresistor ($\rho_{doped} \sim 0.0858\Omega - cm$) and undoped silicon ($\rho_{undoped} \sim 44.44\Omega - cm$), the path for the doped silicon is long and narrow, while the undoped silicon is short wide. If, as in Figure 2-1, the doped regions and the separation regions are the same width, then the width for one is the length for the other, and vice versa. The resistance for each lead, R_{lead}, and isolation between neighboring leads, $R_{isolation}$, are given by

$$R_{lead} = \rho_{doped}\frac{L}{tw} \text{ and} \tag{3.62}$$

$$R_{isolation} = \rho_{undoped}\frac{w}{tL} \tag{3.63}$$

Therefore the ratio of resistance goes as

$$\frac{R_{isolation}}{R_{lead}} = \frac{\rho_{undoped}}{\rho_{doped}}\left(\frac{w}{L}\right)^2 . \tag{3.64}$$

The ratio of the resistivities above is 500:1. If we ask that the isolation between one wind and the next be more than 10:1 (which is still pretty low), the aspect ratio of the doped region must be less than 7:1. For a more desirable 100:1 isolation, the ratio would have to be less than 2.5:1.

This isolation analysis simplifies the situation, because the voltage difference across the two resistors is not the same – since there is a voltage drops along the doped lead, there is a linear relationship in the voltage drop along the isolation region.

A few approaches can be used to alleviate some, but not all of the isolation concerns. A more resistive wafer can be used. Wafers with resistivities as high as 1000 Ω-cm is commercially available. Additionally, while it decreases the overall length of the resistor, the paths can be placed much farther apart. But this simple analysis points out one of the greatest design difficulties for the piezoresistive sensing approach: isolation between the leads greatly limits the number of winds and decreases the sensitivity.

3.2.3 Capacitive

Capacitive sensing is very simple in principle – movement in one of the capacitive plates can be sensed as a change in capacitance of the system. However, by simply measuring the capacitance of the gap, one must be careful that the signal will not be swamped by other parasitic capacitances in the system.

However, by modifying the sensing so that one looks solely at the signal at the third harmonic arising from the cantilever motion, one can eliminate many of these drawbacks as will be discussed below. Additionally, both actuation and sensing can be integrated into a single pair of electrodes.

3.2.3.1 Third Harmonic Sensing

The motion of the cantilever (and thus the plate at the end) acts as a variable capacitor. This allows us to send in a known actuation signal and calculate the motion of the beam from the output on the other side. We start by applying an alternating current at half the resonant frequency of the beam with an amplitude centered at 0V.

$$V(t) = V_{AC}\sin(\Omega t) \tag{3.65}$$

where Ω is the radial frequency or the actuation voltage and V_0 is the amplitude of the voltage. Since the force on the beam involves the voltage squared, the beam vibrates at double the actuation frequency (2Ω). The amplitude of the beam can then be generally written as

$$u(x,t) \propto u(x)\sin(2\Omega t + \theta)\,, \tag{3.66}$$

where θ is the phase shift caused by damping, and $u(x)$ is the mode shape of the actuated beam. By approximating the end of the beam as parallel to the substrate (which is approximately true for small deflections) the capacitance of the charged beam and its time derivative can be written as

$$C(t) = \frac{\varepsilon_0 w l}{g - U_{max}\sin(2\Omega t + \phi)} \text{ and} \tag{3.67}$$

$$\frac{\partial C'}{\partial t} = \frac{2\Omega\varepsilon_0 w l U_{max}\cos(2\Omega t + \phi)}{(g - U_{max}\sin(2\Omega t + \phi))^2} \tag{3.68}$$

where U_{max} is the maximum deflection at the beam tip. Charge stored in a capacitor is given by

$$Q_e(t) = C(t)V(t)\,. \tag{3.69}$$

Current is then

$$\begin{aligned} i(t) &= \frac{\partial Q}{\partial t} \\ &= \frac{\partial C}{\partial t}V(t) + \frac{\partial V}{\partial t}C(t) \\ &= \frac{\varepsilon_0 w l \Omega V_{AC}}{g - U_{max}\sin(2\Omega t + \phi)}\left(\frac{U_{max}(\sin(\Omega t + \phi) - \sin(3\Omega t + \phi))}{g - U_{max}\sin(2\Omega t + \phi)} + \cos(\Omega t)\right) \end{aligned} \tag{3.70}$$

Signal processing, such as using a lock-in amplifier, can be used to separate the third harmonic current $i_3(t)$ at frequency 3ω from the rest of the signal

$$i_3(t) = \frac{\varepsilon_0 w l V_{AC}\Omega(U_{max}\sin(3\Omega t + \phi)}{(g - U_{max}\sin(2\Omega t + \phi))^2} \tag{3.71}$$

When $U_{max} \ll g$ (as designed, $U_{max} \leq g/6$, so this is a rough approximation), the denominator reduces to g^2 and the selected third harmonic output current can be written as

$$i_3(t) = \left(\frac{\varepsilon_0 w l}{g}\right)\left(\frac{V_{AC}\omega(u_{max}\sin(3\omega t + \phi)}{g}\right) = C_0 V_{AC}\omega\frac{u_{max}}{g}\sin(3\omega t + \phi) \tag{3.72}$$

where C_0 is the un-actuated capacitance.

Now consider other capacitances in the system that are not varying at 2Ω . A constant capacitance will not have a time derivative, so it will only appear in the final signal as a constant

multiplier of the voltage time derivative. Even another time varying capacitor with frequency ω_{cap} will factor in at a frequency of $(\Omega + \omega_{cap})$, so unless the unintended capacitance varies at precisely at 2Ω it will not couple into the third harmonic output.

One final benefit to consider is that the third harmonic sensing gives a precise frequency range to measure the signal. By cutting out other frequencies, noise can be greatly reduced. Additionally, since the target third harmonic frequency will be high (~30kHz), it will be above 1/f noise.

*3.2.3.2 **Effect of Changing Beam Dimensions***

Like in the piezoresistive method, the beam will be actuated electrostatically. This places the same constraints on the beam (pull-in, beam-like behavior), and means that the beam will have the same deflection. The desired output signal, the third harmonic current, is given by:

$$i_3(t) = C_0 V_{AC} \Omega \left(\frac{u_{max}}{g}\right) \sin(3\Omega t + \phi) \tag{1.1}$$

where C_0 is the un-actuated capacitor, V_{AC} is the amplitude of the voltage, Ω is the angular frequency of the actuation voltage, g is the gap and θ is the phase shift. The capacitance is given by

$$C_0 = \frac{\varepsilon_0 w l}{g} \tag{1.1}$$

The device is actuated with the voltage oscillating between $+V_0$ and $-V_0$ at Ω, so the beam oscillates at twice that frequency, or 2Ω . We want to operate near the beam's resonant frequency, ω_0, which can be calculated as follows

$$2\Omega = \omega_0 = 2\pi k_1^2 \sqrt{\frac{E}{12\rho}} \left(\frac{t}{L^2}\right). \tag{3.73}$$

As before, the maximum deflection is limited according to the pull-in instability

$$U_{max} \leq \frac{g}{6} \tag{3.74}$$

with the largest currents being obtained for larger displacements. Putting this all together yields

$$i_3 \propto \left(\frac{wl}{g}\right) V \left(\frac{t}{L^2}\right) g = \frac{Vwlt}{L^2}. \tag{1.1}$$

It can easily be seen that larger widths increase output. Substituting for the largest allowable width ($w = L/5$), we obtain the following:

$$i_3 \propto \frac{Vlt}{L}. \tag{3.75}$$

It is also likely that as L increases, so will l. Assuming $l \propto L$ we obtain

$$i_3 \propto Vt\,. \tag{3.76}$$

3.2.3.3 ***Noise***

Noise in the system (excluding noise in the detection apparatus) comes from two main sources:

1) "Damping Noise": Random motion of the cantilever beam due to pressure differences between the air on either side of the beam caused by random Brownian motion. It is related to the damping coefficient (qualitatively, the difficulty for air molecules to redistribute themselves). The magnitude of the displacement is given by

$$u_n = \sqrt{4k_B T c} \tag{3.77}$$

The effect of damping noise can be seen by modifying the derivation for the third harmonic signal. Random motion changes the capacitor gap

$$C'(t) = \frac{\varepsilon_0 wl}{g - u_{max}\sin(2\Omega t + \phi) - u_n}, \tag{3.78}$$

where the prime refers the quantity with noise. This also changes the time derivative of the capacitance

$$\frac{\partial C'}{\partial t} = \frac{2\Omega\varepsilon_0 wl\left(u_{max}\cos(2\Omega t + \phi) + \frac{\partial u_n}{\partial t}\right)}{(g - u_{max}\sin(2\Omega t + \phi) - u_n)^2}, \tag{3.79}$$

Assuming the derivative of noise displacement is negligible, the current becomes

$$i'(t) = \frac{\varepsilon_0 wl\Omega V_0}{g - u_{max}\sin(2\Omega t + \phi) - u_n}\left(\frac{u_{max}\left(\sin(\Omega t + \phi) - \sin(3\Omega t + \phi)\right)}{g - u_{max}\sin(2\Omega t + \phi) - u_n} + \cos(\Omega t)\right), \tag{3.80}$$

Picking out the third harmonic, we obtain

$$i_3'(t) = \frac{\varepsilon_0 w l V_0 \Omega (u_{max} \sin(3\Omega t + \phi)}{(g - u_{max} \sin(2\Omega t + \phi) - u_n)^2}. \tag{3.81}$$

As long as $g \gg u_{max} + u_n$, (a good approximation, considering u_n is on the order of *pico*meters) $i_3(t)$ is still given by

$$i_3(t) = C_0 V_0 \Omega \left(\frac{u_{max}}{g}\right) \sin(3\Omega t + \phi), \tag{3.82}$$

which suggests that damping noise has negligible effect on the output current.

2) Johnson Noise: Due to random motion of electrons in a resistor, an additional noise voltage is applied to the capacitor, given by

$$v_n = \sqrt{\frac{k_b T}{C_0}}. \tag{3.83}$$

Similarly, this changes the applied voltage to the form

$$V'(t) = V_0 \sin(\Omega t) + v_n, \tag{3.84}$$

where the prime refers the quantity with noise. The derivative changes to

$$\frac{\partial V'}{\partial t} = V_0 \, \Omega \cos(\Omega t) + \frac{\partial v_n}{\partial t} \tag{3.85}$$

Assuming that the time derivative of the Johnson noise is negligible, we obtain

$$\begin{aligned} i'(t) &= \frac{\partial C}{\partial t}[V(t) + v_n] + \frac{\partial V}{\partial t} C(t) \\ &= i(t) + v_n \frac{\partial C}{\partial t} \\ &= i(t) + v_n \frac{2\Omega \varepsilon_0 w l u_{max} \cos(2\Omega t + \phi)}{(g - u_{max} \sin(2\Omega t + \phi))^2}. \end{aligned} \tag{3.86}$$

While this changes the output at the second harmonic, if we are careful to pick out the third harmonic (3Ω) we can remove all noise except that which varies at a frequency equal to or a multiple of the third harmonic.

This analysis suggests that major (predictable) noise sources have negligible impact on the output signal. Of course, there will still be noise from the testing equipment.

3.2.3.4 Difficulties

This method doesn't come without its limitations. Firstly, while the operation inside the device is simple, separating the signals outside will take additional hardware. A lock-in amplifier should be able to zero in on the signal.

3.3 Limits on Dimensions

Many aspects of the design can be controlled through fabrication and careful selection of materials:

- The cantilever dimensions (length L, width w, and thickness t)
- Capacitive gap g
- Resonant frequency ω_0 (dependent on beam dimensions)
- Size, number and spacing of squeeze-film holes
- Actuation voltage V_{AC}

However, many of these variables are inter-related or can only be chosen within a specific envelope determined by fabrication limitations and physical laws. Once a feasible range has been determined, the remaining degrees of freedom can be chosen to maximize the pressure sensor's sensitivity. Several limiting factors that apply to any resonant pressure sensor design are described below.

3.3.1 Fabrication limitations

Several ranges of several device parameters (shown in figure 1) are set by inherent limitations of the available fabrication steps.

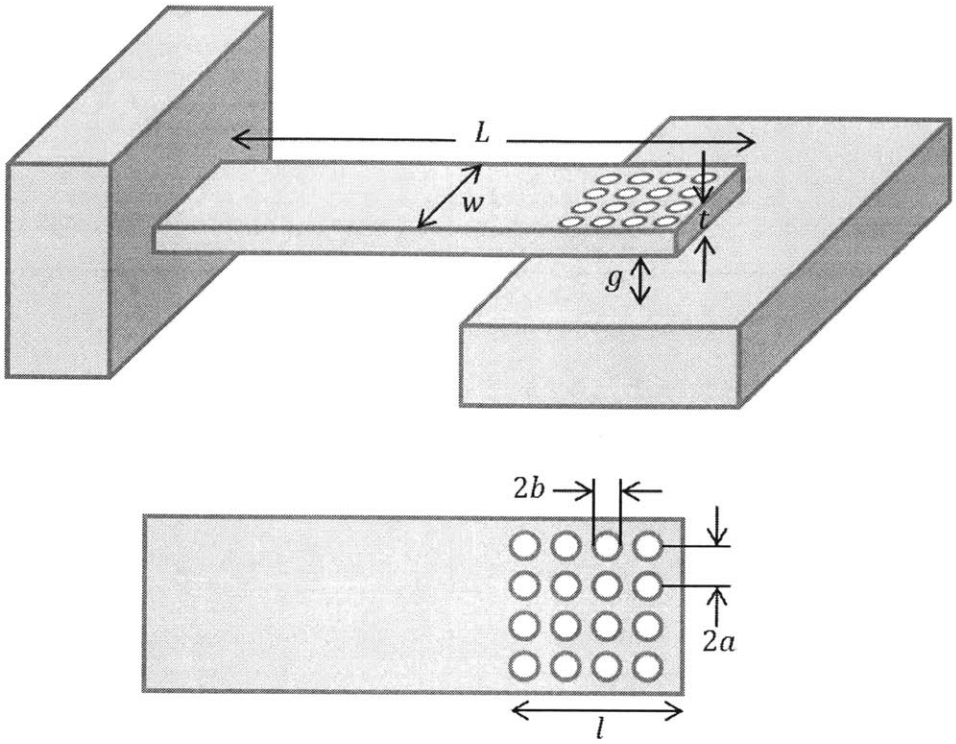

Figure 3-8 Schematic of resonator, showing critical dimensions (Note: not to scale)

1) The gap (g) between the cantilever and substrate (where the device is actuated) is determined by the thickness of a PECVD oxide. While these oxides can in theory by quite thick (approaching 20μm), thicker oxides have considerable compressive stresses and are prone to cracking. As such, the thickness of the oxide (and thus g) will be limited to a maximum of 4 μm.
2) The radius of the holes (b) used to decrease squeeze film damping must be within the "safe" range for photolithography and DRIE etching. Light invariably scatters during photolightography, creating angled sidewalls in the resist. This means that while 1-2μm features *can* sometimes be patterned with contact photolithography, it is unlikely that the mask will withstand DRIE etching. As such, the holes will be restricted to $b \geq 2\mu m$ (or a feature size of $2b \geq 4\mu m$).

3.3.2 Gravitation Effects

Gravity also places a constraint on the dimensions of the beam - a long thin beam will deflect slightly in the direction of gravity. Even a slight increase in deflection could decrease the gap and lead to unexpected pull-in and device failure. As such, the deflection due to gravity is constrained by

$$u_g \ll g_0 \tag{3.87}$$

where g_0 is the actuation gap. Gravity is modeled as a uniform distributed load of the form

$$F_{grav} = \rho w t a_g \tag{3.88}$$

where a_g is the gravitational acceleration. The maximum deflection (at the tip of the cantilever) is given by

$$u_g = \frac{F_{grav} L^4}{8EI} = \left(\frac{3}{2}\right)\left(\frac{\rho a_g}{E}\right)\left(\frac{L^4}{t^2}\right) \tag{3.89}$$

$$L \leq \left(\frac{u_g}{g}\left(\frac{2Et^2}{3\rho a_g}\right)\right)^{\frac{1}{4}} \tag{3.90}$$

With E and ρ for silicon, $a_g = 9.8 m/s^2$, g = 3 μm

$$L \leq 1910\left(\frac{u_g}{g} t^2\right)^{\frac{1}{4}} \quad (L \; in \; [um]) \tag{3.91}$$

Therefore, in order to ensure that gravitational deflection is under 5% of the gap, $L \leq 903.2\sqrt{t}$. To ensure it is less than 1%, the length must be under $\leq 604.0\sqrt{t}$. While it is unlikely that we will hit the gravitational limit, along with the frequency minimum these two constraints bound L.

3.3.3 Frequency of Operation

For a slowly moving beam, the gas has enough time to leak out from between the plates. There is little pressure built up, and the gas is modeled as incompressible. For very fast vibrations, the gas cannot move fast enough and must be modeled as compressible. Expanding and contracting the gas means that an additional air spring due to the increased pressure must be added to the stiffness of the beam. The nondimensional number governing this behavior is the squeeze number σ, given by

$$\sigma = \frac{12\mu\omega L_c^2}{P_a g_0^2}, \tag{3.92}$$

where L_c is the characteristic length preventing gas flow and P_a is the ambient pressure. At a squeeze number of 1, the elastic force of the air starts to become appreciable, and at $\sigma = 10$, the elastic and damping forces are of the same magnitude [32].

For a regular cantilever beam with no holes, L_c is the full width of the beam. For a cantilever beam with dimensions of 1100x220μmx15μm (the size in the final device), at a

resonant frequency of 10^5rad/s, this translates to $\sigma = 1.67$. This means that the elastic compression of the gas is starting to inhibit the beam motion.

However, perforating the beam reduces L_c to the width between holes. For the same beam above with 4μm diameter holes covering 10% of the available electrode area, the squeeze number is reduced to $\sigma = 3.02 \text{ x } 10^{-4}$, suggesting negligible compressibility of the gas. This means that the air will freely pass through the holes in the beam (with damping), but will not act as an air spring and or cause significant squeeze film damping. With squeeze film damping this low even at 100kHz, this shows that squeeze film won't be a problem for any reasonable dimensions or frequency.

However, there are limitations in the electronic measurement used. Amplification of small signal is limited to lower frequencies. For signals on the order of a tens of nA, commercial amplifiers cannot be found that operate above 10kHz. The cantilever will be operated at the frequency of the first mode, given by

$$\omega_0 = k_1^2 \sqrt{\frac{E}{12\rho}} \left(\frac{t}{L^2}\right) \leq \omega_{max} \tag{3.93}$$

where $k_1 = 1.875$ (corresponding to the 1st mode of fixed-free beam), E is Young's modulus, ρ is the density of the beam, and $\omega_{max}$is the maximum allowed resonance frequency . This tells us that for a given thickness,

$$L^2 \geq k_1^2 \sqrt{\frac{E}{12\rho}} \left(\frac{t}{\omega_{max}}\right). \tag{3.94}$$

Substituting values for silicon, and using $\omega_{max} = (2\pi)10\text{kHz}$, we obtain the following limit on L (note that L is in [μm])

$$L \geq 361.2\sqrt{t} \tag{3.95}$$

This requires long beams, such as the 1400μm long, 15μm thick beam in the third harmonic design below.

3.4 MATLAB optimization

A script was written in MATLAB to enforce all of the constraints described above and maximize the signal to noise ratio and output signal magnitude. While the above expressions show the general trends and can guide and make sense of the results, actual optimization across all the constraints is hard to do.

The MATLAB code uses the *fmincon()* function maximize the signal output and ratio of noise to signal with variations allowed in the thickness, width and length of the beam, the initial gap, and the actuation voltage. The function *fmincon()* is designed to minimize a nonlinear function (or maximize the negative of a function) in multiple dimensions subject to linear and nonlinear constraints within a fixed domain. This is perfect for optimizing the resonator.

The other dimensions were limited to the following domain:

$$L \leq 1500\mu m \tag{3.96a}$$

$$w \leq \frac{L}{5} \tag{3.96b}$$

$$t \leq 30\mu m \tag{3.96c}$$

$$g_0 \leq 4\mu m \tag{3.96d}$$

$$V_{AC} \leq 30V \tag{3.96e}$$

Width is limited to ensure the cantilever deflects like a beam (rather than a plate). The gap and thickness limits are due to fabrication limitations. Cantilever thickness is limited because it is more difficult to make narrow holes (needed to alleviate squeeze film damping) the thicker the wafer is. The gap thickness is limited because thicker PECVD oxides have higher stress and will peel when annealed. The voltage is limited largely because lower voltages are easier to work with, but higher voltages would cause pull-in with the required small gap and thin beams.

The optimization was subject to the following constraints:

$$U_{max} \leq \frac{g_0}{6} \tag{3.97a}$$

$$\omega_0 \leq 10kHz \tag{3.97b}$$

$$i_3 \geq 1nA \tag{3.97c}$$

The first limitation on the maximum deflection places a factor of safety of 2 on the maximum deflection to prevent pull-in. Lower frequency devices are easier to work with; small currents cannot be amplified at frequencies much higher than 10kHz. The final constraint prevented a common situation where the signal to noise ratio was optimized in such a way that the final signal was insignificant.

This yields many possible solutions for each L, and the length with the largest output current was chosen for a predetermined thickness. Once a reasonable set of dimensions was found, important parameters (such as output current, max displacement, and frequency) were double-checked to ensure the optimization had correctly enforced all the constraints.

Despite this, an error was when choosing the final dimensions and the device had a resonant angular frequency of 100krad/s, rather than 10krad/s.

Table 3-2 - Final dimensions and critical parameters for optimized device

Parameter		**Value**
Length (L)		1100μm
Width (w)		220μm
Thickness (t)		15μm
Gap (g_0)		2.5μm
Actuation Voltage (V_{AC})		14V
Hole Spacing ($2r_c$)		6.3μm
Angular Resonance Frequency (ω_0)		100.8rad/s
Resonance Frequency (f)		16.04kHz
Third Harmonic Current (i_3)		23nA
Max Deflection (u_{max})	Static Point Load: (used for optimization)	0.321μm
	Dynamic Point Load: (upper bound)	0.415μm

4 Fabrication

4.1 Overview

Microfabrication of these devices was performed at the Microsystems Technology Laboratories (MTL) at MIT. A schematic of the resonator is shown below in Figure 4-1. The pressure sensor consists of two 6" (150mm) silicon on insulator (SOI) wafers (Ultrasil Corporation). Both wafers had 100nm of thermal oxide grown by the supplier to protect surfaces during transport and facilitate bonding. The bottom wafer consists of a 650μm thick handle layer, 1μm buried oxide (BOX) layer, and a 15μm p-doped device layer (Boron, resistivity of 100-150 Ω-cm). The top wafer consists of a 520μm thick handle layer, 0.5μm buried oxide (BOX) layer, and a 5μm p-doped device layer (Boron, resistivity of 1-30 Ω-cm).

The bottom later consists of the pressure access hole, the cantilever and corresponding electrical connections. The top layer is etched down to leave the cap and a portion of the device layer that contains the other half of the actuation electrodes.

The wafers were processed using bulk micromachining techniques including cleaning, photolithography, and etching (both wet and dry). Ion implantation was performed by the Innovion Corporation to control electrical conductivity. Fusion bonding was used to bond the wafers together. Individual devices were obtained by dicing with a die saw. The final release involved a critical point dry at the Whitehead Institute. The entire fabrication process uses seven masks and eight lithography steps. The following sections detail the fabrication for each layer, bonding and the bonded wafer processing. A detailed process flow can be found in Appendix B.

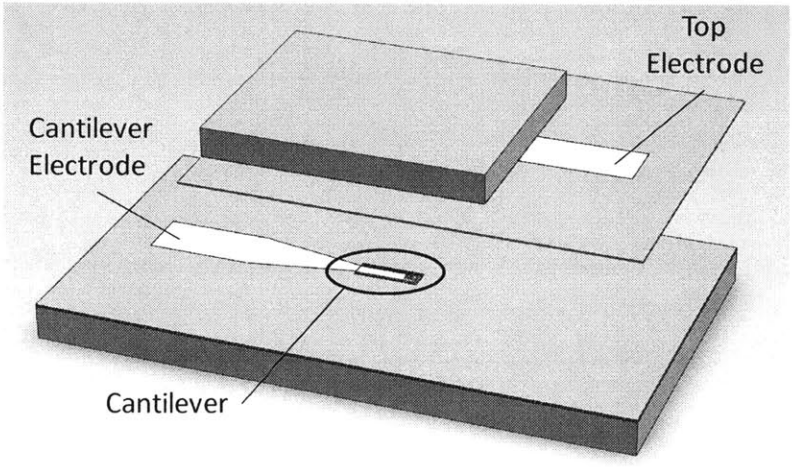

Figure 4-1 – Schematic of fabricated device with wafers separated to show interior features. Yellow indicates highly doped silicon.

4.2 Die Layout

The mask design includes 154 dies. Two major parameters were varied – the size of the holes at the end of the beam (used to control squeeze film damping) and the length (and thus frequency) of the beam.

Holes spaced closer together decrease squeeze film damping. However, they must also be large enough to be easily fabricated in the clean room. The total area of the holes must also be limited (in this analysis to 10% of the total area). This means that larger holes are farther apart and have more squeeze film damping. To find the optimal hole size, four hole diameters were be fabricated. Devices with no holes, 4μm-, 6μm-, and 8μm- diameter holes are divided into four quadrants. This is shown in Figure 4-2.

Additionally, the resonant frequency of devices was varied within each quadrant by incrementing the length of the beam. This is shown within the upper right quadrant in Figure 4-3. The lengths in the other four quadrants are symmetric, i.e. the top row of the bottom right quadrant is the same as the bottom row in the top right. Longer beams would be less stiff, and therefore susceptible to pull-in. The beams were varied from 550 μm – 1100 μm in 50 μm increments. This leads to a frequency range of 101.6krad/s – 406.4krad/s. The lengths and related resonance frequencies are shown in Table 3 below.

The increase in frequency will allow for the study of squeeze film damping across the beams. For the highest frequency, the beam with no holes will have a squeeze number σ = 6.67. This means the squeeze film damping at the tip will play a considerable role in the movement of the beam, because the elastic force of the air will be almost as large as the damping force on the beam.

Table 3 - Length variations and corresponding frequencies

Length [μm]	Frequency [krad/s]
1100	101.6
1050	112.9
1000	122.9
950	136.2
900	151.8
850	170.2
800	192.1
750	218.6
700	250.9
650	290.1
600	3.41.5
550	406.4

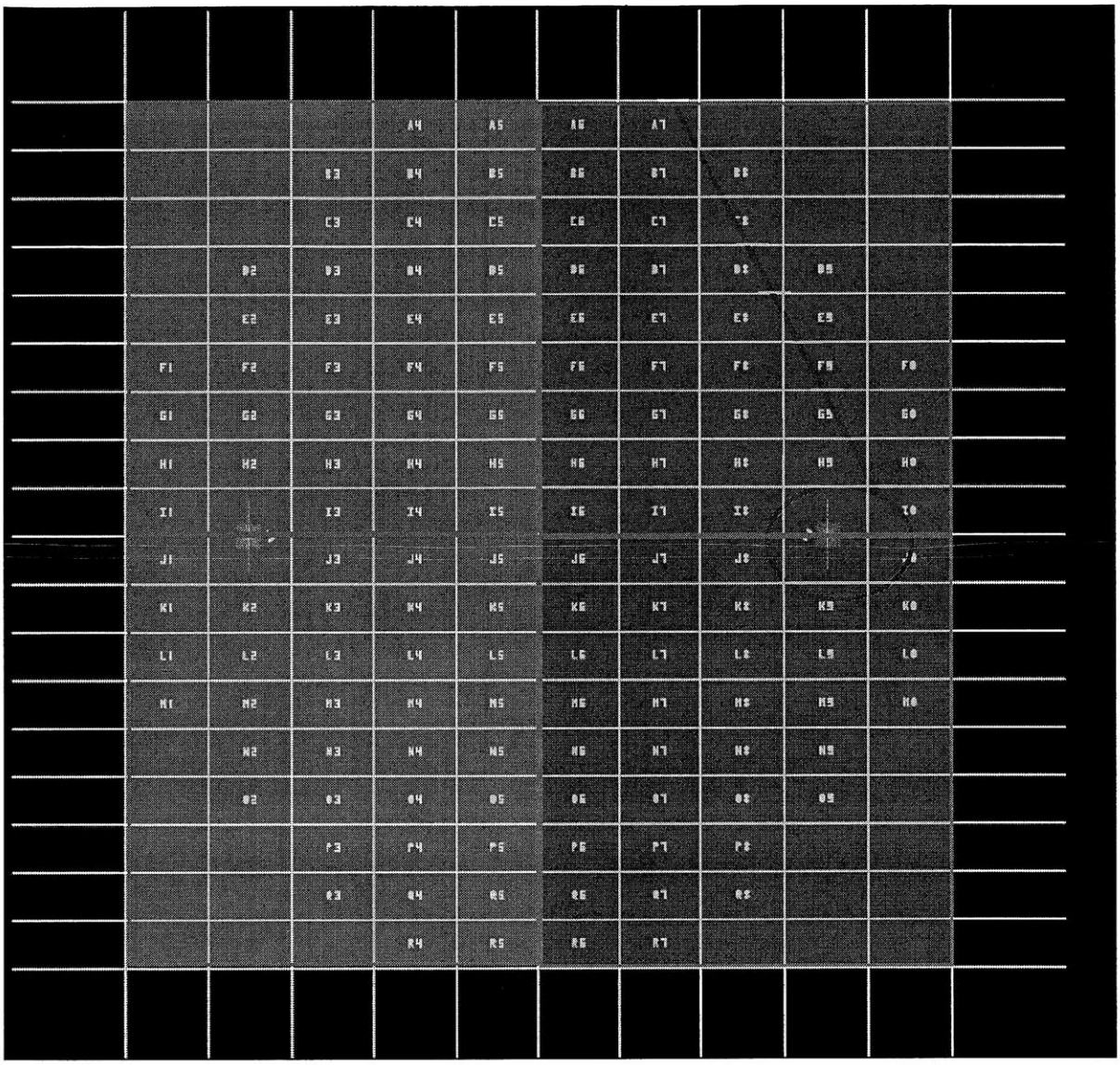

Figure 4-2 – Four quadrants each with a different hole diameters: 8µm holes (red), 6µm holes (orange), 4µm holes (green) and no holes (blue).

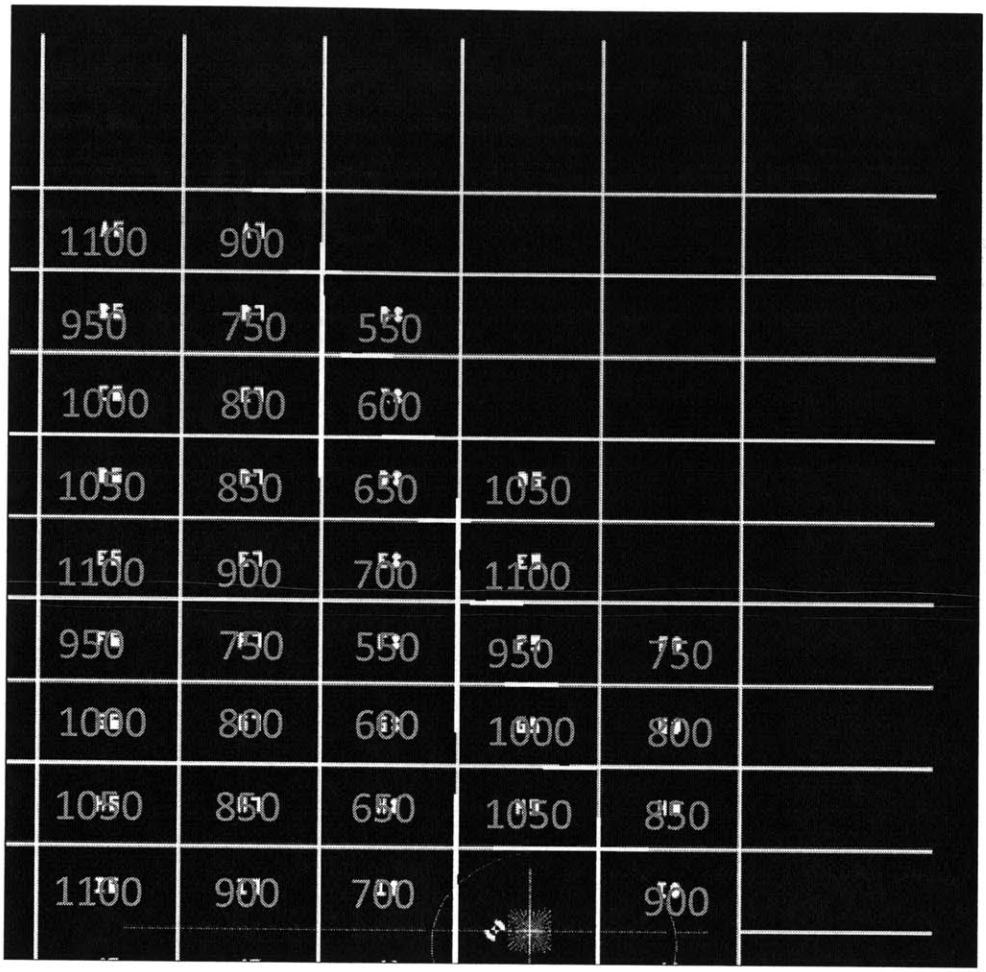

Figure 4-3 -Cantilever length of each die in the upper right quadrant.

4.3 Alignment Marks

Since this device requires aligning several etches on both wafers and bonding them together with precision, alignment marks must be etched before device features. Subsequent masks have complementary features that enable precise alignment with the wafer. A summary of the necessary fabrication steps is shown below in Figure 4-4. The wafers are first patterned with photolithography (HMDS, spin on resist, prebake, expose resist, develop, postbake) using thin resist and the mask "Dicing" shown in Figure 4-5 on the back side. The protective oxide layer was dry etched, followed by a shallow (0.25μm) deep dry etch of the underlying silicon. Finally the wafers were cleaned with piranha. A second set of alignment marks were created on the front side by repeating the process with mask "Resonator_Alignment" (shown in Figure 4-7) and aligning the features on the mask with the alignment marks already etched on the back side. Close-up views of alignment features are shown in Figure 4-7 and Figure 4-8.

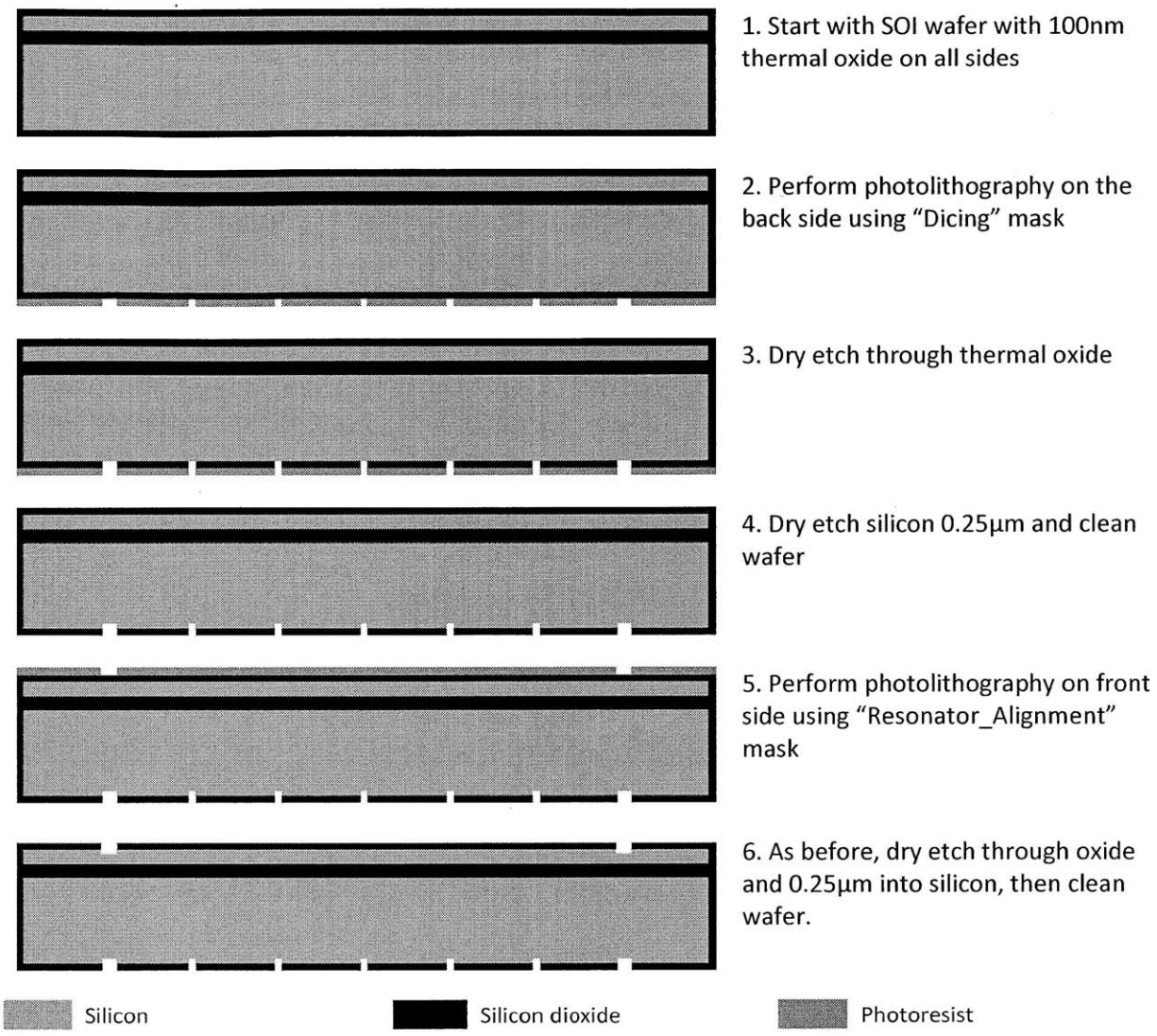

Figure 4-4 - Process Flow for creating alignment marks

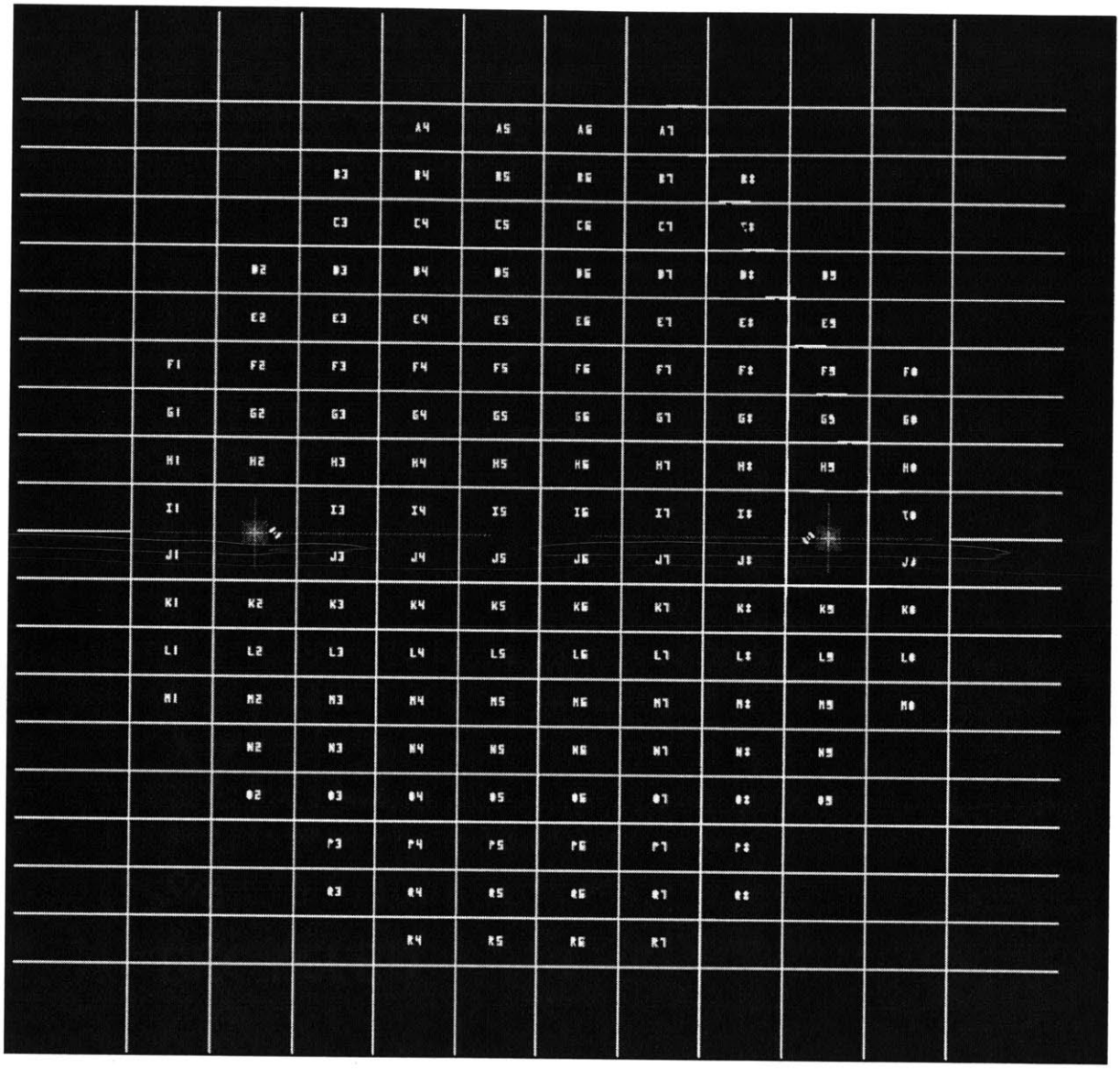

Figure 4-5 – Mask “Dicing”

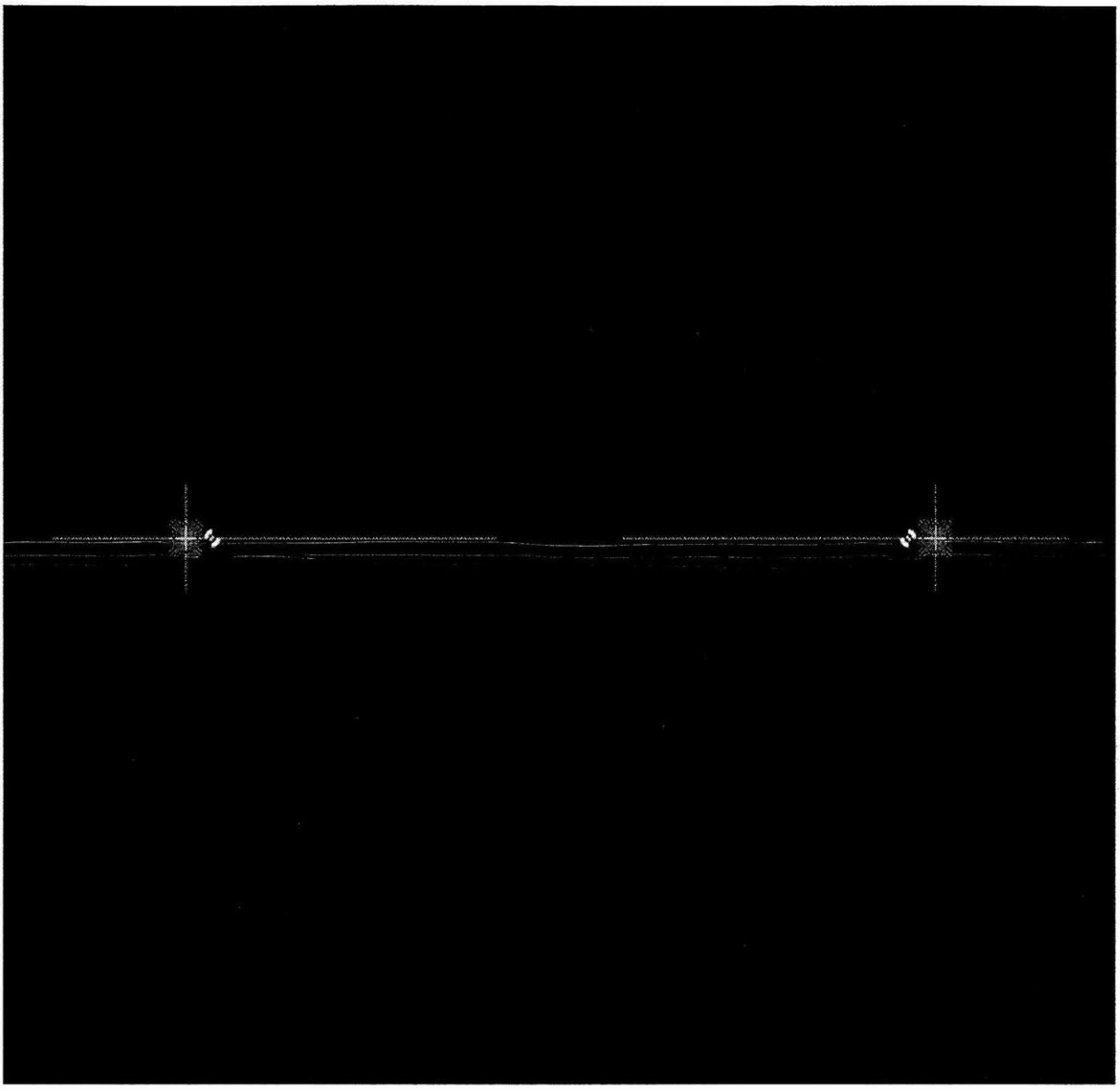

Figure 4-6 – Mask "Resonator_Alignment"

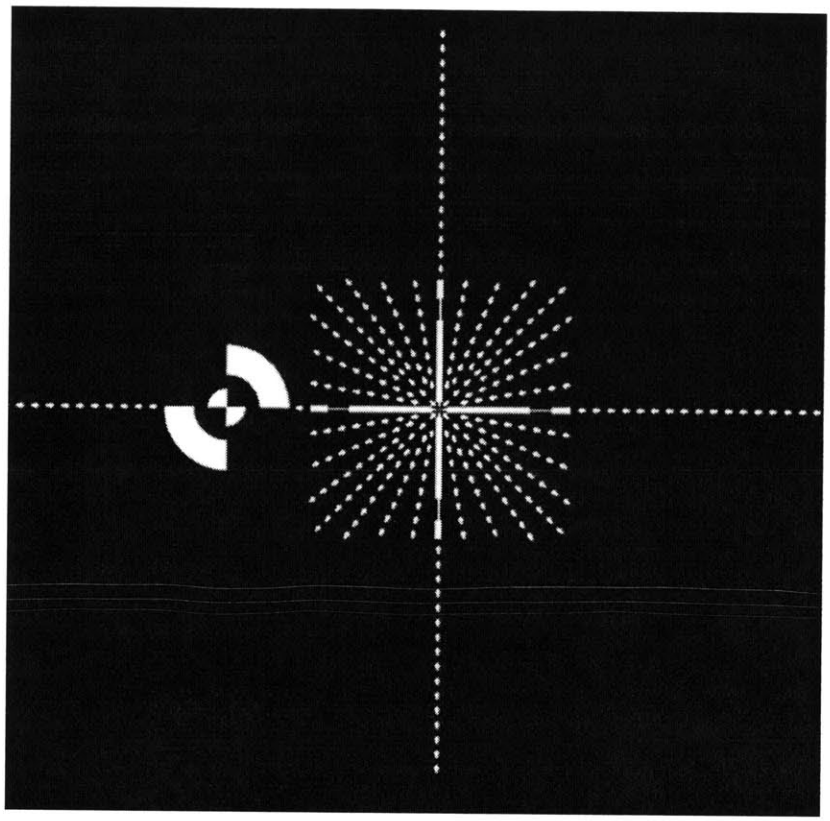

Figure 4-7 - Alignment Marks

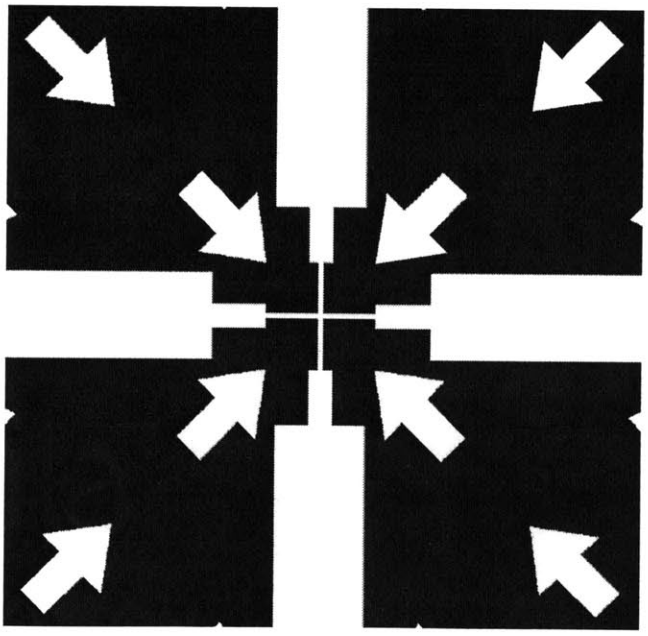

Figure 4-8 - Detailed view of alignment marks

4.4 Bottom Layer

A summary of the fabrication process for the Bottom Layer (before bonding) is shown in Figure 4-9 below. First photolithography is used to pattern thin resist using mask "Cantilever_Electrode" shown in Figure 4-10 with die-level zoom shown in Figure 4-11. The features used to align the mask with the alignment marks are shown in Figure 4-12. Once complete, the wafers were placed back in a clean box, lab tape was used to seal the edges, and the entire box was placed in a resealable bag. This was shipped to Innovion Corp where the wafers were subjected to a heavy boron implant. The dose was $10^{15}cm^{-2}$, with the 100nm oxide protecting the implanted silicon surface from damage and the 1.2μm resist absorbing the ions to prevent unwanted doping of the bulk silicon.

Once the wafers arrived back from Innovion, they were cleaned thoroughly by ashing and double piranha (two consecutive piranha cleans, one blue followed by one green). The wafers were annealed at 1050°C for 1.5 hours to activate the dopants and spread then throughout the device layer. The 100nm oxide layer was then stripped with BOE, the wafers were cleaned in piranha, and a new 3μm layer of PECVD oxide was grown on the surface using the DCVD tool in ICL. While still clean, the wafers were annealed again at 950°C for 1 hour to densify the PECVD oxide film and improve film quality. To smooth the oxide surface for bonding, the wafers were polished using CMP.

The final steps before bonding pattern the cantilever beam. The wafers are subjected to photolithography using mask "Cant_Plus_Holes" shown in Figure 4-15 with a detailed view of the cantilever shown in Figure 4-15. The beam outline is first dry-etched to remove the oxide, then dry-etched again with different reactive gases to etch through the device layer. Since the holes are quite narrow, they etch at a slower rate than the surrounding silicon and care must be taken to ensure that they are completely etched through.

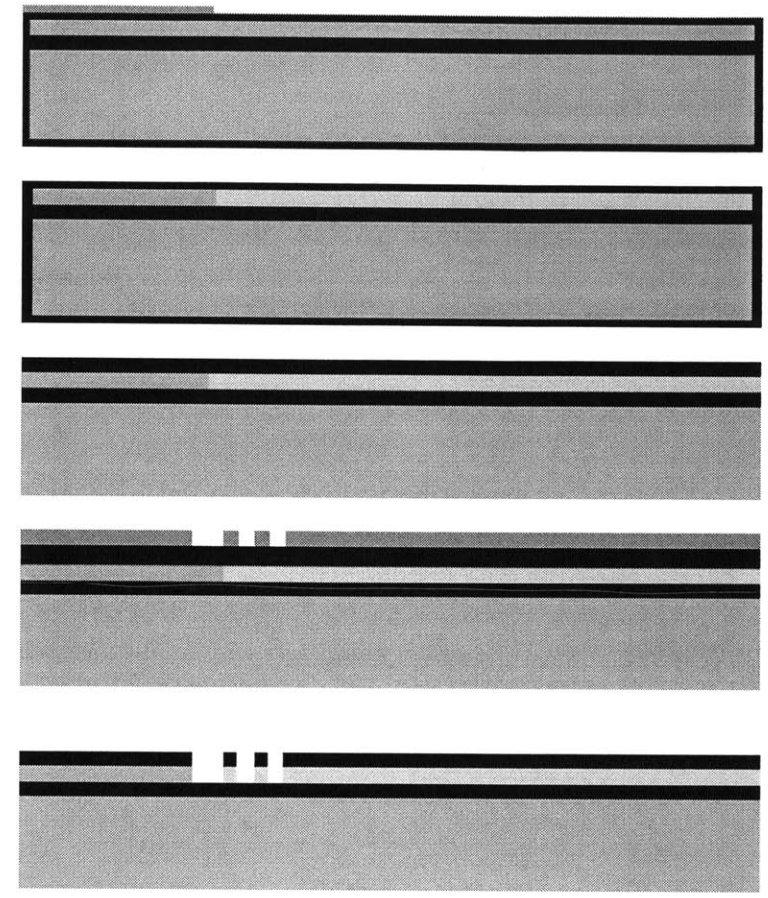

Figure 4-9 – Bottom layer fabrication process

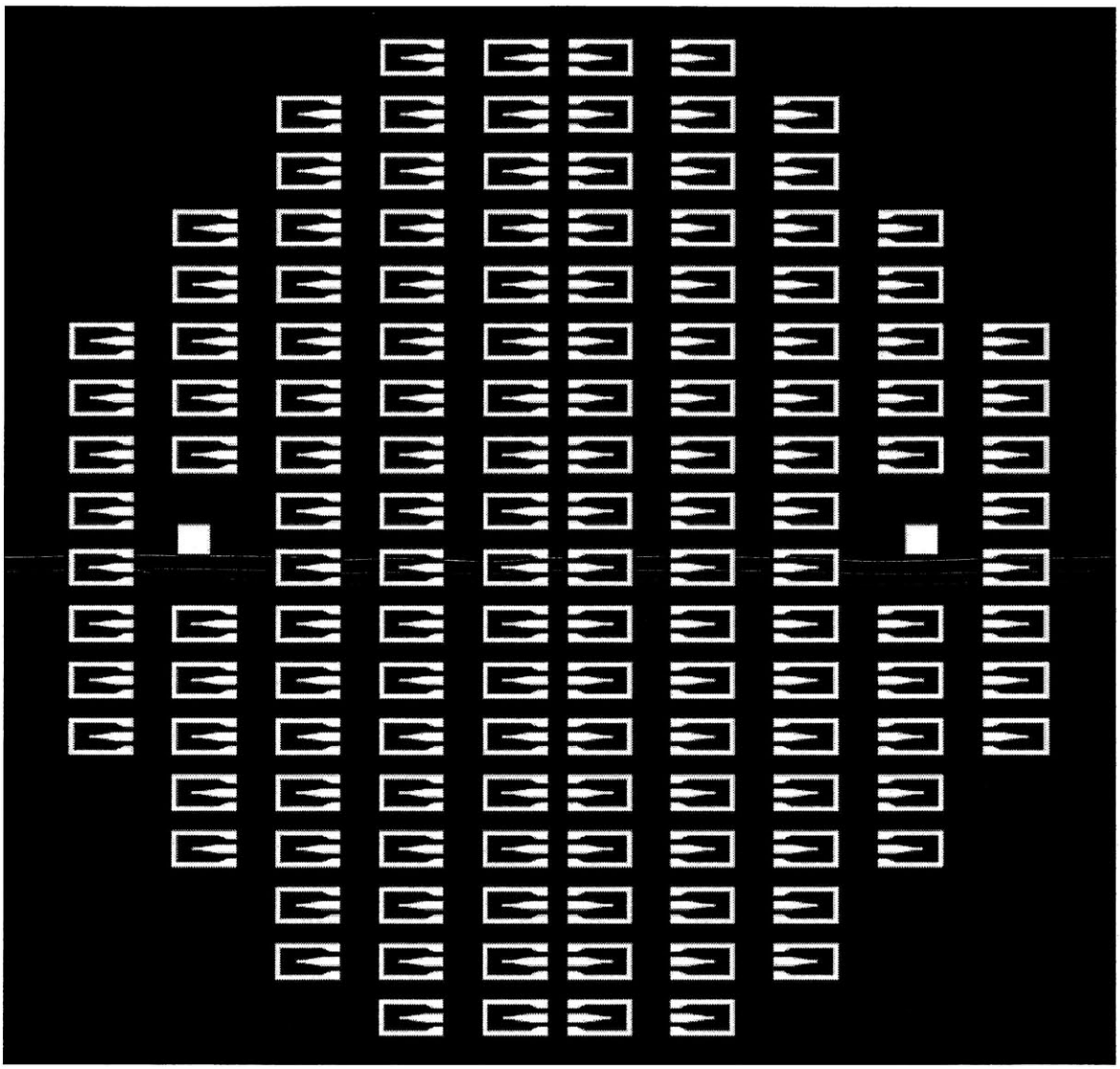

Figure 4-10 – Mask "Cantilever_Electrode"

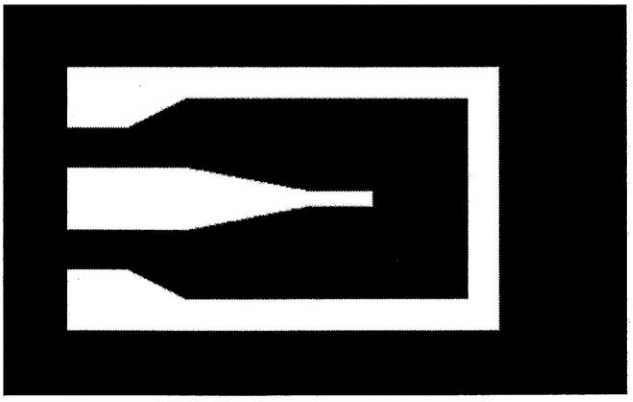

Figure 4-11 - Die level view of mask "Cantilever_Electrodes"

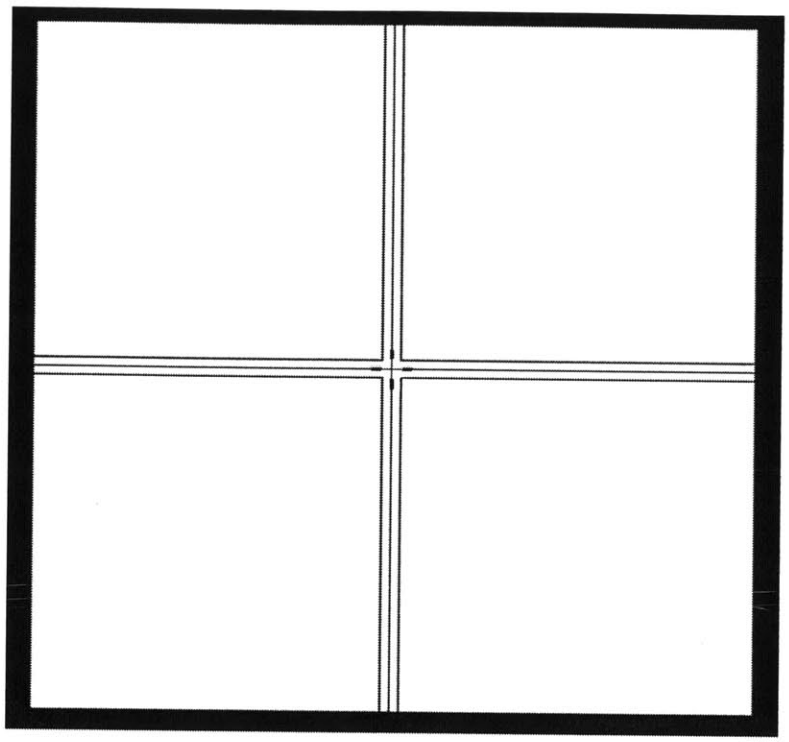

Figure 4-12 - Window used to align masks with alignment marks. The cross lines up with the alignment marks on the wafer, and the window allows for a wider field of view.

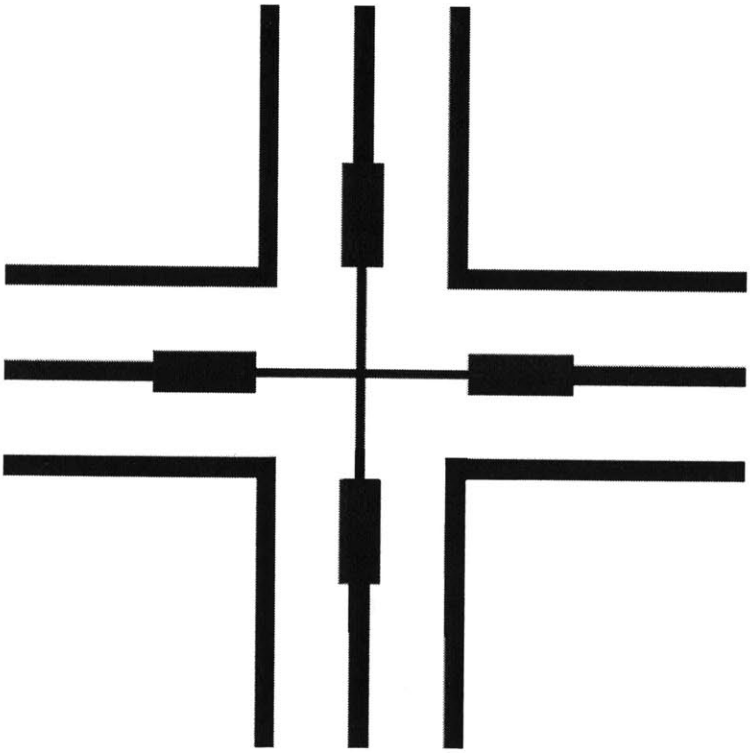

Figure 4-13 - Detailed view of alignment features from previous figure.

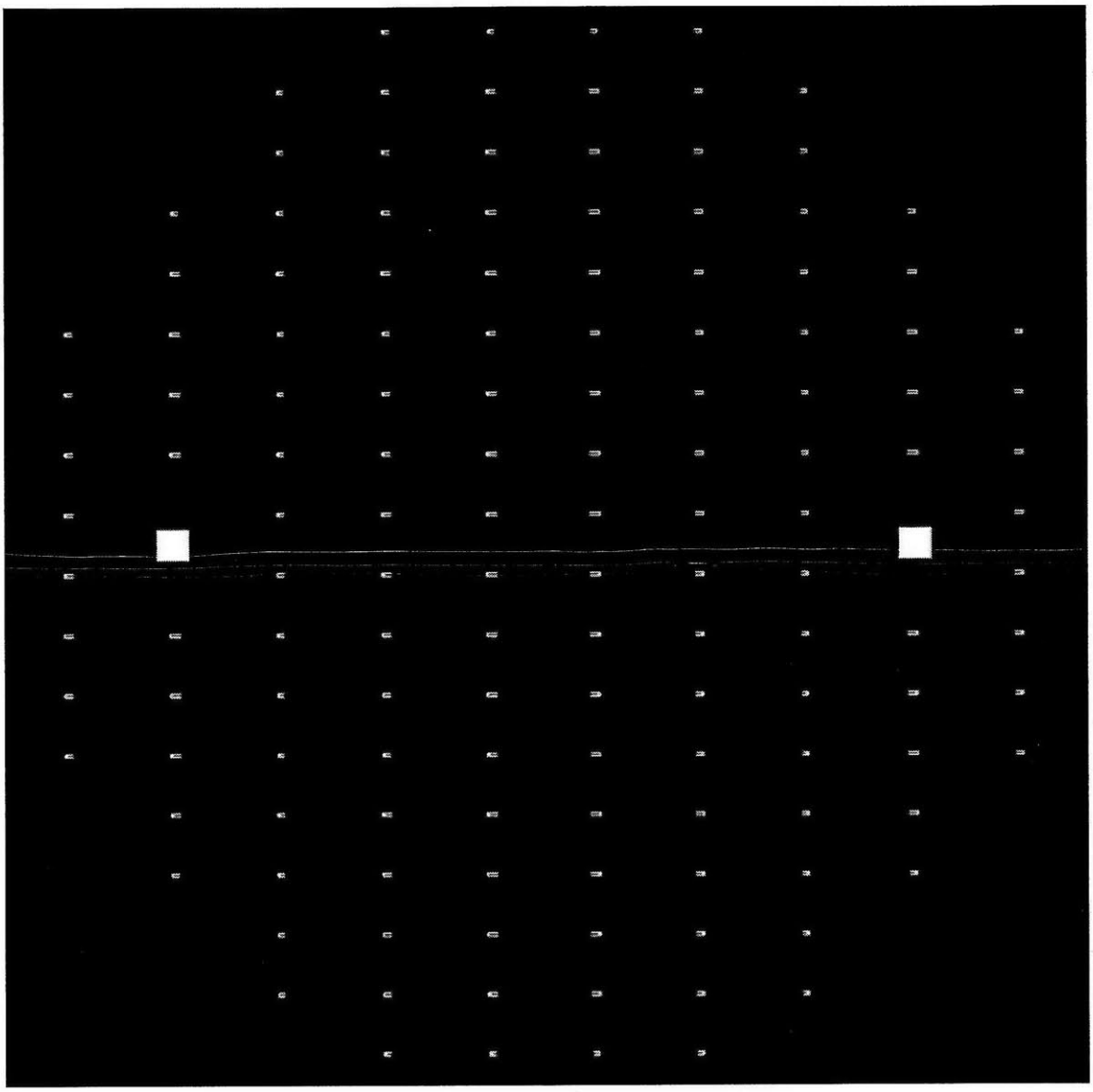

Figure 4-14 - Mask "Cant_Plus_Holes"

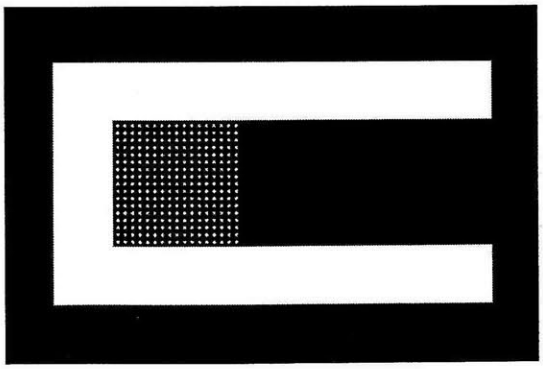

Figure 4-15 - Zoomed view of 750µm long cantilever in "Cant_Plus_Holes" mask

4.5 Top Layer

A summary of the fabrication process for the Bottom Layer (before bonding) is shown in Figure 4-16 below. Many of the processing steps are similar for the top and bottom wafers at the beginning, so the wafers are processed together with separate masks to save time. First photolithography is used to pattern thin resist using mask "Second_Electrode" shown in Figure 4-17 with die-level zoom shown in Figure 4-18. Once complete, the wafers were placed back in a clean box with the bottom layer wafers, lab tape was used to seal the edges, and the entire box was placed in a resealable bag. This was shipped to Innovion Corp where the wafers were subjected to a heavy boron implant. The dose was $10^{15}cm^{-2}$, with the 100nm oxide protecting the implanted silicon surface from damage and the 1.2μm resist absorbing the ions to prevent unwanted doping of the bulk silicon.

Once the wafers arrived back from Innovion, they were cleaned thoroughly by ashing and double piranha (two consecutive piranha cleans, one blue followed by one green). The wafers were annealed at 1050°C for 1 hour to activate the dopants and spread then throughout the device layer. The 100nm oxide layer was then stripped with BOE, the wafers were cleaned in piranha, and a new 3μm layer of PECVD oxide was grown on the surface using the DCVD tool in ICL.

The final steps before bonding etch the resonator cavity and help with the final release. A nested mask is used for this processing. First, the wafers are subjected to photolithography using mask "Nested". BOE is used to etch through the PECVD oxide layer where the cavity will be formed. Then the resist is stripped off using a piranha clean. The wafers are subjected to another round of photolithography using the "cavity" mask. This is followed by a 15μm deep deep-reactive-ion etch (DRIE) through the silicon device layer. Ashing is necessary to remove any C_4F_8 from the sidewalls and surfaces. A BOE etch removes both the BOX layer at the bottom of the DRIE etch and the PECVD layer at the surface around the contacts. A final DRIE etch for 50μm increases the total cavity depth to 65μm. The BOX layer acts as a hard mask to protect the contacts from this etch.

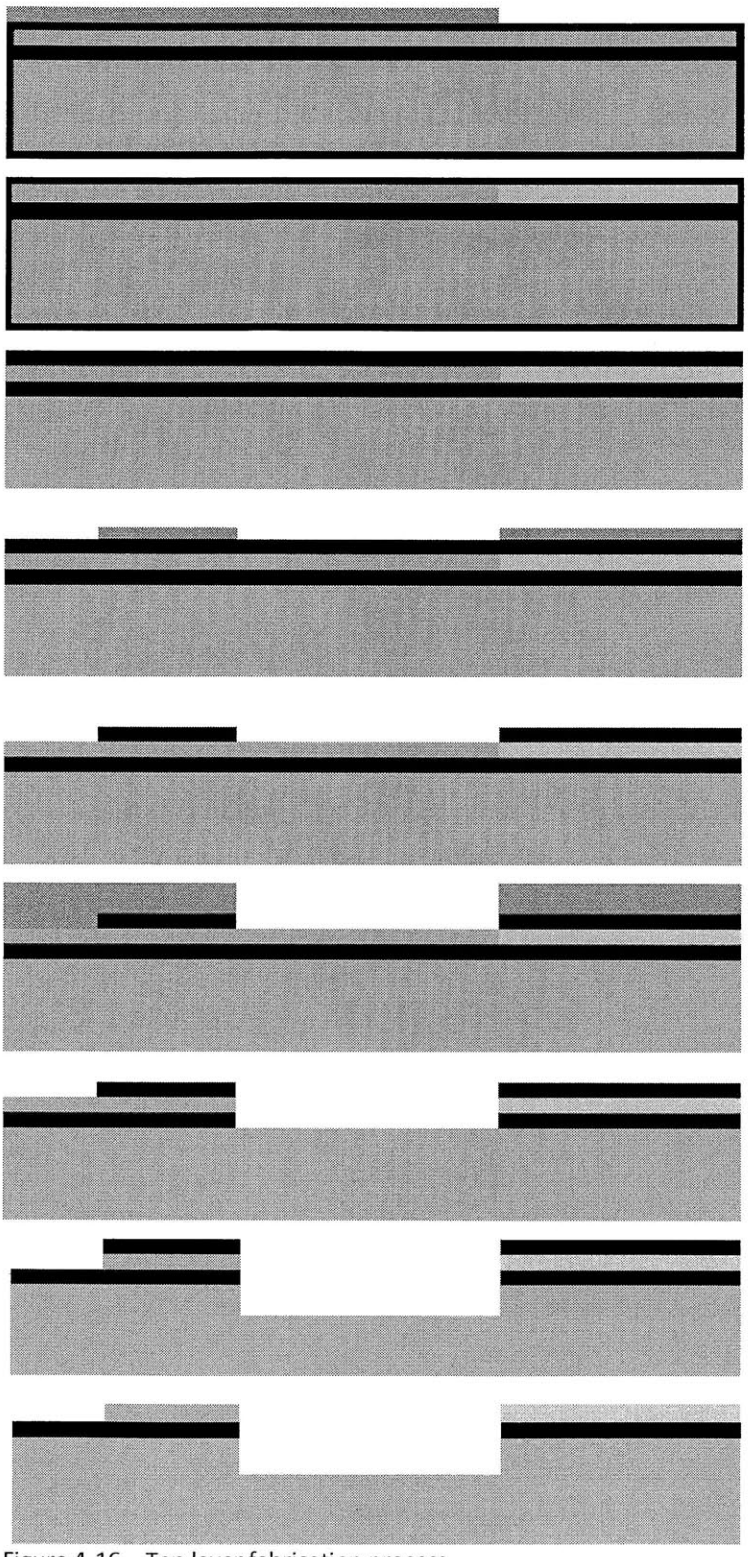

1. Perform photolithography using mask "Second_Electrode"

2. Send wafers to Innovion for implantation, ash, RCA clean, anneal at 1050°C for 1 hour.

3. Strip oxide with BOE, redeposit PECVD oxide, anneal at 950°C for 1 hour, CMP to smooth for bonding

4. Perform photolithography with mask "Nested"

5. Etch through oxide with BOE, clean wafer

6. Perform photolithography again, this time with mask "Cavity"

7. DRIE etch silicon for 15μm, BOX etch stop. Etch through exposed BOX with BOE. Strip resist.

8. DRIE etch silicon again for 50μm, this time deepening the cavity and etching through the device layer.

9. Strip oxide immediately before bonding

Figure 4-16 – Top layer fabrication process

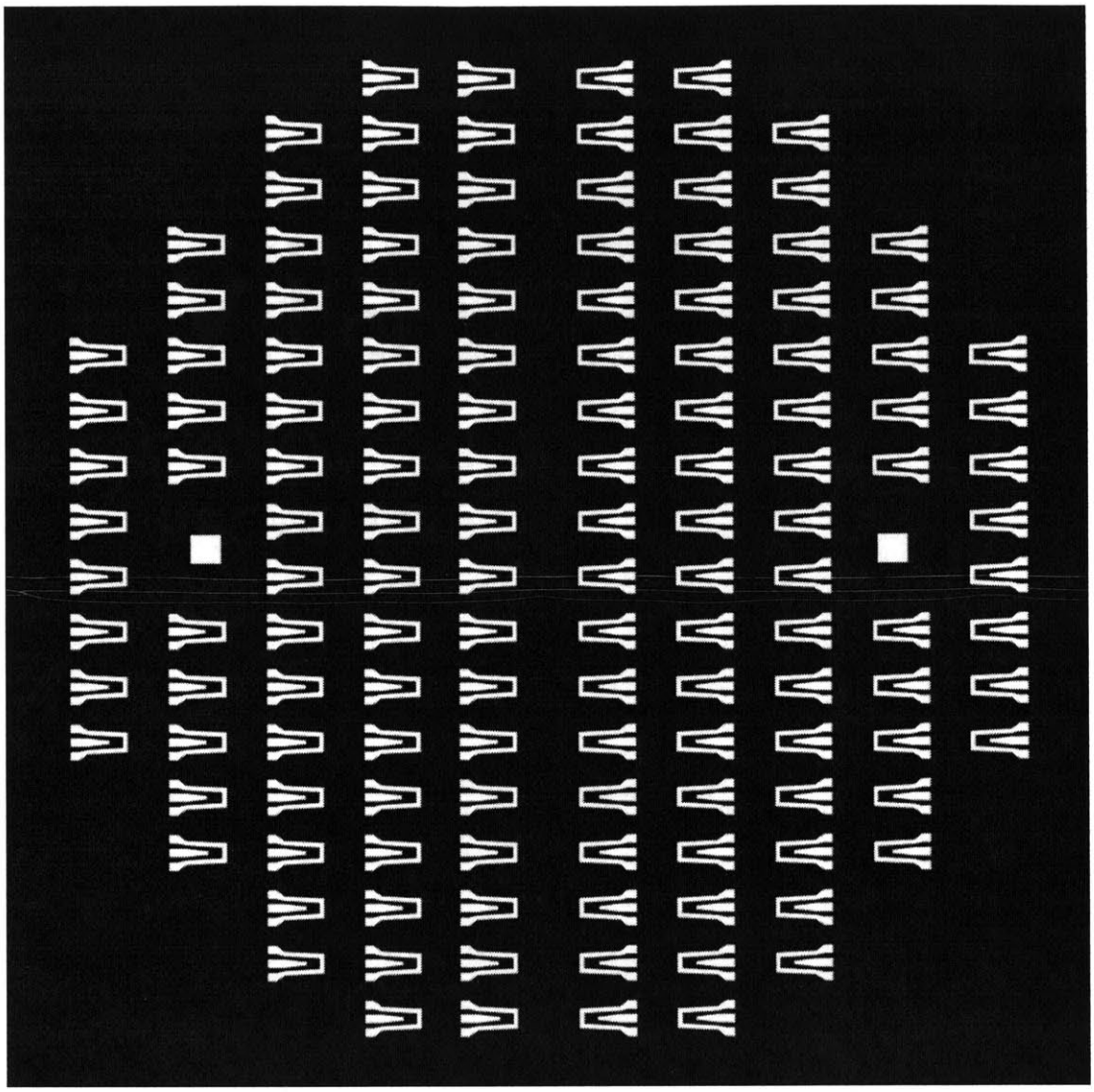

Figure 4-17 - Mask "Second_Electrode"

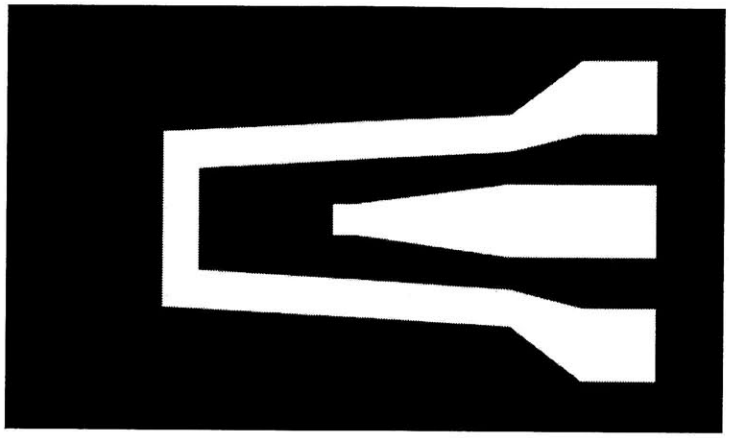

Figure 4-18 - Die level view of mask "Second_Electrode"

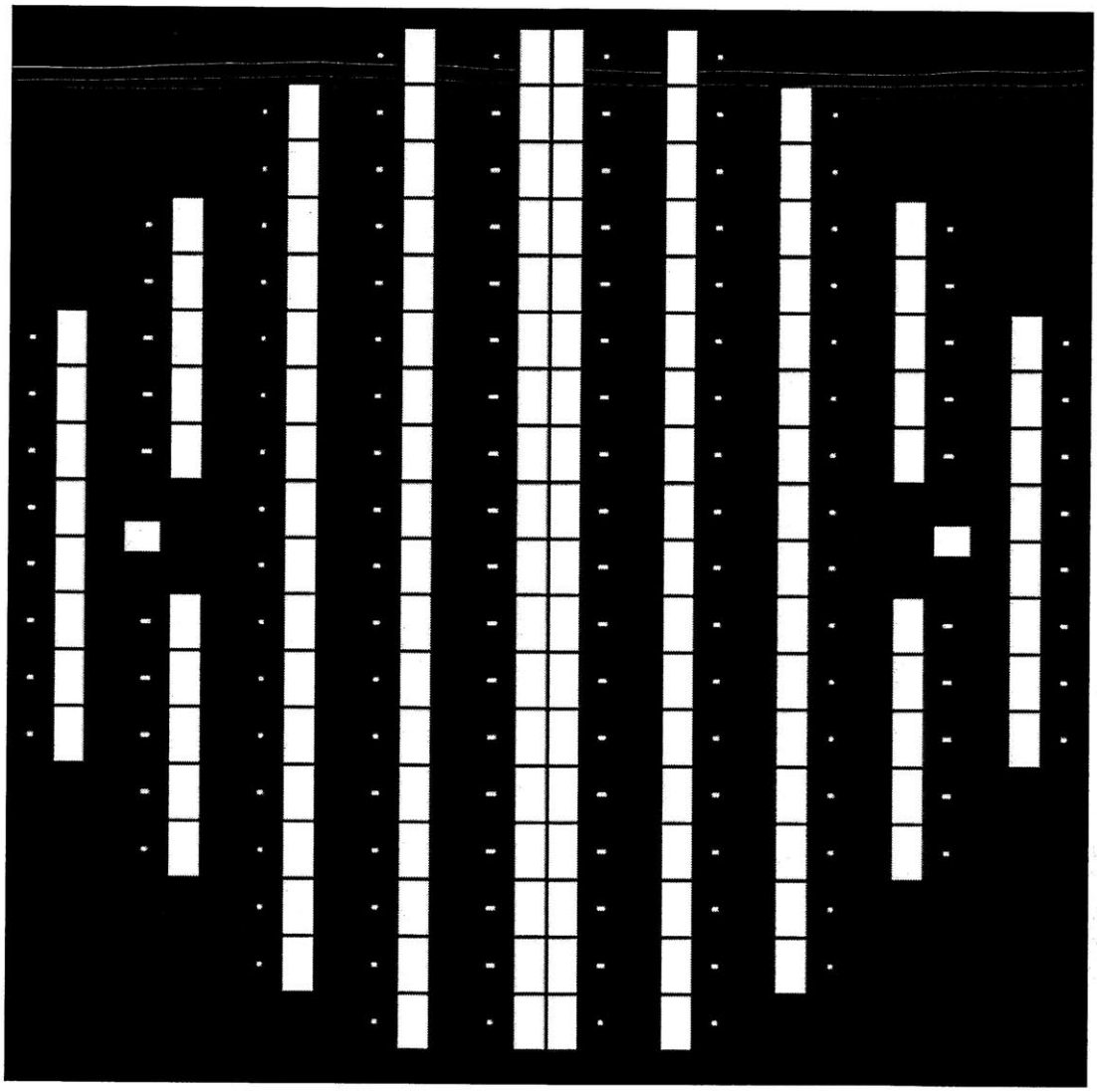

Figure 4-19 - "Nested" mask

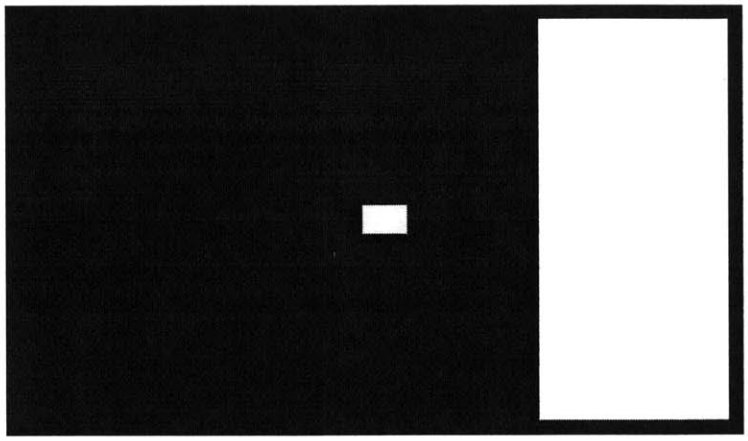

Figure 4-20 - Die level view of mask "Nested"

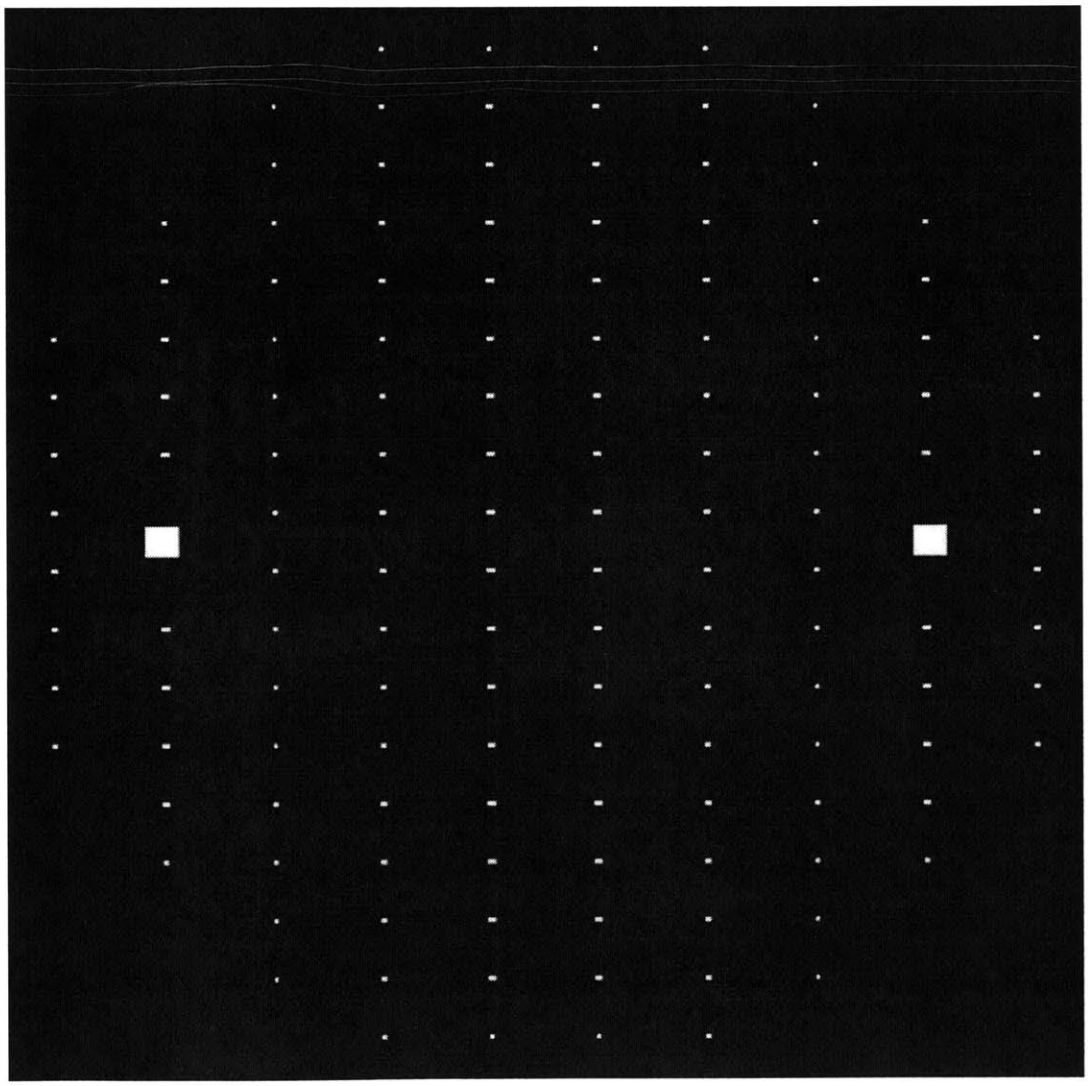

Figure 4-21 - "Cavity" mask

4.6 Wafer Bonding

After preliminary processing to form the interior features on the top and bottom wafers, the wafers were bonded together with the device layers facing each other, as shown in Figure 4-23. To help ensure successful bonding, extra care was taken to ensure that the wafer surfaces remained as clean as possible. The first step was to ash both wafers. The bottom layer was placed in HF to remove the PECVD oxide that had been protecting the surface. This is followed by a piranha clean for both wafers, immediately followed by an RCA clean. The HF dip was skipped for the bottom wafer to prevent undesirable etching of the PECVD oxide film. The time between steps was kept to a minimum to prevent particulates in the air from depositing on the cleaned surfaces

The two wafers were aligned and pressed for 30 minutes. The quality of the bond was checked using an infrared camera. Images of the bond front can be seen in Figure 4-24 below. When a bond was complete enough, or the wafers were bonded over more than 75% of the area, they were annealed at 850°C for 3 hours. In retrospect, more time and/or higher temperatures is advisable for future fabrication attempts. At least 3 hours at 1000°C is usually required; this is equivalent to annealing for 9 hours at 850°C [33]. This is shown in Figure 4-22 below.

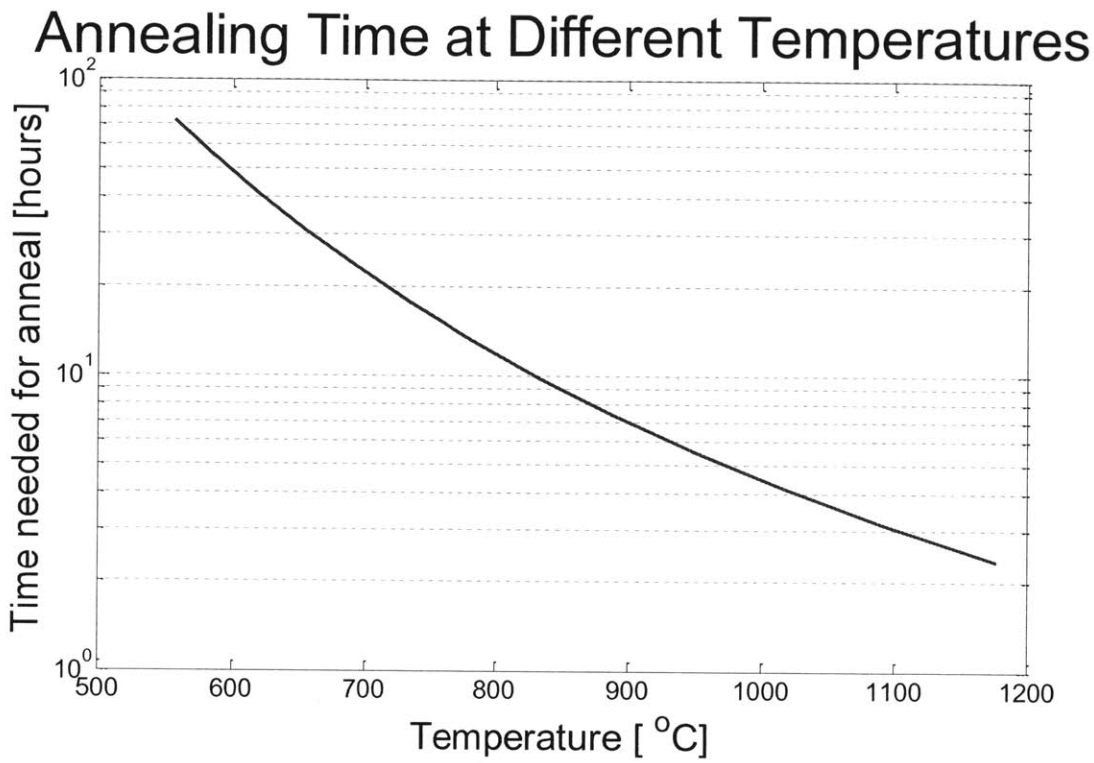

Figure 4-22 - Necessary anneal times based on furnace temperature. These values were scaled assuming that 21.5 hours produces a complete bond at 700°C [33].

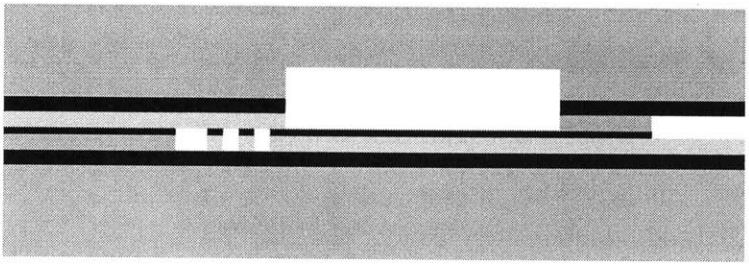

Figure 4-23 – Cartoon showing alignment for fusion bond

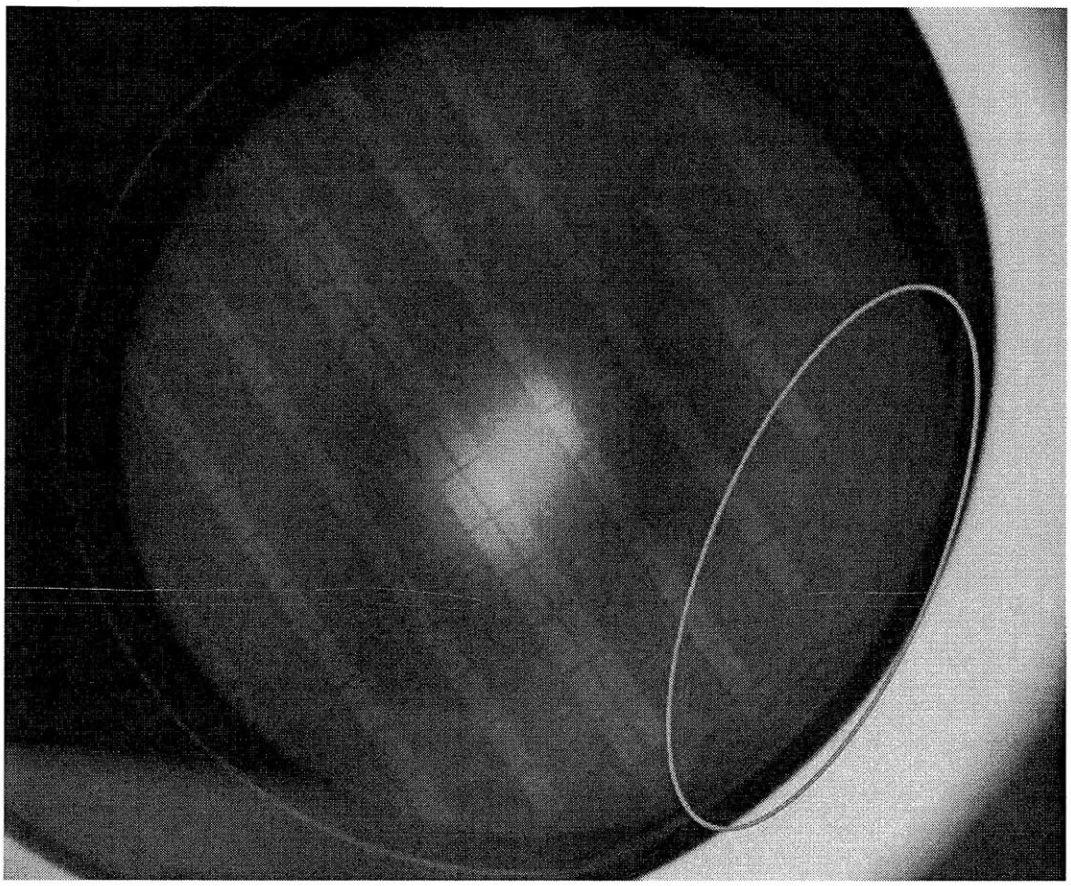

Figure 4-24 – This image shows two wafers after bonding under the infrared camera. The white spot in the middle is the bulb of the light used to illuminate the wafers. The outer black ring is the extent of the wafer, though only a smaller (approximately 4 inch) disc can be seen through the hole in the support. The wafers bonded in the center leaving an approximately 1cm unbonded ring around the edge (shown by the fringes circled in red).

Several factors could have prevented full wafer bonding, including wafer bow due to residual stresses in the annealed PECVD oxide, roughness remaining from the CMP process, and unclean wafer surfaces.

While the wafer bow and CMP induced roughness could not be avoided in this process, dirty wafers were the result of an effort to get finished devices faster. The wafers used for the final device were thoroughly cleaned before bonding, but they had been sitting in wafer boxes for months before being bonded because they were left over from earlier fabrication builds. Previous fabrication attempts resulted in broken or damaged wafers. The top wafers from one build and the bottom wafer from another build survived and processing resumed using the two salvaged wafers. Since the previous builds were abandoned a few steps before bonding, the wafers had been left in boxes for months with the bond surface exposed. They were cleaned before bonding, but it is unwise to expose the bonding surface longer than necessary, and the surface cleanliness was suspect.

4.7 Bonded Wafer Processing and Release

Since the final two etches are deep, photolithography cannot be done after etching because vacuum won't hold them to the vacuum chuck in the photoresist spinner. Therefore photolithography was performed on both sides of the wafer before etching. Since this is a long etch, double-thick resist was used on both sides of the wafer stack (spin once to get 10μm, prebake, spin again for ~20μm, prebake, expose, and develop). The bottom side of the wafer stack was exposed using the "Via" mask shown in Figure 4-26 with individual dies shown in Figure 4-27. Then the front side of the wafer stack was exposed with the "Expose_Electrodes" mask shown in Figure 4-28 with a die level zoom in Figure 4-29. The bottom side is etched using DRIE through the device layer and stopping on the BOX layer. Then the wafer is flipped over and another through wafer DRIE etch is used to remove the upper silicon wafer down to the BOX layer on one side, and the PECVD bonding oxide on the other. All that is left is the wafer cap and a portion of the device layer containing the electrodes.

DRIE is a hot process, and good thermal contact with the helium cooling system is necessary to prevent resist from burning off during the etch. A smoother surface forms a better seal with the helium cooling. Photoresist is considerably rougher than bare silicon, so when photoresist is on the back side of the wafer, helium leaks past the seal and cooling is less efficient. Additionally, regions with poor bonding, such as the edges of the wafer do not transfer heat between the wafers as well and cause hot spots where the resist burns off. This means that even 20μm of resist is not enough to etch through the wafer. Kapton tape was used to cover the caps when the resist burned off to protect regions of the wafer that etched faster than others.

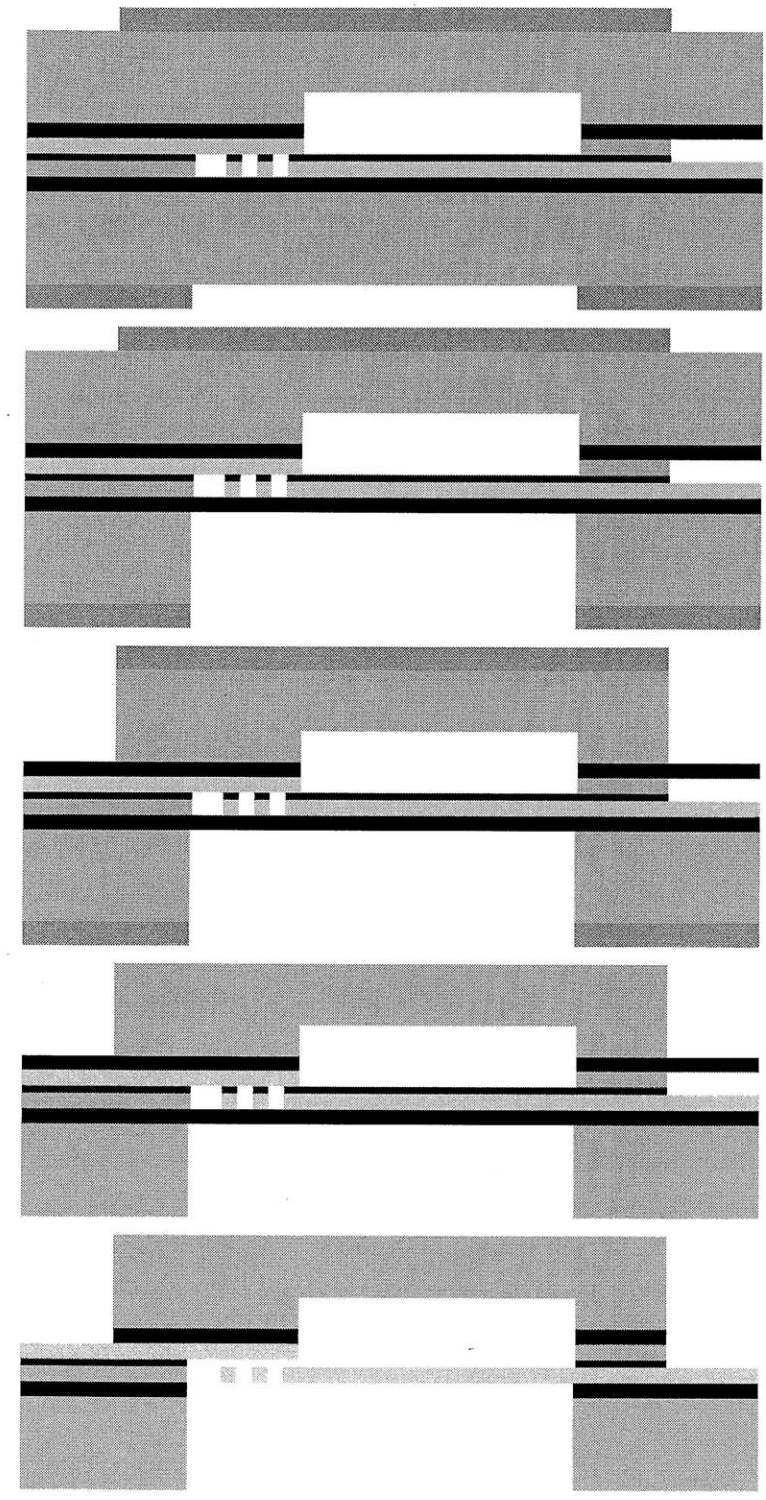

1. Perform photolithography on both sides with double-thick resist. Use mask "Via" on the back and mask "Expose_Electrodes" on the front

2. DRIE etch bottom side through silicon handle wafer, BOX etch stop

3. DRIE etch top side through handle wafer, BOX etch stop. Apply Kapton tape is needed when resist burns off.

4. Strip resist in acetone, ash wafers. Dice wafers.

5. Release dies in BOE. Rinse with water (5x), then dehydrate in ethanol (3x). Critical point dry at Whitehead Institute.

Figure 4-25 – Post-bond processing

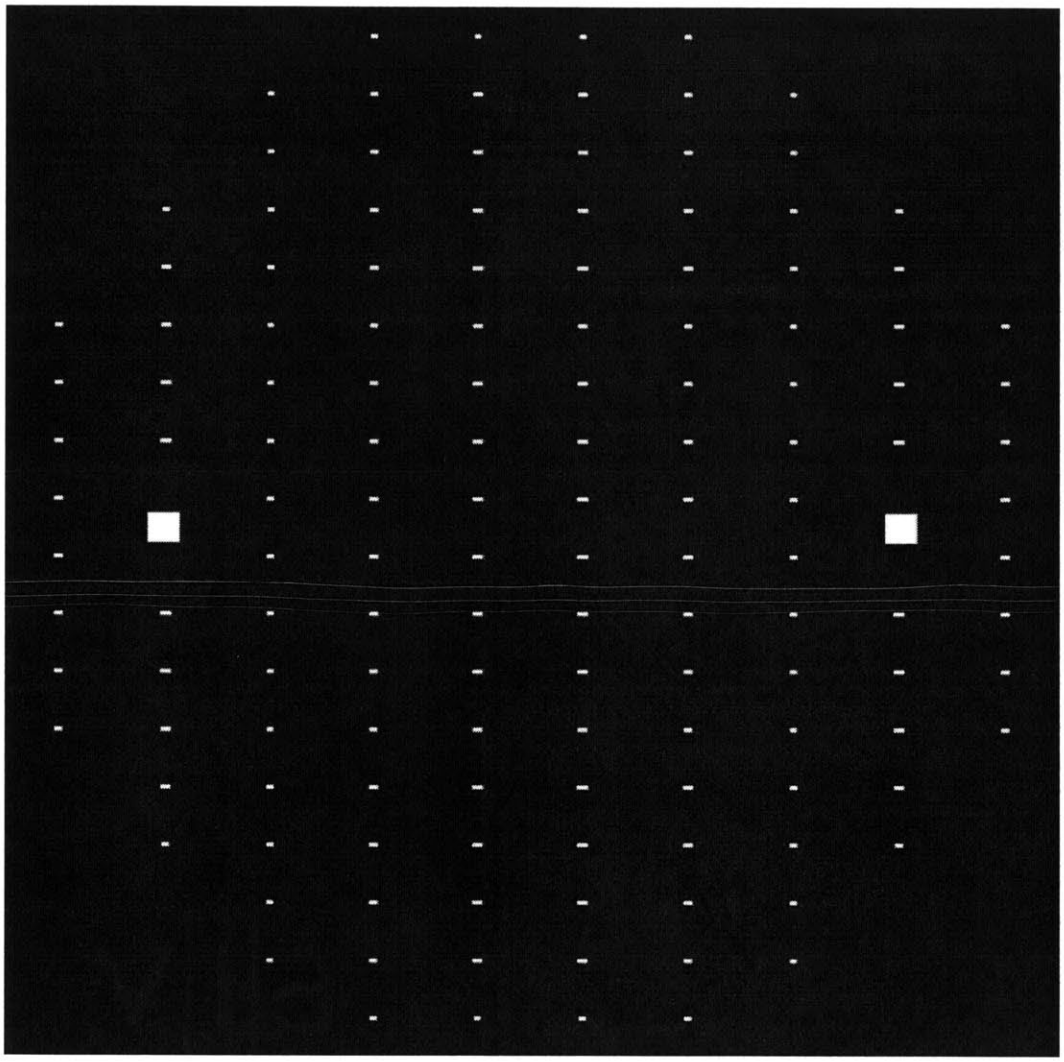

Figure 4-26 - Mask "Via"

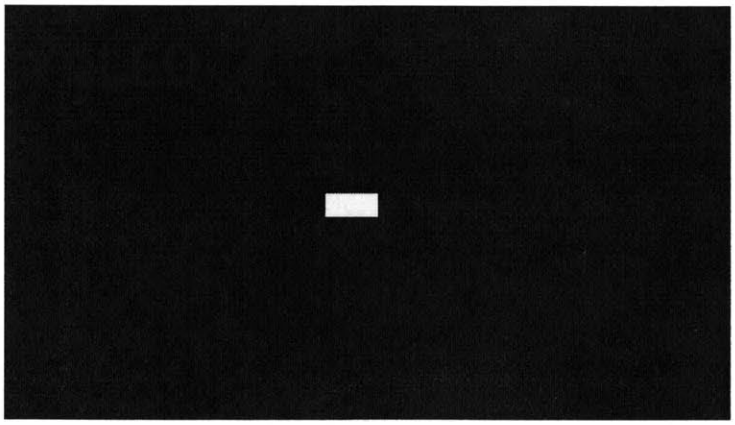

Figure 4-27 - Die level view of "Via" mask

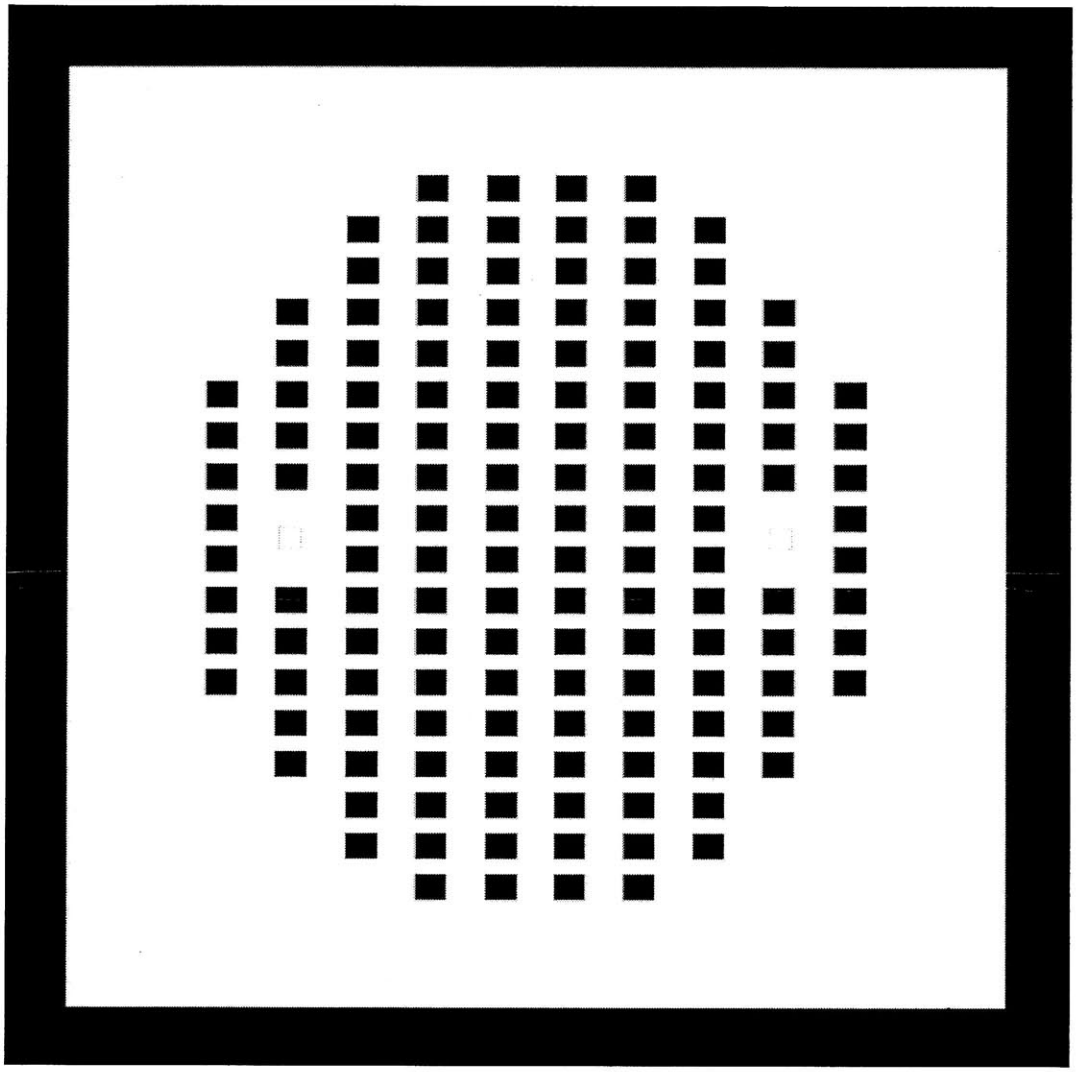

Figure 4-28 - Mask "Expose Electrodes"

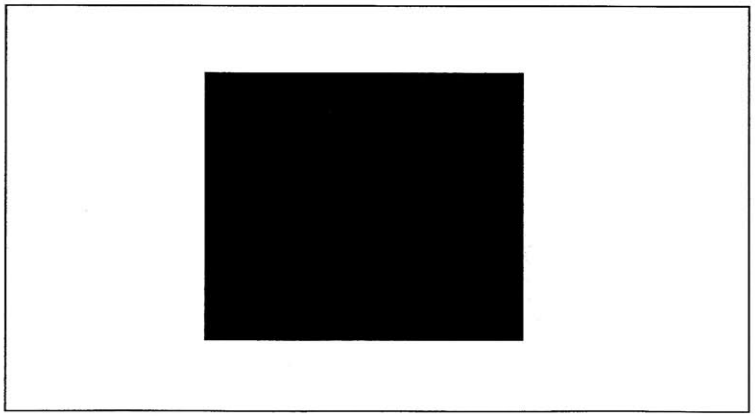

Figure 4-29 – Die level view of mask "Expose_Electrodes"

Following these two etches, the wafers were placed bottom side down on diesaw tape to protect the vias from water and particulates created during dicing. The wafer stack was cut along die-saw lines on the top side of the bottom wafer that had been exposed during the last DRIE etch. The die-saw cut 500μm deep, leaving a thin support of silicon between samples, and the dies were snapped apart by hand. This placed less stress on the cantilevers, and decreased the risk that individual dies would partially peel off the tape and particulates from the dicing would enter the via.

The final steps release the cantilever beams. Dies were placed in 49% Hydrofluoric Acid (HF) for 15 minutes. This was followed by five rinses in fresh beakers of DI water. When satisfied that the HF was completely removed, the dies were placed in pure ethanol, once again using three separate beakers to rinse away the water and fully dehydrate the samples. Finally the dies were brought to the Whitehead Institute for critical point drying in CO_2.

The cantilever can be seen through the via hole as shown in Figure 4-30, both before and after the release etch. A complete microfabricated device can be seen in Figure 4-31 below. The roughness and chipping at the edges comes from the die-saw.

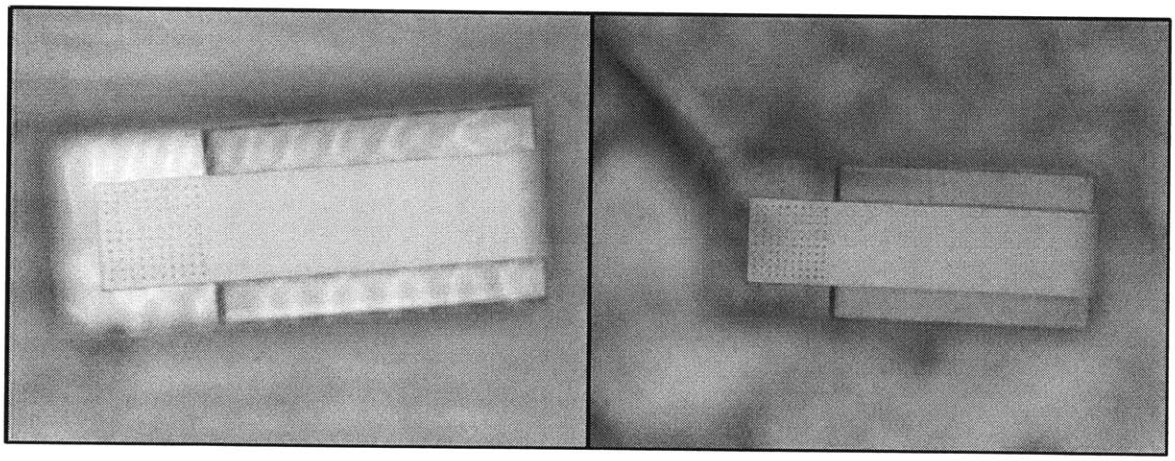

Figure 4-30 – Before and after release of cantilevers. The oxide layer can readily be seen in the left image, with residual stress causing a periodic rippling.

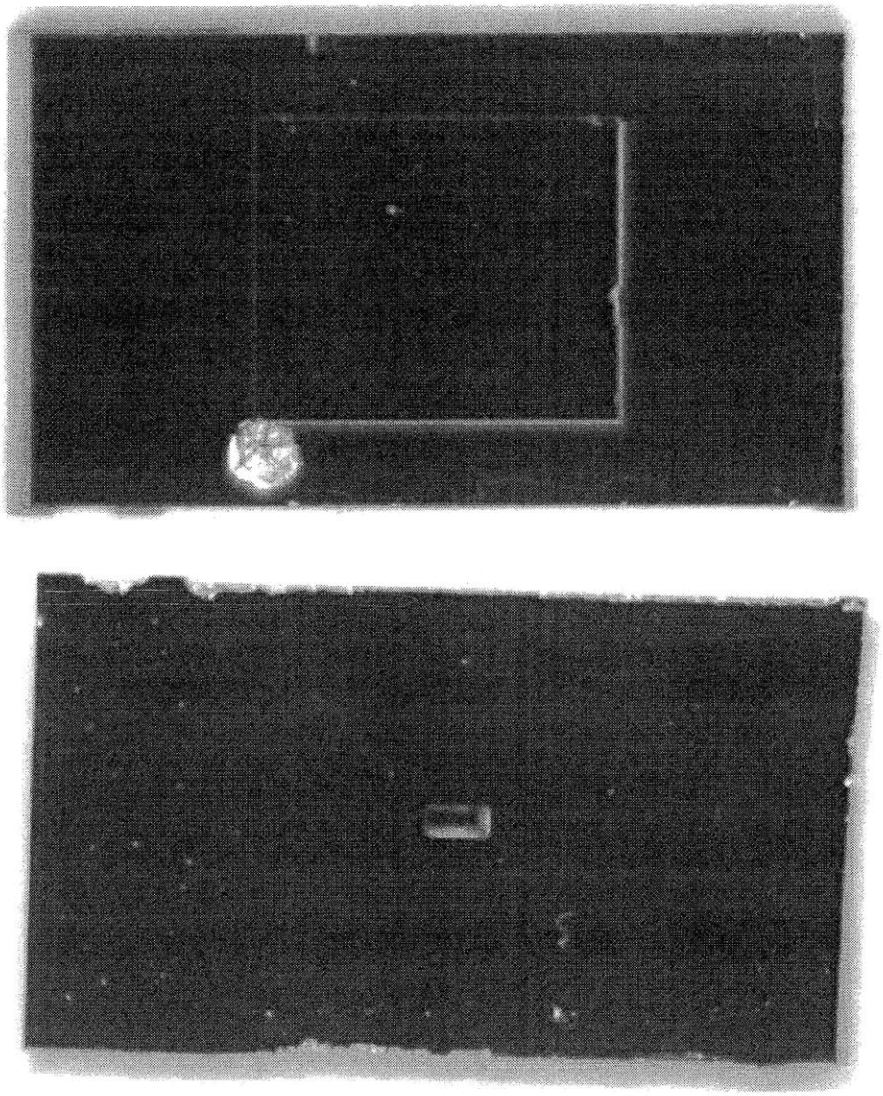

Figure 4-31 – Top and bottom views of a microfabricated device.

5 Testing

5.1 Test Setup

The test setup can be seen in simple block diagram form in Figure 5-1. There are two main functions of the design:

1. *Controlling the pressure* (related components are shown in blue).
   Pressure is maintained in flow control, which means that the pressure is determined by the equilibrium between the vacuum pump removing air and the amount of air that gets through the *MKS 248A flow control valve* (10 sccm maximum flow rate). A *MKS 910 series absolute* pressure sensor is constantly feeding the pressure back to the computer via the NI-PCI 6221 DAQ card and the valve flow rate is modified accordingly.
2. *Measuring the resonance frequency of the device* (shown in yellow).
   A *Signal Recovery 7265 Dual Phase DSP Lock-in Amplifier* was used as both a signal source and to process the signal to pick out the third harmonic. A large 800kΩ resistor was used to convert the current to a voltage and amplify the signal.

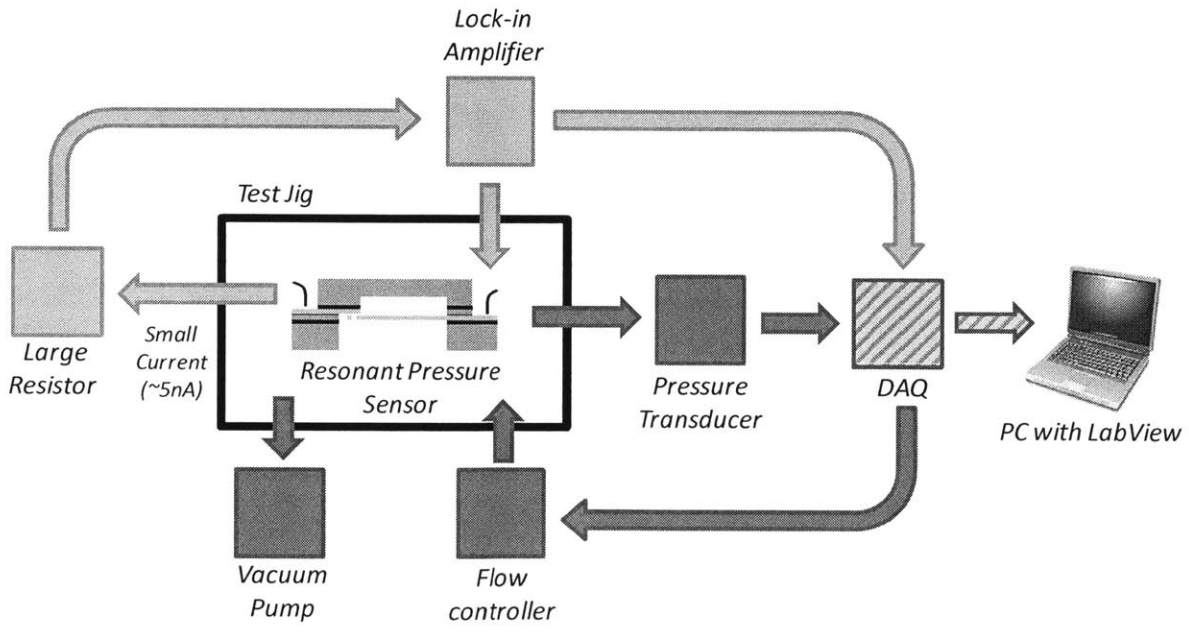

Figure 5-1 - Testing block diagram

A specialized test jig was machined from acrylic and aluminum to position the MEMS sensor for electrical contact and connect the access hole to the vacuum pump and pressure sensor. The jig is made from two parts: an aluminum base and a transparent acrylic cap.

The base is made from aluminum, measuring 3 in square and 1.75 in in tall. A rectangular cut (12.3 mm x 7.4 mm, giving 0.5 mm clearance on each side) with an O-ring groove was milled in the top side of the aluminum base to hold the device. The O-ring both provides creates a seal around the via and distributes pressure on the base of the chip. A hole was bored from the bottom to the device location, and a second hole was bored from the side to meet the first. Two KF-25 flanges were welded over the holes to allow easy connection to the vacuum pump and pressure transducer. An O-ring sits in a groove within the rectangular inset and provides a leak-free seal between the device access via and the pressure control loop. This is shown in Figure 5-2.

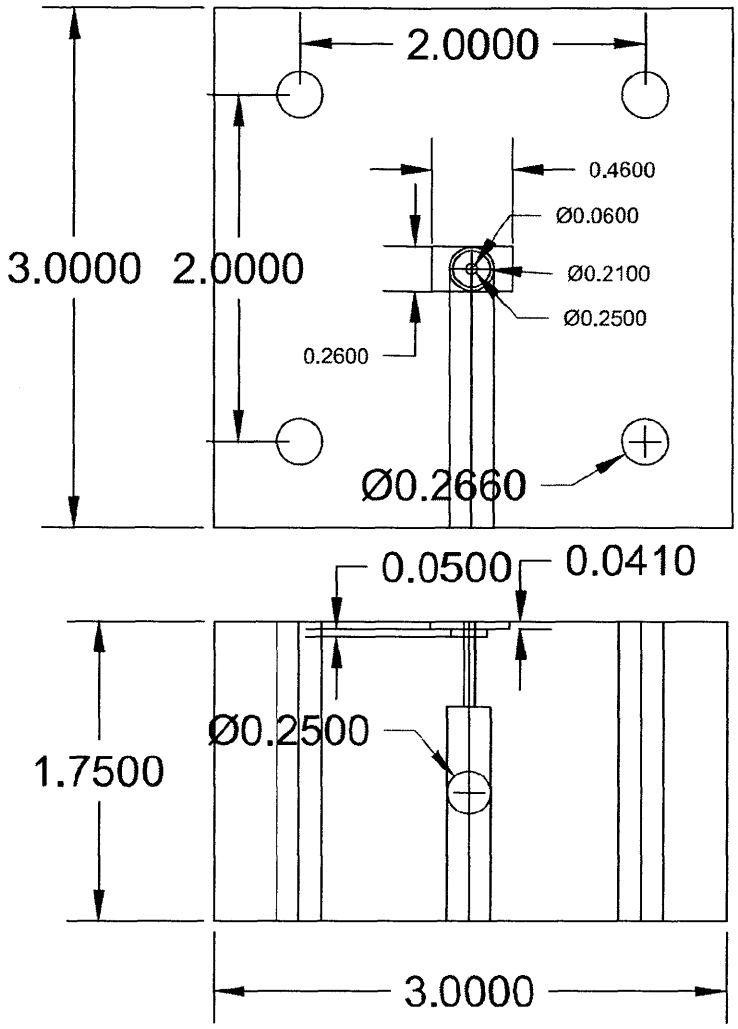

Figure 5-2 – Diagrams showing aluminum base for test jig, a top view on top and a side view on bottom. Dimensions are given in inches.

The cap is machined from acrylic, measuring 0.383 in thick and 3 in square. Another O-ring groove was milled in the bottom. An O-ring inserted here distributes pressure from clamping the test setup to protect the device. Holes that hold pogo pins have been bored through the acrylic in two steps. First, a wider 0.04in hole is drilled from the bottom, stopping 0.5 in from the top. The hole is completed by drilling a narrower 0.022 in hole from the top, meeting the first hole. This allows the pogo pins to enter the bottom hole to a specified depth, with the pin at the top extending out of the cap. A diagram of the acrylic cap is shown in Figure 5-3. One end of the pin presses against the doped contact pads and the other end extends out the top of the cap for electrical access, as shown in Figure 5-4 below. A side view highlighting the path through the resonator is shown in Figure 5-5.

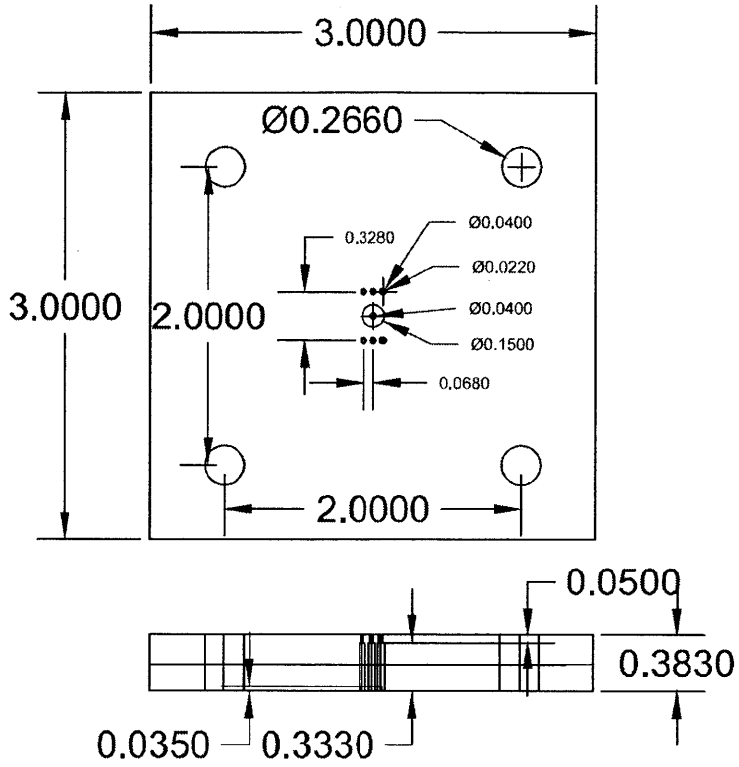

Figure 5-3 – Diagrams showing acrylic test jig cap, with a top view on top and a side view on bottom. Dimensions are given in inches.

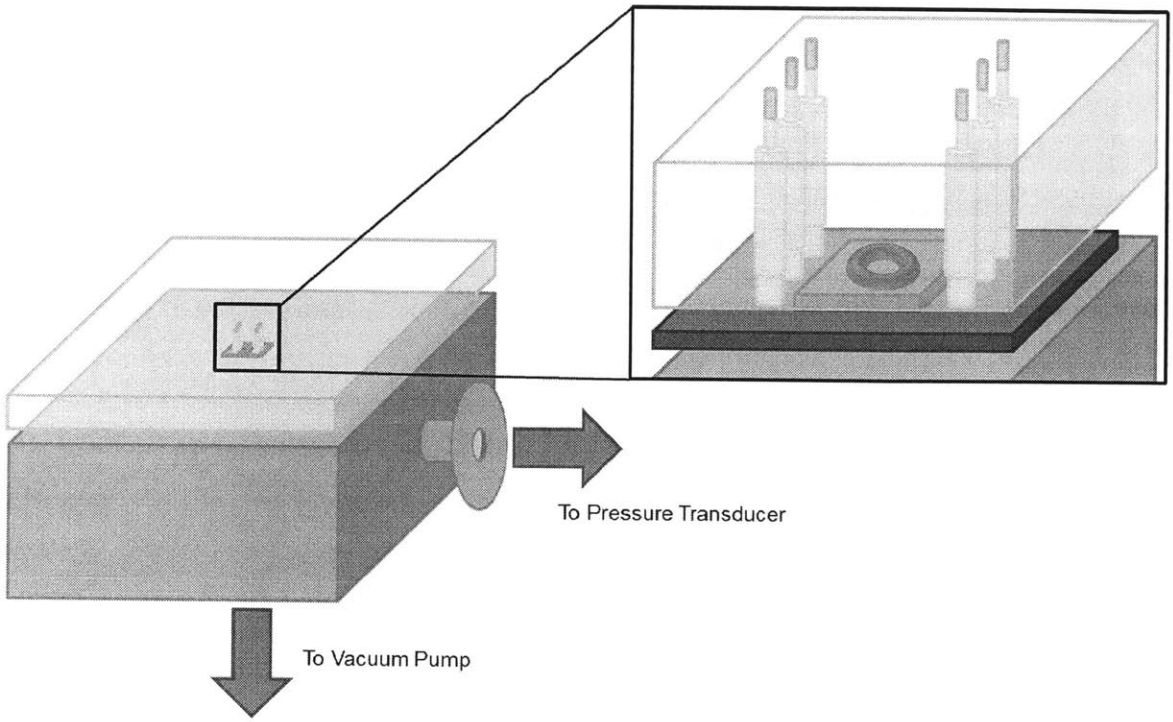

Figure 5-4 - Schematic showing placement of pogo pins in test jig.

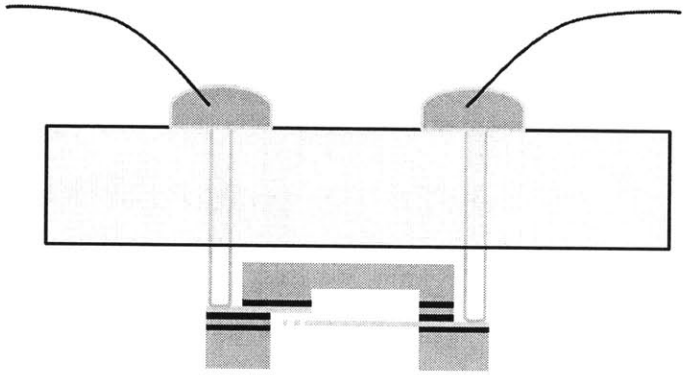

Figure 5-5 -A cartoon cross-section of the device and electrical connections, highlighting the intended current path. Wires attached with conductive epoxy to pogo pins allow electrical contact with the device.

To improve contact with the pogo pins, conductive silver epoxy was used to bond the top of the pin to the connecting wires. Extra bends in the wires were taped to the cap surface to provide stability, and prevent the wires from twisting and breaking the connection. This is shown in Figure 5-6.

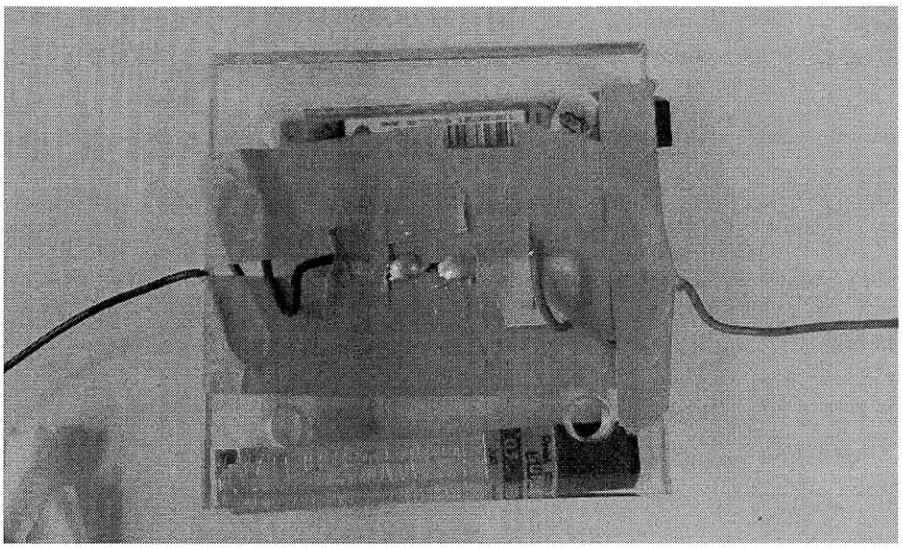

Figure 5-6 – Wires attached to pogo pins with conductive silver epoxy and taped to acrylic cap to provide stability.

5.2 Results

5.2.1 Leak Testing

The poor condition of the wafers and a short, lower temperature anneal had claimed some dies in the clean room. Some caps peeled off the lower wafer during the final DRIE etch, and many more fell off during dicing. This initially posed a concern beyond broken devices: would the surviving dies still be hermetically sealed? To answer that, the first test performed on released dies was a leak test to assess the quality of the seal.

First a blank die the same size as the devices was tested to provide a baseline. This silicon piece was from the edge of the wafer, so it had no cap (and no via etch), but had undergone the same processing as all the other devices. Once concern is that this die was only one wafer (or 650μm) thick so it wouldn't compress the O-rings fully. However, it still provides a useful comparison.

The vacuum pump was turned on and allowed to run until the pressure stabilized at around 2mTorr. After waiting several minutes, the pump was turned off and the pressure was monitored to determine the leak rate. The same procedure was performed with two complete devices (this time only finger tight). The results can be seen for the blank die in Figure 5-7 and for two full devices in Figure 5-8.

After an initial rapid increase in pressure, the rate stabilized to a fairly linear pressure increase. While the linear regime on all three dies starts at a different pressure, the leak rate once stable is almost indistinguishable. Since the measured leak rate for complete devices is

similar to the blank die, it suggests that leakage is due to the inherent leakage from the test jig rather than air passing under the bonded cap.

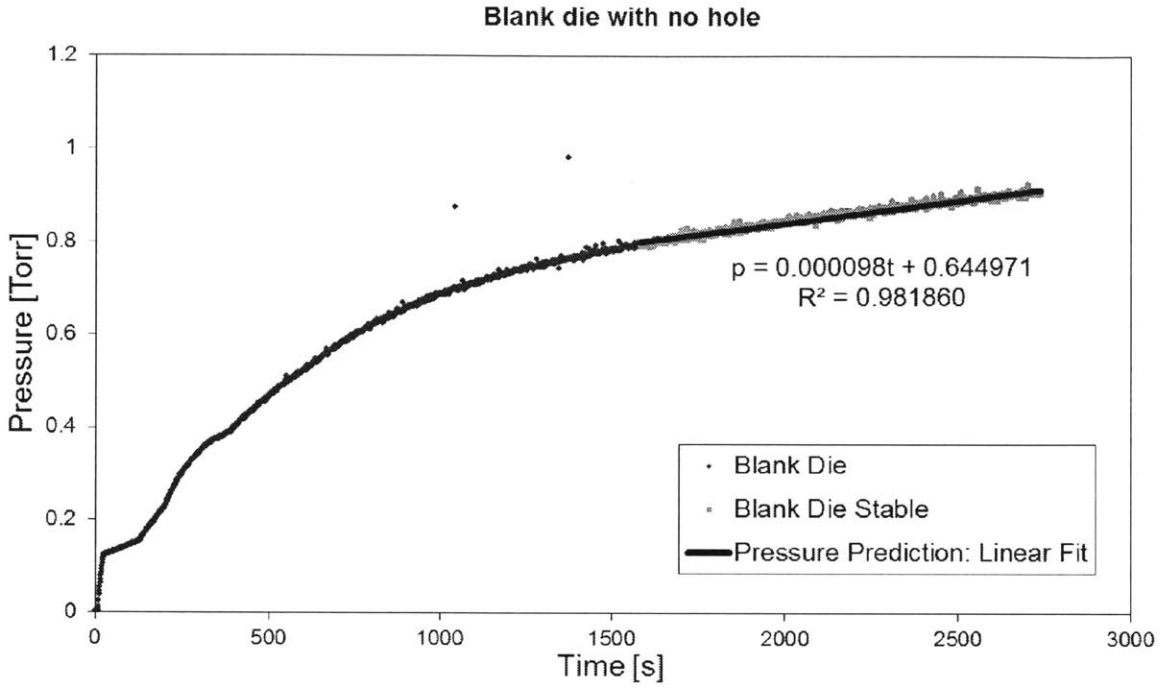

Figure 5-7 – Plot showing leakage around blank die

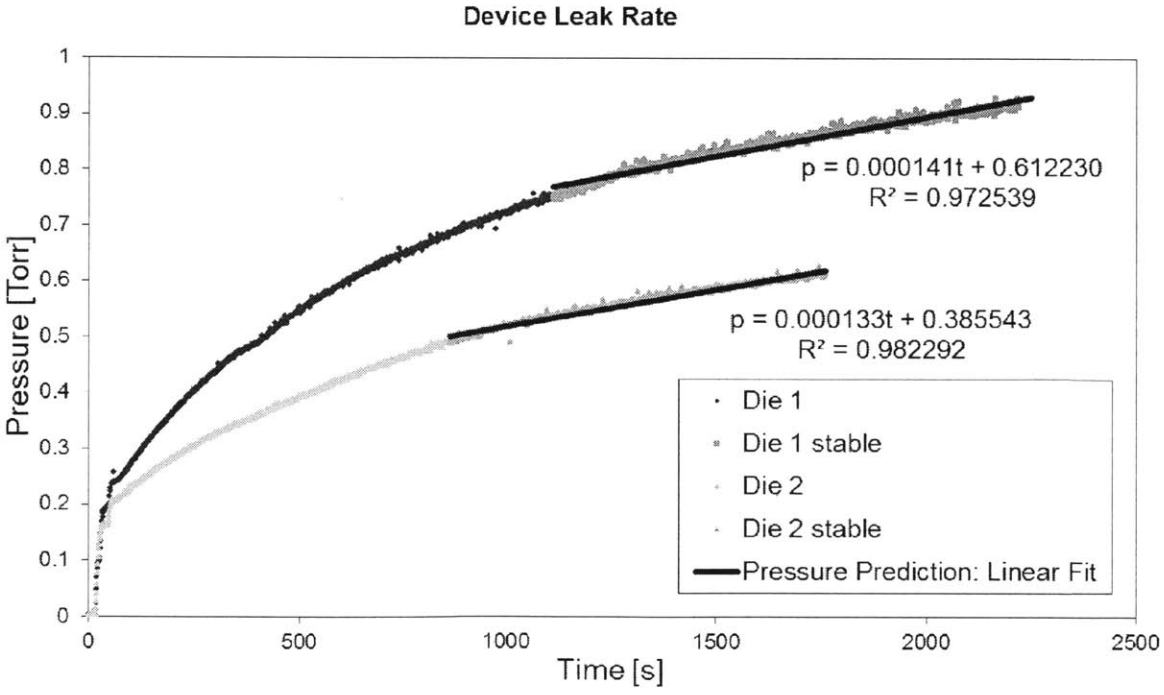

Figure 5-8 – Plot showing leakage through two test dies.

5.2.2 Electrical Testing

A general procedure for the electrical testing is described here. Problems with testing will be mentioned when they caused changes in the testing procedure, but a detailed analysis will wait until the next section.

The first testing method used the lock-in amplifier as both the source of the actuation voltage and the method for separating the third harmonic from the measured signal. The output current from the device was converted to a voltage and amplified by sending it through a 10MΩ resistor. The actuation voltage was 5V (rms), or an amplitude of 7.07 V. This is approximately half of the designed voltage (amplitude of 14 V). At this level of actuation, the beam displacement would be 1/4 of the designed displacement (0.082 μm), and the predicted output current would be 1/8 as large as predicted (3.4 nA). Though low, this current should have been measurable.

After an initial frequency sweep within 50 Hz from the expected resonance peak showed no results, a wider sweep was performed over a range from 10 kHz to 20 kHz. None of the devices showed any noticeable resonance peaks at any frequency.

Further examination of the circuit showed that the device had rectifying behavior. There was a small impedance when biased one direction, but very high impedance the other. This necessitated a biased actuation voltage for future tests. The frequency sweep procedure was repeated, but still no resonance peaks were visible. A typical frequency sweep with a DC offset is shown in Figure 5-9.

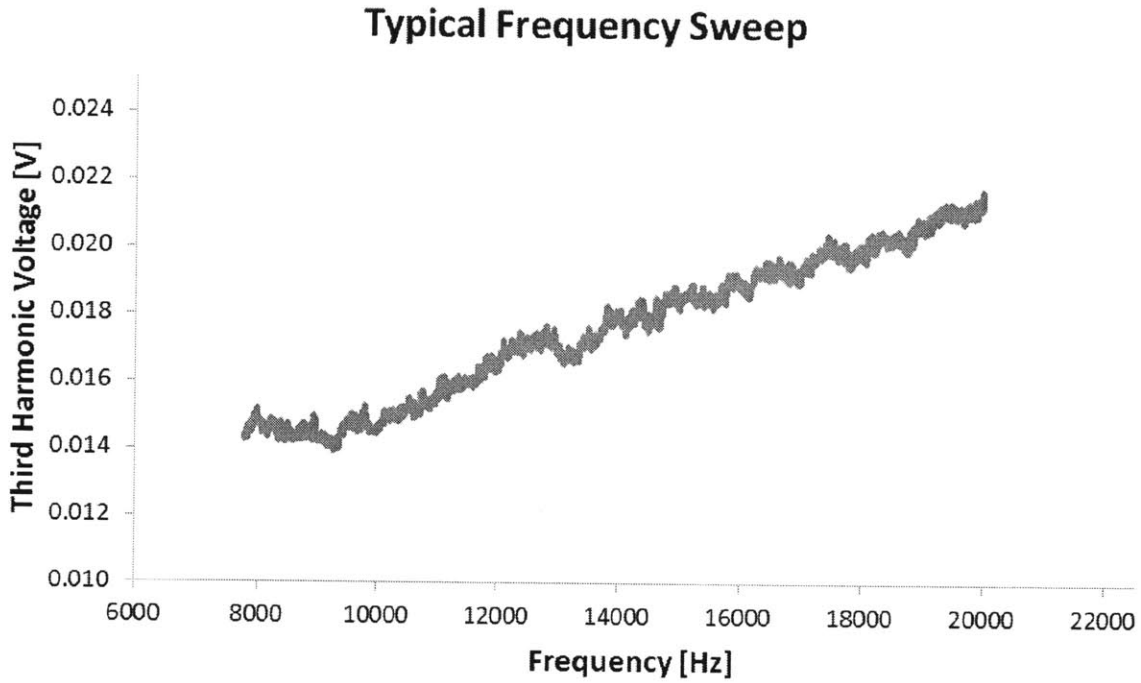

Figure 5-9 – Typical response before shorting was removed at the edges. Applied voltage was 5V rms, 20dB gain, 500kΩ measurement resistor.

Further examination revealed a noticeable lip at the edge of the devices. It appeared that the device layer had collapsed down due to over-etching in BOE, possibly shorting the device. To solve this, more devices were released with a shorter etch. The lip was still there, although the device layer was peeling up in many places in addition to the collapsed regions. By pressing the tape lightly to the peeling edge, the suspended silicon adhered to the tape and could be easily peeled away. The frequency sweep was repeated on devices that had been cleaned with tape. A marked decrease in the output current was observed, suggesting that there was a resistive short. However, there were still no resonance peaks. A typical frequency sweep after removing the collapsed edge is shown in Figure 5-10.

The increase in the measured third harmonic voltage at higher frequencies means that the impedance of the short decreases at higher frequency, suggesting that that the short is both resistive and capacitive in nature. This makes sense, because the collapsed region would not be in contact with the underlying device layer in all places, and where there is separation a capacitor is formed.

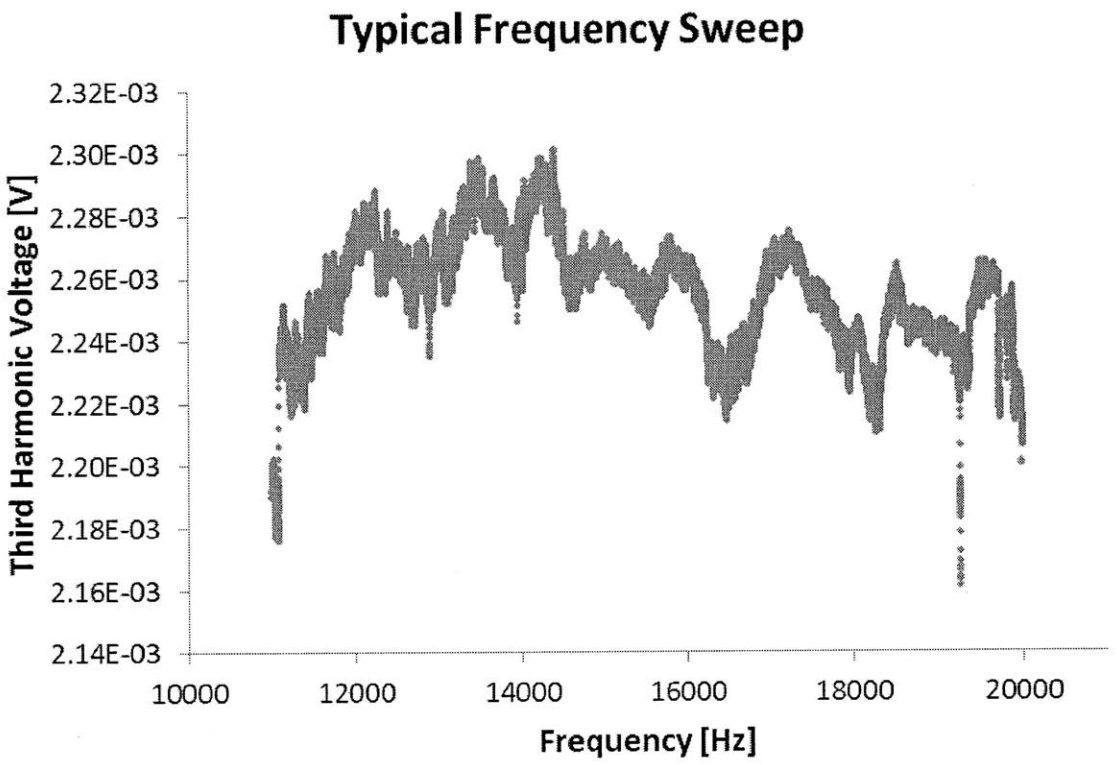

Figure 5-10 - A typical frequency sweep measurement from the lock-in after removing shorting with tape. Applied voltages were 2V-rms with a 3V DC offset, 500kΩ measurement resistor, 20dB gain. Measurements were taken for 10s at each frequency, with 5Hz per step. While there are several peaks, none of them are repeatable, nor are they large enough to constitute resonance.

Both of these measurements (before and after removing the edge shorts) are of the right order of magnitude.

Since a negligible amount of the voltage drop occurs across the cantilever, the entirety of the signal is due to the third harmonic signal in the applied voltage (discussed in more detail later in Section 5.3.4.1). A majority of the third harmonic voltage drop occurs across the measurement resistor. With 20dB gain, this should be on the order of 10-20mV.

The second measurement is a bit low. For the low actuation voltages used, the third harmonic due to the cantilever vibration should be around 0.3nA, which corresponds to a voltage across the measurement resistor of 0.15 mV. The ~1 mV third harmonic component to the actuation voltage is divided across the parasitic resistance and the measurement voltage. Along with the gain of 20dB, this should result in a 9.64mV measured voltage. This suggests that the parasitic impedance may be a bit higher than the estimates in section 5.3.3.

Since the phase of an oscillator changes 180° around resonance (with a sharper corner at higher Q), this presented another option for detecting resonance. However this also showed nothing noticeable around the expected resonance frequency.

5.3 Problems with Current Design

As discussed above, resonance was never successfully measured in the fabricated devices. The following sections will look at the underlying problems with the design in more detail.

5.3.1 Release Etch Undercut and Shorting

When frequency sweeps across the device failed to find a resonance peak, the voltage was measured across each of the circuit elements. This was done both at high frequencies (near the resonance frequency, ω_o) and at lower frequencies down to 1 Hz. It was found that even at very low frequencies, there was a voltage across the measurement resistor.

At 1Hz, very little current should be passing through a device consisting of predominantly capacitive plates. This suggests that there is a resistive short bridging the gap between the upper and bottom electrodes. A visual inspection with an optical microscope confirmed these suspicions as shown in Figure 5-11. A further check with an optical interference microscope confirmed that the collapsed region was flat and 2.5μm, the thickness of the gap oxide, lower than the adjacent device layer.

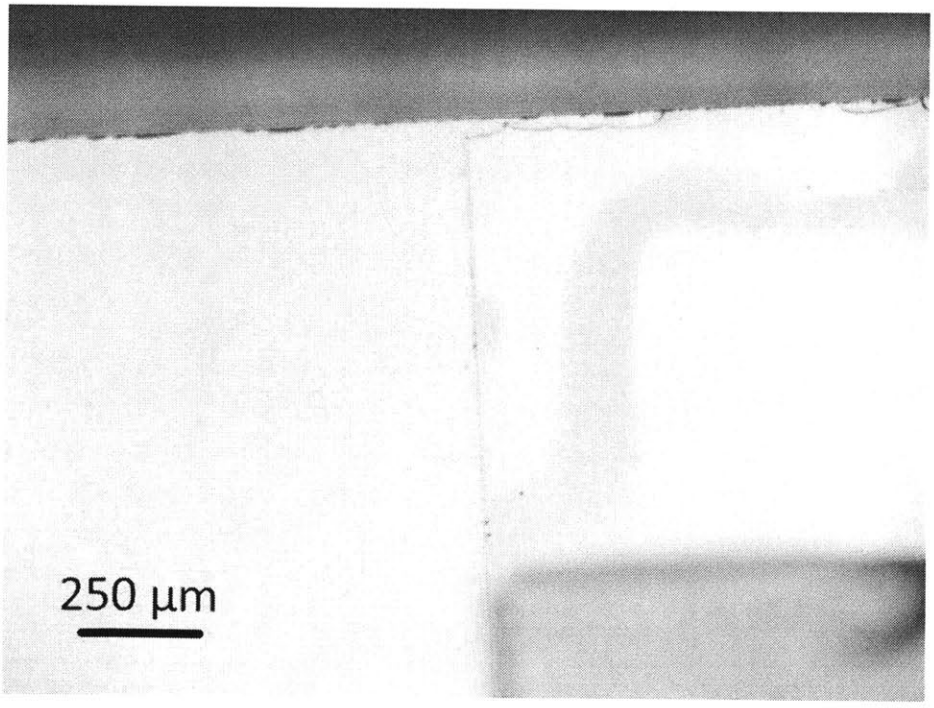

Figure 5-11 – Optical microscope picture showing top side of device. On the left side the lower wafer is exposed. In the bottom right the cap can be seen. The device layer (upper right) is visibly collapsed, creating a resistive short between the wafers.

The original etch was 45 min in BOE, which was intended to etch 100 μm in 40 min with an additional 5 min to ensure complete release. The collapsed region shows that the oxide was etched underneath the device layer for a distance of almost 250μm, which is considerably higher than the predicted 100μm. This suggested that a shorter etch might solve the problem because a shorter device layer overhang would be considerably stiffer and might not collapse. To test the effect of etch time, 15 more samples were released with etch times between 10 and 20 min.

Unfortunately, changing the etch time had no noticeable effect on the etch depth (see Figure 5-12). The undercut was to almost the same degree as before. In some cases, the thin device layer had peeled back far enough to show the underlying oxide. In many cases the device layer was peeling instead of simply sticking to the underlying substrate. On many dies, the device layer both peeled and collapsed down in different places. It is likely that the bond surface between oxide and silicon was not very strong, and HF was able to etch along the bond interface to a much greater depth than it would if the two surfaces were in perfect contact. This is further supported by the fact that the oxide was grown on the bottom surface, and in all cases where the oxide was exposed, it appears to have etched isotropically from the bond interface and remained attached to the bottom surface.

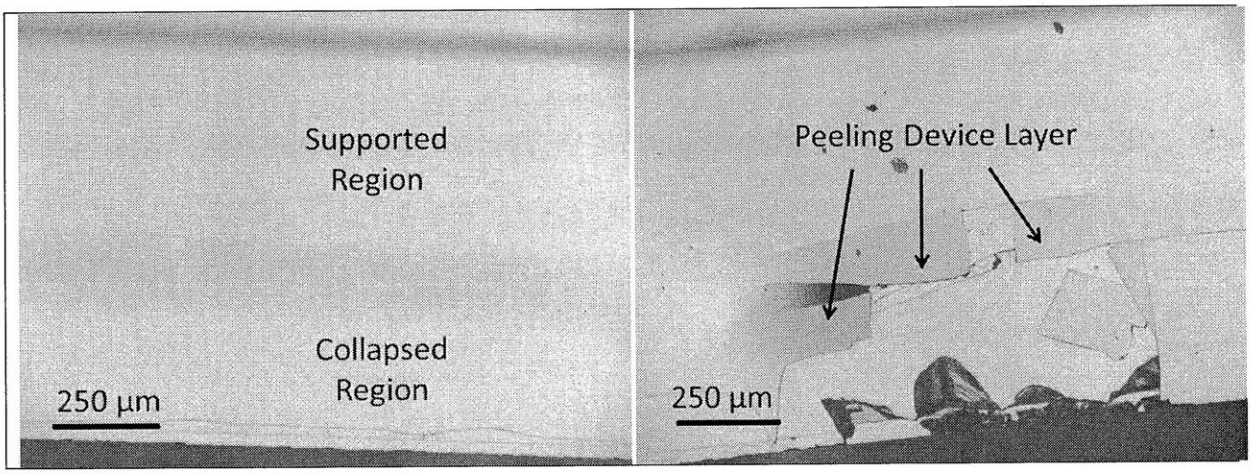

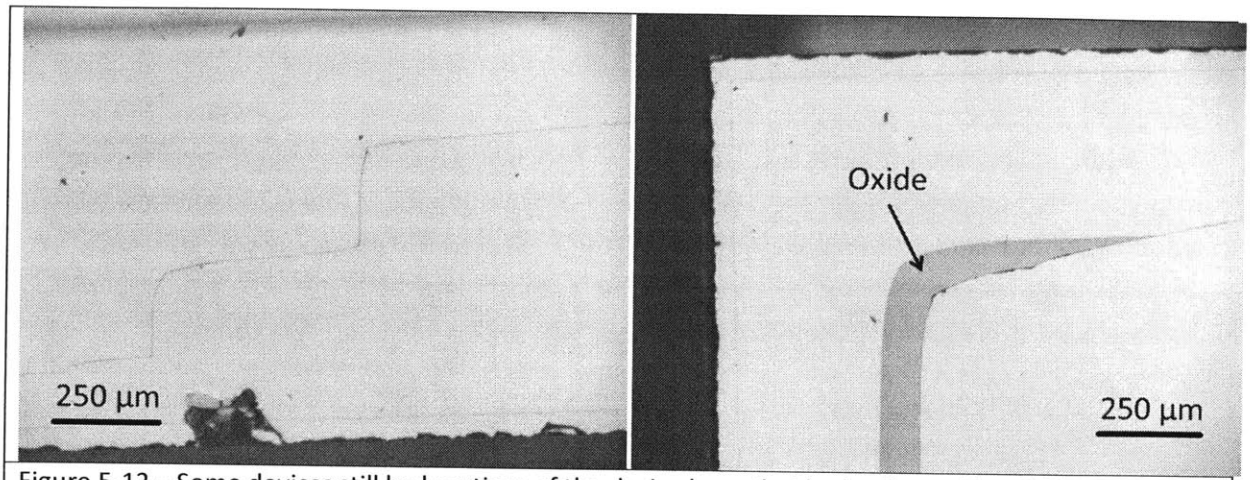

Figure 5-12 – Some devices still had portions of the device layer that had collapsed (top left). However, many more were peeling (top right). The peeling was not uniform (bottom left) and in some places had completely separated from the oxide (bottom right).

The peeling and revealed oxide suggested an idea – what if all of the suspended device layer silicon could be removed? This was done quite easily with lab tape. Lightly pressing the tape to the edges of the chips caused the device layer silicon to adhere to the tape, and it could easily be peeled away.

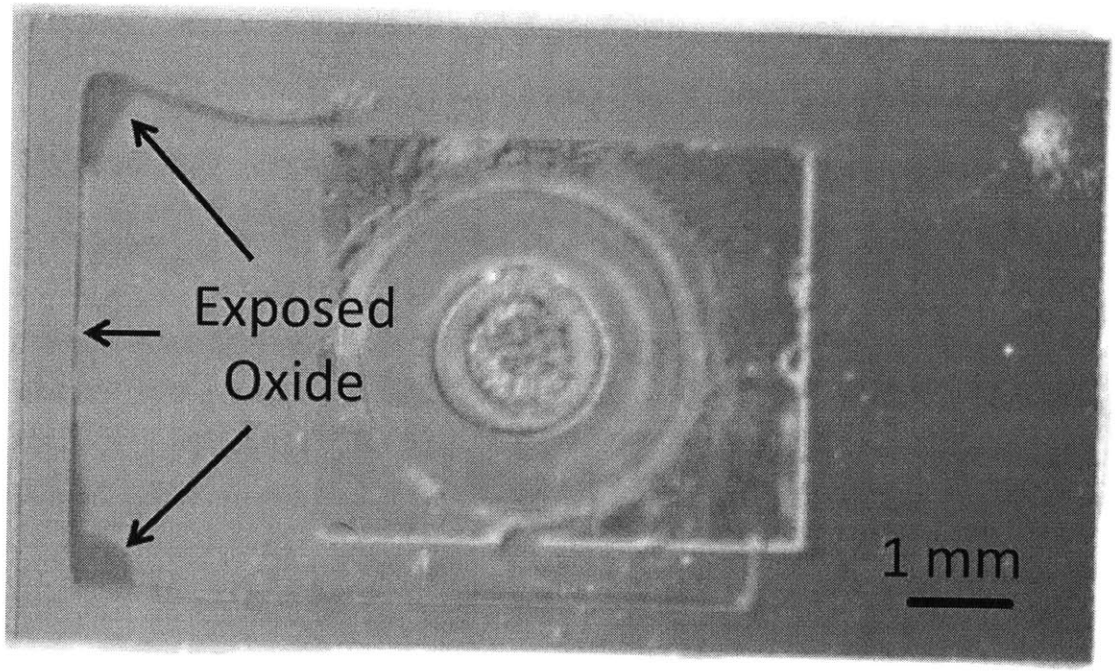

Figure 5-13 – After using tape to remove the overhanging silicon. The edge of the remaining device layer can be seen outlined by the exposed oxide (purple).

After peeling, a dramatic increase in impedance was seen (shown in Figure 5-9 and Figure 5-10 in previous section).

Two methods were used to ensure that the entire undercut region was removed. First, the edge of the still attached device layer was examined for large visible flakes, some as small as 10 μm, and peeled regions under a microscope. Obvious problems were targeted with tape. After obvious shorts were removed, the devices were subjected to a brief electrical test. Since the impedance change when the short is removed is quite dramatic at low frequencies, a large current (or voltage across the measurement resistor) indicated that the short was still there. At 1 Hz, the voltage measured across the measurement resistor was >100 mV with a short, and only noise was visible (corresponding to a voltage <1mV) when the short was removed.

The unexpectedly high etch rate of the oxide at the bond interface suggests poor adhesion between the two bonding surfaces. The poor bonding could be seen immediately after the wafers were bonded. A ring around the edge of the wafers remained separated, and several pockets showed rings in the interior. This is probably due to unclean wafer surfaces. Even though the wafers used for the final device were thoroughly cleaned before bonding, they had been sitting in wafer boxes for months before being bonded because they were remnants from earlier fabrication builds. Previous fabrication attempts resulted in broken or damaged wafers. The top wafers from one build and the bottom wafer from another build survived and processing resumed using the two salvaged wafers. Since the previous builds were abandoned a few steps before bonding, the wafers had been left in boxes for months with the bond surface exposed. They were cleaned before bonding, but it is unwise to expose the bonding surface longer than necessary, and the surface cleanliness was suspect.

5.3.2 Quality Factor

Another design limitation comes from the high frequency of operation. Higher frequencies yield higher output currents, and the end of the cantilever was perforated so that squeeze film damping would not limit the frequency of operation. The added signal from high frequency operation was never realized because the parasitic leakage paths also have lower impedance at higher frequency and swamp the third harmonic signal over the whole range.

An additional problem is that high frequency corresponds to high quality factor, especially at lower pressures. This leads to a very narrow and sharp resonance peak, and high Q peaks take more oscillations to reach resonance. Since the resonance peak does not shift as far at high Q, it was assumed that the frequency sweep range could be narrowed at lower pressures and resonance could still be measured. However if resonance can't even be found at high pressures, it would be very hard to find the sharper (and higher magnitude) peaks at lower pressures.

Resonance is determined by taking measurements across a range of frequencies near the theoretical resonance peak. Several measurements on the resonance peak are needed to

determine the peak height and width accurately. The width of the resonance peak is defined as the frequency range over which the oscillation magnitude satisfies $X_0 \geq \frac{X_{max}}{\sqrt{2}}$.

For resonance with low damping, the resonance width is

$$\Delta\Omega = \frac{\omega_0}{Q} \tag{5.1}$$

Taking the damping quality factor expressions from Chapter 2.1.5, resonance width can be written as:

$$\Delta\Omega_{viscous} = \frac{6\mu w + \frac{3}{2}\pi w^2\sqrt{2\mu\frac{M}{RT}\omega_o p}}{2\rho_b t w^2} \tag{5.2}$$

$$\Delta\Omega_{molecular} = \frac{4}{\rho_b t}\sqrt{\frac{2}{\pi}}\sqrt{\frac{M}{RT}}p \tag{5.3}$$

Peak width for the entire pressure range is plotted in Figure 5-14. For the device as originally designed, this translated into a resonance peak width of 100 Hz at atmospheric pressure. However, the width decreases dramatically as the pressure decreases. At the low pressure range around 10^{-2} Torr, the peak width would be 1Hz. This makes it quite likely that the frequency sweep is very slow, it would pass over the resonance frequency without a single measurement, much less the multiple measurements needed for accurate analysis.

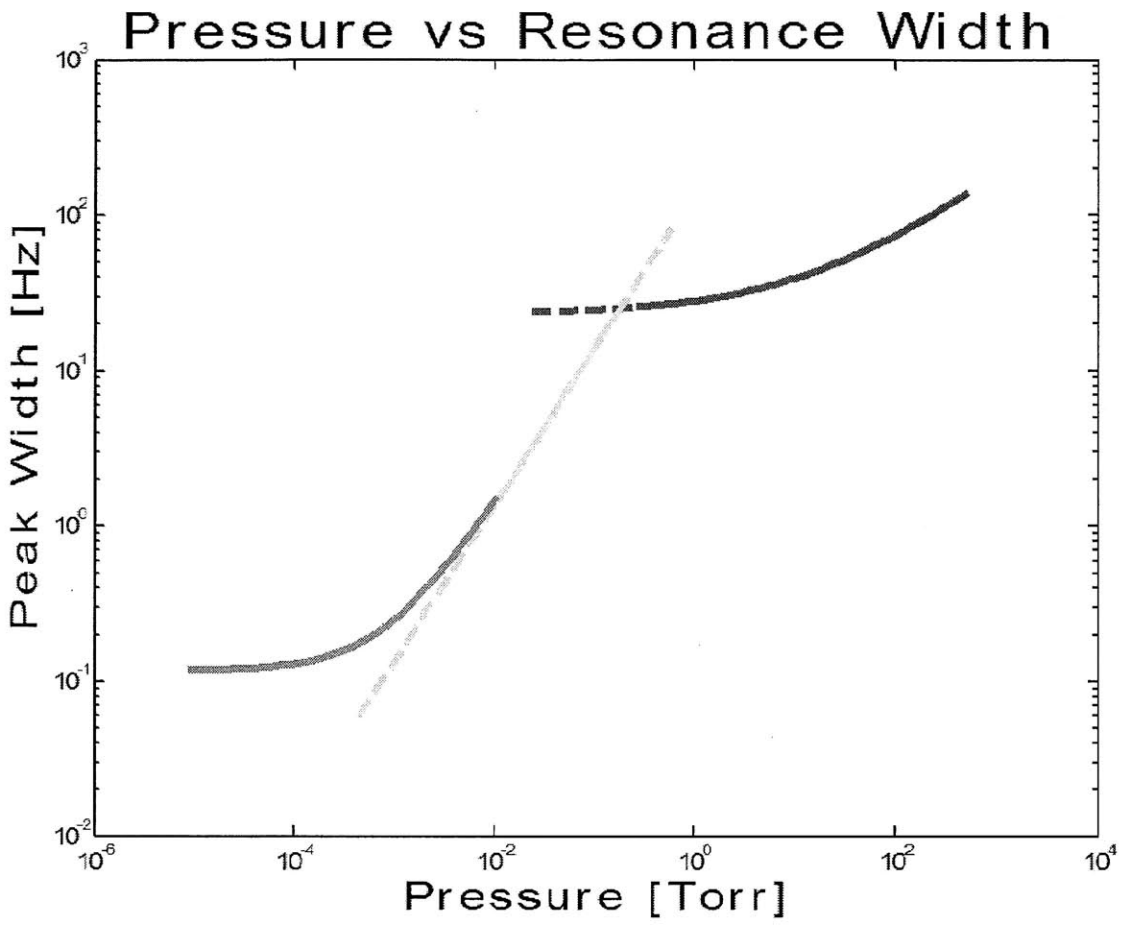

Figure 5-14 - Relationship between pressure and peak width

5.3.3 Parasitic Capacitance

It is not enough for the undoped silicon to have a high resistance compared to the doped actuation paths. Instead, the isolation between the terminals needs to be higher than the impedance of the actuation capacitor. This is discussed in the section below.

The third harmonic measurement method (described in Section 3.2.3.1) was chosen in part because with an ideal actuation voltage, the only current with a component at the third harmonic of the resonance frequency ($3\omega_0$) is directly proportional to the displacement of the cantilever beam. All other frequencies would be filtered out by the lock-in amplifier and ignored. However, if the actuation voltage contains a significant third harmonic component, then this can create an additional current at the output if the terminals are poorly isolated. A circuit model that incorporates the parasitic current paths is shown in Figure 5-15 below.

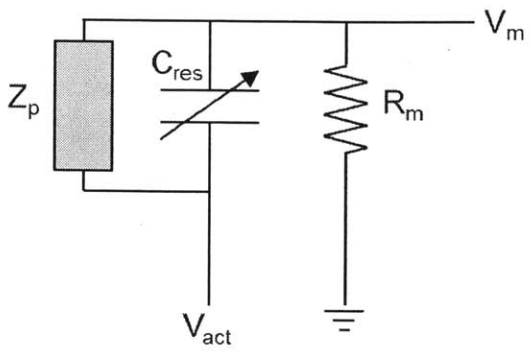

Figure 5-15 - An approximate circuit model for the actual device. The idealized case ignores Z_p because it was assumed that the only relevant path was the intended one. However, the high impedance of the capacitive actuation gap makes several parasitic paths contribute significant third harmonic components to the output signal.

In this case, the third harmonic component is small, measuring <2 mV when the actuation voltage is 5 V (rms). However, since the impedance of the parasitic leakage paths is much lower than expected, the third harmonic can easily flow through parasitic paths through the surrounding area of the chip rather than through the resonator.

Several parasitic paths will be considered in detail below. The critical concern is the impedance at the third harmonic frequency. To provide context and provide easier comparison between paths, impedance values are specifically calculated at 45kHz (the third harmonic frequency at theoretical resonance) for each path.

For the intended actuation path, the parameters are simple. Two doped silicon resistors R_1 and R_2 extend from the actuation capacitor C, as shown below in Figure 5-16.

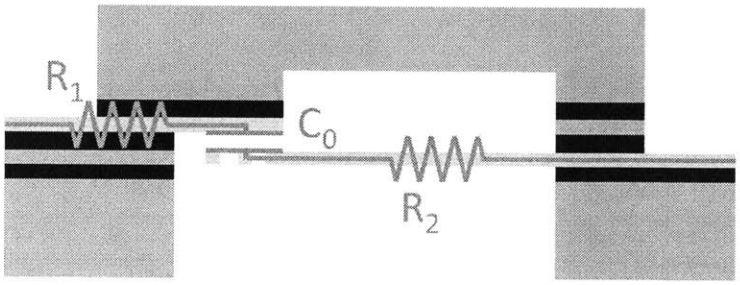

Variable	Value
R_1	52.9Ω
R_2	88.1Ω
C_0	171 fF
Z_C (@45kHz)	130MΩ
Z_{res} (@45kHz)	**130MΩ**

Figure 5-16 – Intended path for current, with circuit elements superimposed over device cartoon. The impedance of the actuation capacitor at the resonator tip dominates over the resistance of the doped leads.

One parasitic path involves current passing through the BOX layer into the device cap and over the top of the resonator, as shown in Figure 5-17 below. It can be shown that the active capacitance is due mostly to the area including and directly adjacent to the doped region. For a best case (least parasitic leakage) limit, the capacitor area was limited to the silicon directly over the doped region.

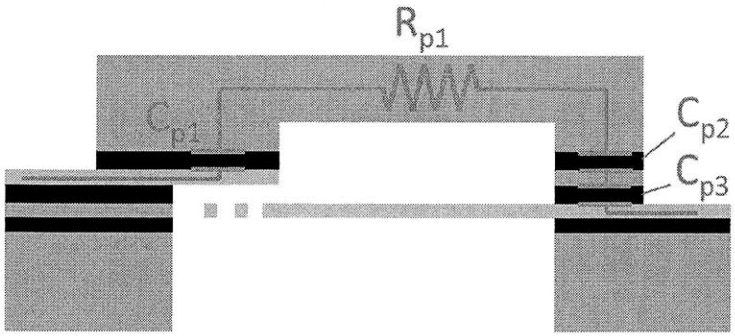

Variable	Value
R_{p1}	235Ω
C_{p1}	158.8pF
C_{p2}	138.1pF
C_{p3}	55.25pF
Z_{Cp1}(@45kHz)	140kΩ
Z_{Cp2}(@45kHz)	161kΩ
Z_{Cp3}(@45kHz)	402kΩ
Z_{over}(@45kHz)	**703MΩ**

Figure 5-17 – Parasitic path over the top of the resonator cap. It was assumed that the cap is approximately square, so the resistance is simply resistivity/thickness of the cap.

The next two leakage paths are similar and will be discussed together. The first occurs when current passes around the via hole and through the gap oxide. Another parasitic path also goes around the via, but passes through both oxide layers and travels through the bulk silicon around the via. Both of these are shown in Figure 5-18. The resistance through the bulk wafer has been neglected because the short path and thick wafer make it vanishingly small (on the order of 100Ω).

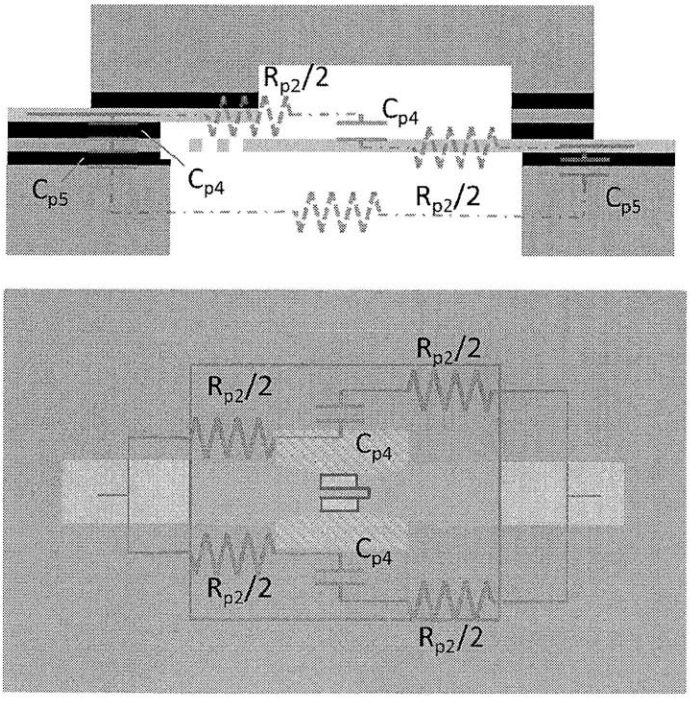

Around through device layer

Variable	Value
R_{p2}	60kΩ
C_{p4}	59.7pF
Z_{Cp4}(@45kHz)	372kΩ
Z_{around}(@45kHz) (each path)	**432kΩ**

Around through bulk silicon

C_{p5}	149pF
Z_{Cp5}(@45kHz) (each path)	149kΩ
Z_{under}(@15kHz)	**730kΩ**

Figure 5-18 – Top and side views of device showing a parasitic leak path around the cantilever through the bulk silicon. The green shaded region shows the estimated area for the capacitive path around the access hole.

All of these parasitic paths are in parallel with the intended path through the resonator, as shown in Figure 5-19 below. These can be combined to find the impedance of the parasitic paths that are adding to the output current.

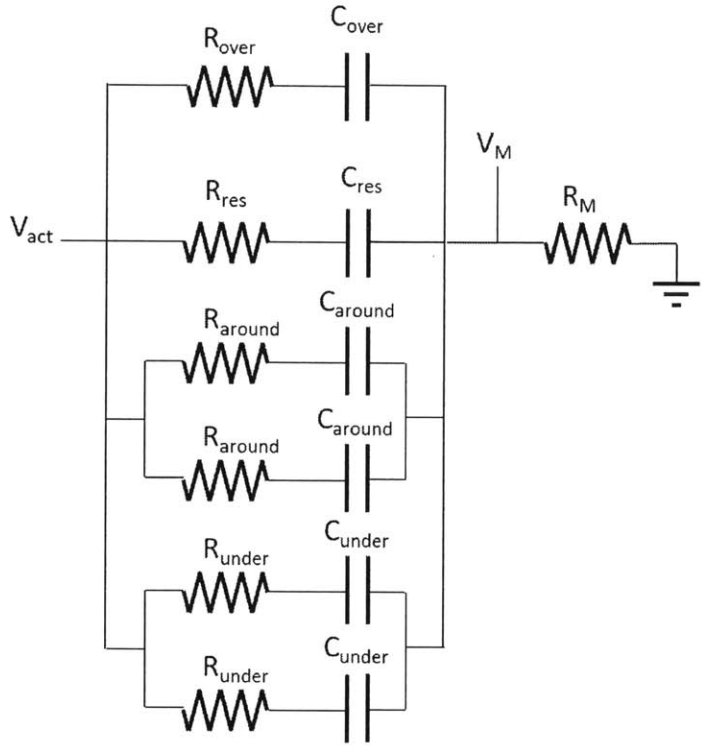

Figure 5-19 – Circuit model for "real" device. The R_{res}, C_{res} path is the intended path containing the resonator. All the others are parasitic impedances in parallel.

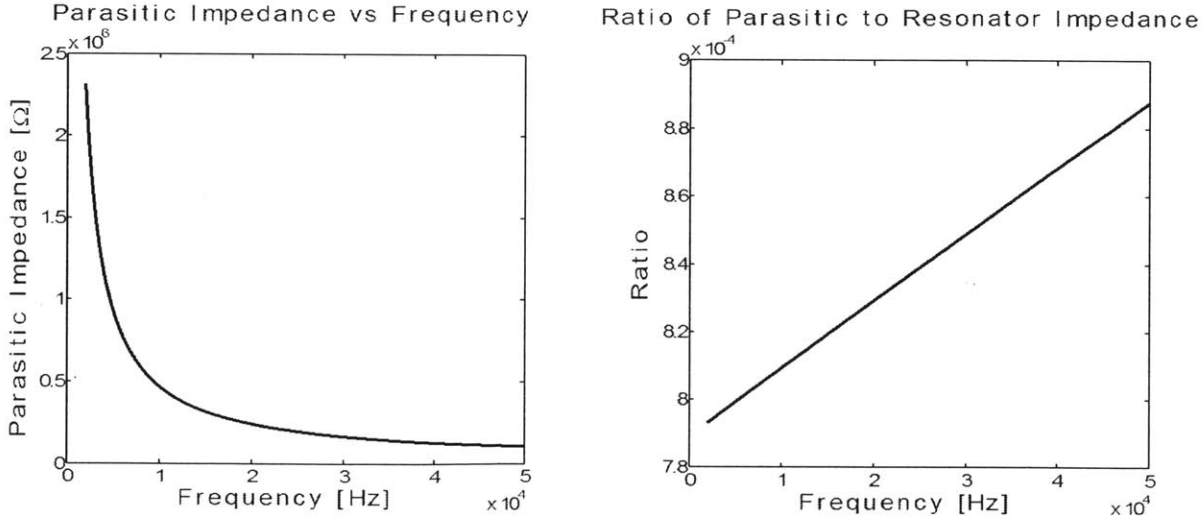

Figure 5-20 – Plots showing the relative impedance of the parasitic paths and the intended resonator path.

It must be noted that the capacitance of the bulk is stationary, and therefore will not modulate the frequency of the actuation voltage. Therefore, while the entire actuation signal will leak around the resonator, only the third harmonic component of the actuation voltage matters because the lock-in filters out everything else. The parasitic leakage only becomes a problem when the third harmonic in the actuation signal is large enough that it can pass around the parasitic paths and interfere with the third harmonic signal due to the cantilever motion. This will be analyzed further after the next issue, rectification, has been discussed.

5.3.4 Rectified Signal

It was originally assumed that the device would be an Ohmic element with a linear overall relationship between voltage and current with a slight third harmonic modulation due to the motion of the cantilever. However, a strange phenomenon was observed while plotting the voltage drop across the measurement resistor. The voltage applied to the whole circuit was sinusoidal, but the measured voltage appeared as a truncated sinusoid – it barely made it below 0V (see Figure 5-21). The same effect was observed in reverse for the voltage across the device, where the voltage was sinusoidal for negative values, but didn't cross above 0V.

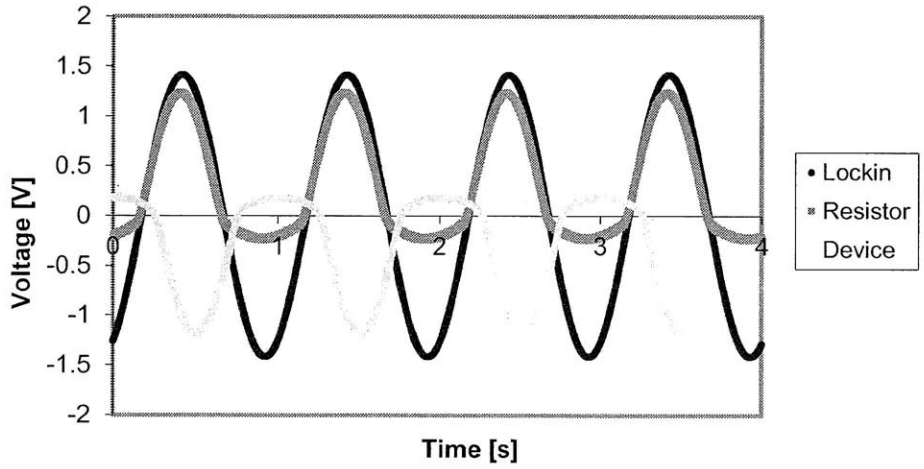

Figure 5-21 – Voltage across elements in testing circuit. The curves were measured separately (starting at different points in the waveform) and superposed on the same plot, so they don't line up. It can be seen that the maximum of the resistor voltage and device voltage add up to the applied voltage from the lock-in amplifier, so this strange behavior is still obeying Kirchhoff's laws.

Reversing the terminals (i.e. sending current the other way through the device) reversed the problem. The resistor showed negative voltages, the device only negative. It should be noted that summing the voltages around the entire circuit still gave the actuation voltage, so this irregularity does not appear to be an error in the measurement.

Some clarification came after adding a DC bias to the sinusoidal actuation voltage. When the bias was large enough that the entire signal was positive or negative, the voltage across both the device and measurement resistor had the expected sinusoidal forms. Additionally, the voltage across the device was markedly less for positive bias than negative. If we consider this as a simple voltage divider, the resistor is constant so this suggests that the device has much higher impedance under negative bias.

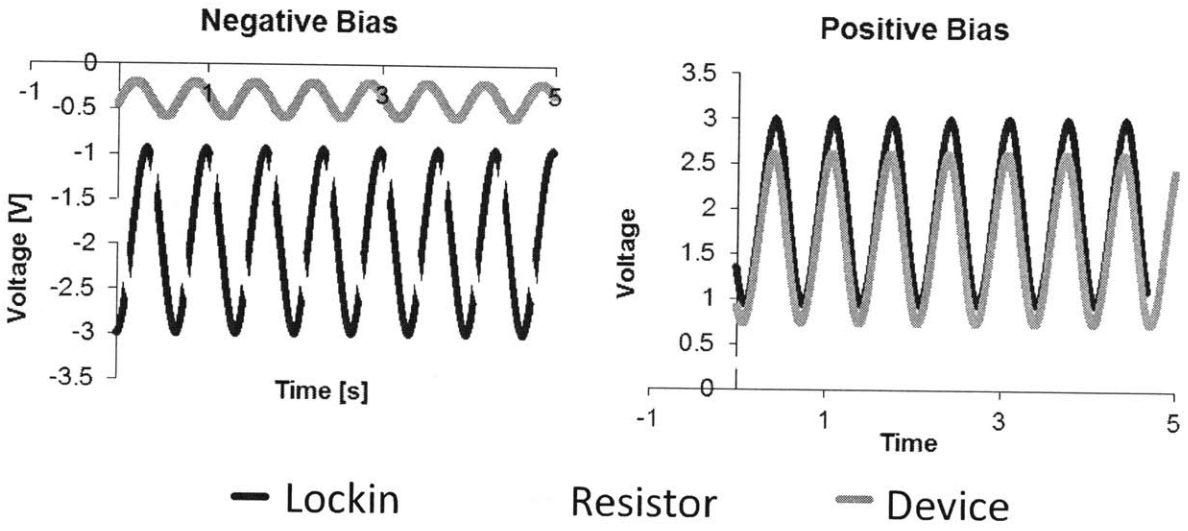

Figure 5-22 – Plots of voltage across the circuit elements under positive and negative bias.

This rectifying behavior resembled a diode – high impedance one way, low impedance when biased the other. Since the wafers started slightly p-doped and the implanted leads were very highly p-doped, there is no chance for a p-n junction to have created a diode. However, Schottky diodes are possible at the intersection of metal and silicon with dopant concentrations under $10^{17}/cm^3$. This likely occurred at one of the pogo pin – Si contact points (not both, or current wouldn't pass in either direction) because the actual annealing temperature was 1050°C, not 1100°C as it was in calculations.

The initial implantation profile, data provided by Innovion, can be seen in Figure 5-23.

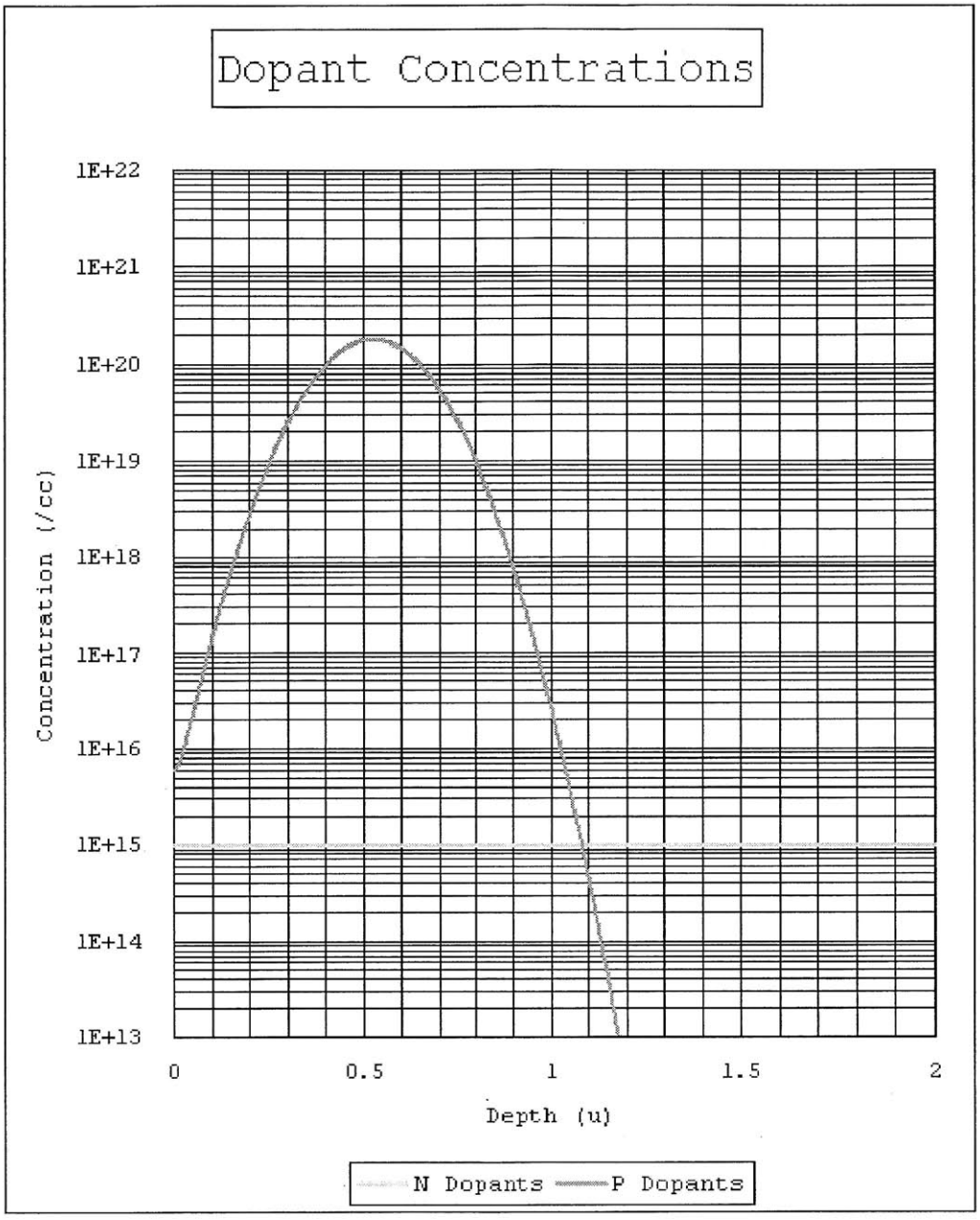

Figure 5-23 – Dopants implantation profile from Innovion. It should be noted that the substrate was actually P doped, so the green N dopants baseline should be P Dopants.

Doping profiles at the two temperatures are compared for several times in Figure 5-24. At 1100°C, 1.5 hours would have been sufficient to diffuse the dopants 5 µm deep through the device layer at a high enough concentration to prevent the Schottky barrier. However, 1050°C is the maximum allowable temperature in the annealing furnace, and unfortunately the same anneal time (1.5 hours) was used. As can be seen, the dopant concentration was well below the starting concentration in the device layer at 5 µm.

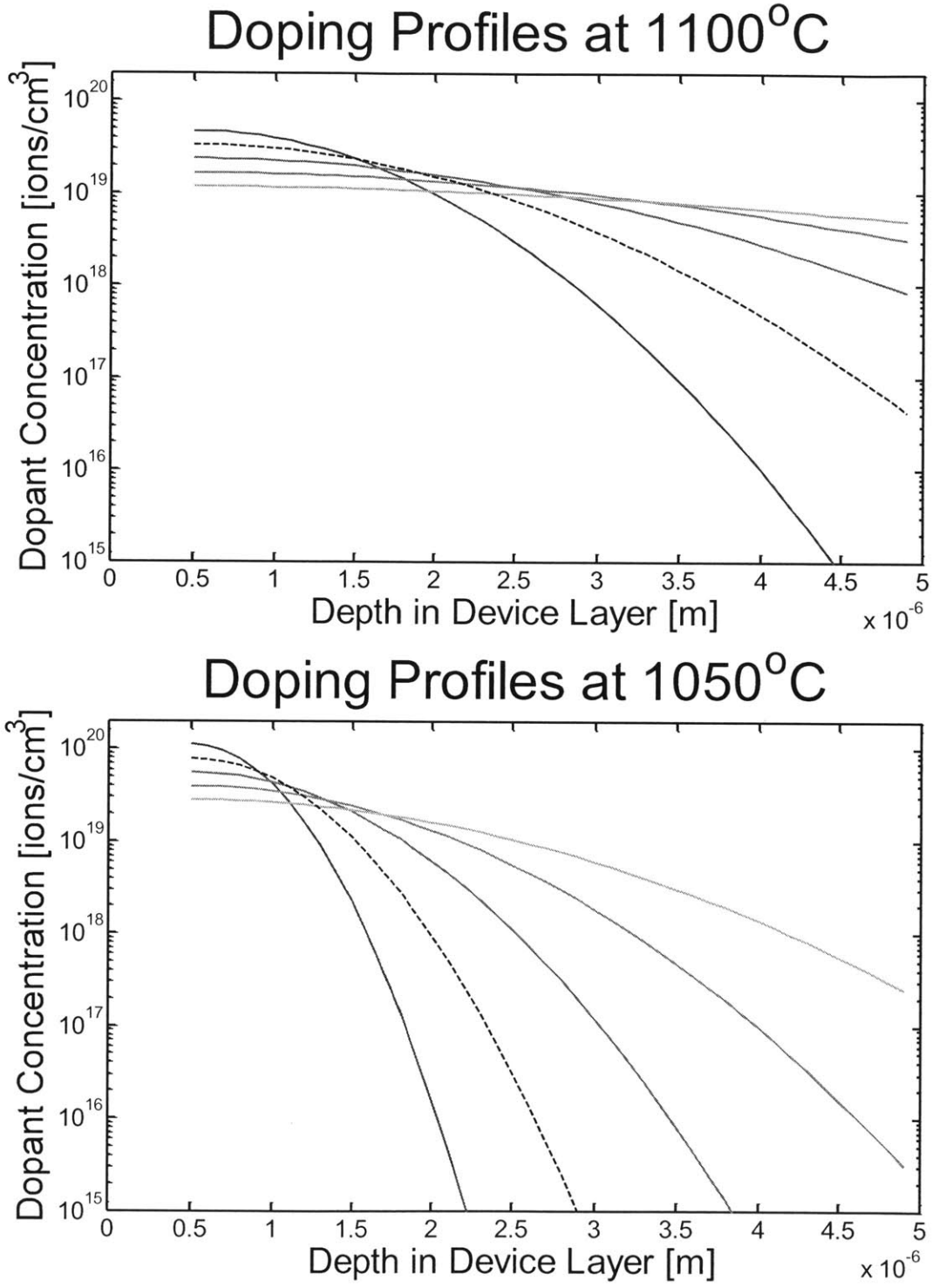

Figure 5-24 – Approximate doping profiles at 1050°C and 1100°C for several diffusion times: 1 hour (blue), 1.5 (actual time, black dashed line), 2hours (green), 4 hours (red), and 8 hours (teal).

Because the SOI wafers are bonded face to face, one of the device layers in contact with the pogo pins is face-up (implanted side up) and one is face down (the side previously touching the BOX layer facing up).

This is shown in Figure 5-25 below.

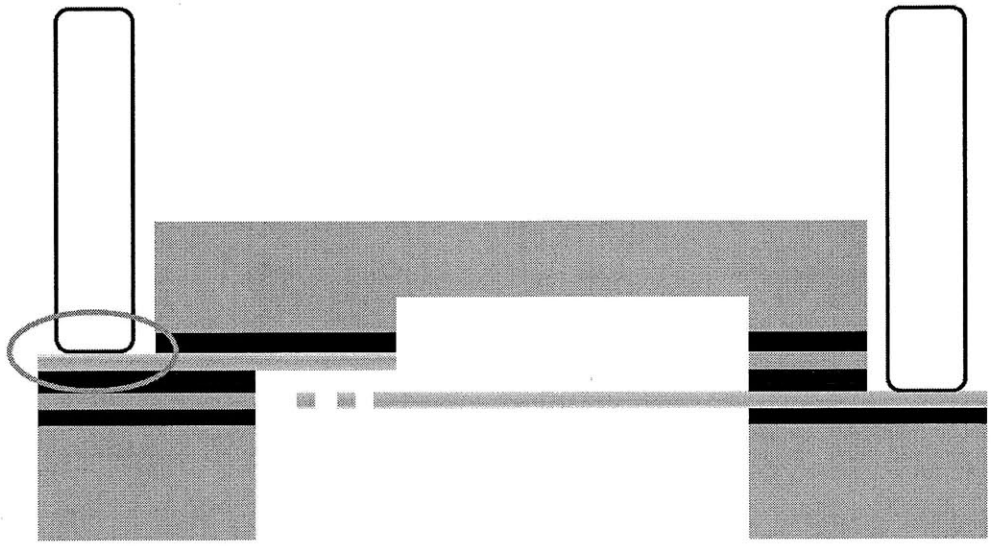

Figure 5-25 – Cartoon showing doping gradients. The bottom wafer was doped from the top, so the highly doped silicon is in contact with the pogo pin. The bottom wafer is upside down, so the highly doped region is on the bottom side.

5.3.4.1 ***Biased Measurements***

Since the device rectification prevents current flow in one direction, a simple solution is to bias the signal so that the applied voltage is always positive when testing the device. While this produces the expected actuation signal, it complicates the third harmonic sensing as described below.

Consider a more general actuation voltage:

$$V(t) = V_{AC}\sin(\Omega t) + V_{DC} \tag{5.4}$$

where V_{AC} is the magnitude of the AC voltage, V_{DC} is the magnitude of the DC voltage, and Ω is the actuation frequency. Since the force on the beam involves the voltage squared, the beam displacement has additional terms involving the DC bias. The amplitude of the beam can then be generally written (in expanded form) as

$$u(x,t) \propto u(x)\left(\frac{V_{AC}\sin(\Omega t)+V_{DC}}{(V_{AC}+V_{DC})}\right)^2$$
$$= u(x)\left[\frac{{V_{AC}}^2\sin(2\Omega t+\phi)+V_{AC}V_{DC}sin(\Omega t+\phi)+V_{DC}}{(V_{AC}+V_{DC})^2}\right] \quad (5.5)$$

where ϕ is the phase shift caused be damping and $u(x)$ is the mode shape of the actuated beam. This relation assumes that the displacement can still be broken up into a shape function $u(x)$ and a time dependence given by the sinusoidal response. For simplification in this analysis, it is assumed that the Ω and 2Ω terms have the same phase shift. Dividing by $(V_{AC}+V_{DC})^2$ normalizes the time dependence.

By approximating the end of the beam as parallel to the substrate (which is approximately true for small deflections) the capacitance of the charged beam and its time derivative can be written as

$$C(t) = \frac{\varepsilon_0 wl}{g - U_{max}\left[\frac{V_{AC}\sin(\Omega t)+V_{DC}}{V_{AC}+V_{DC}}\right]^2} \quad (5.6)$$

$$\frac{\partial C'}{\partial t} = \frac{2\Omega\varepsilon_0 wlu_{max}[(V_{AC}sin(\Omega t)+V_{DC})V_{AC}\cos(\Omega t)]}{\left(g - U_{max}\left[\frac{V_{AC}\sin(\Omega t)+V_{DC}}{V_{AC}+V_{DC}}\right]^2\right)^2 (V_{AC}+V_{DC})^2} \quad (5.7)$$

where U_{max} is the maximum deflection at the beam tip. Charge stored in a capacitor is given by

$$Q(t) = C(t)V(t) \quad (5.8)$$

Current is then

$$\begin{aligned} i(t) &= \frac{\partial Q}{\partial t} \\ &= \frac{\partial C}{\partial t}V(t) + \frac{\partial V}{\partial t}C(t) \\ &= \frac{\varepsilon_0 wl\Omega V_{AC}}{g - U_{max}\left[\frac{V_{AC}\sin(\Omega t)+V_{DC}}{V_{AC}+V_{DC}}\right]^2}\left(cos(\omega t) + \frac{2u_{max}[V_{AC}\sin(\Omega t)+V_{DC}]^2\cos(\Omega t)}{\left(g - U_{max}\left[\frac{V_{AC}\sin(\Omega t)+V_{DC}}{V_{AC}+V_{DC}}\right]^2\right)(V_{AC}+V_{DC})^2}\right) \end{aligned} \quad (5.9)$$

The first $\cos(\Omega t)$ term is the current that would pass through a normal fixed capacitor (without vibrations). For small vibrations, this term can be written as:

$$i_1(t) = \frac{\varepsilon_0 w l \Omega V_{AC}}{g - U_{max}\left[\frac{A\sin(\Omega t) + V_{DC}}{V_{AC} + V_{DC}}\right]^2}\cos(\Omega t) \approx V_{AC} C_0 \Omega \cos(\Omega t) \tag{5.10}$$

where C_0 is the un-actuated capacitance. The more complicated third order trigonometric term in the parentheses is a combination of first, second and third harmonic currents. The numerator can be separated as follows:

$$\begin{aligned}(V_{AC}\sin(\Omega t) + V_{DC})^2 \cos(\Omega t) \\ = \frac{{V_{AC}}^2}{4}[\cos(\Omega t) - \cos(3\Omega t)] + V_{AC}V_{DC}\sin(2\Omega t) \\ + {V_{DC}}^2\cos(\Omega t)\end{aligned} \tag{5.11}$$

Using the same small deflection approximation, the first, second and third harmonic currents due to cantilever motion can be written as follows (with the same small deflection approximation):

$$i_1'(t) = = 2C_0\left(\frac{V_{AC}\left(\frac{V_{AC}^2}{4} + V_{DC}^2\right)}{(V_{AC} + V_{DC})^2}\right)\Omega\frac{U_{max}}{g}\sin(\Omega t + \phi) \tag{5.12}$$

$$i_2(t) = = 2C_0\left(\frac{V_{AC}^2 V_{DC}}{(V_{AC} + V_{DC})^2}\right)\Omega\frac{U_{max}}{g}\sin(2\Omega t + \phi) \tag{5.13}$$

$$i_3(t) = = \frac{C_0}{2}\left(\frac{{V_{AC}}^3}{(V_{AC} + V_{DC})^2}\right)\Omega\frac{U_{max}}{g}\cos(3\Omega t + \phi) \tag{5.14}$$

This reduces to the original unbiased case where $V_{AC} = V_0$ and $V_{DC} = 0$, and with no deflection the only current is that of a constant capacitor (no second or third harmonics). Since the displacement is much less than the gap, the first harmonic current i_1' due to cantilever motion is much smaller than the normal capacitive current and can be ignored.

Both the second and third harmonic output currents depend on three variables: the total voltage ($V_{AC} + V_{DC}$), the magnitude of the AC voltage, and the frequency. If we limit the analysis to a fixed total voltage (choosing a value that is a factor of safety less than the pull-in voltage) we can reduce it to a two variable dependence.

In order to be able to measure the desired current from the resonator, the second or third harmonic currents due to the capacitor variation must be greater than the current due to the parasitic leak paths. To determine this, spectral measurements of the lock-in amplifier's

signal were made to measure the voltage at each harmonic over the relevant frequency range, as shown in Figure 5-26.

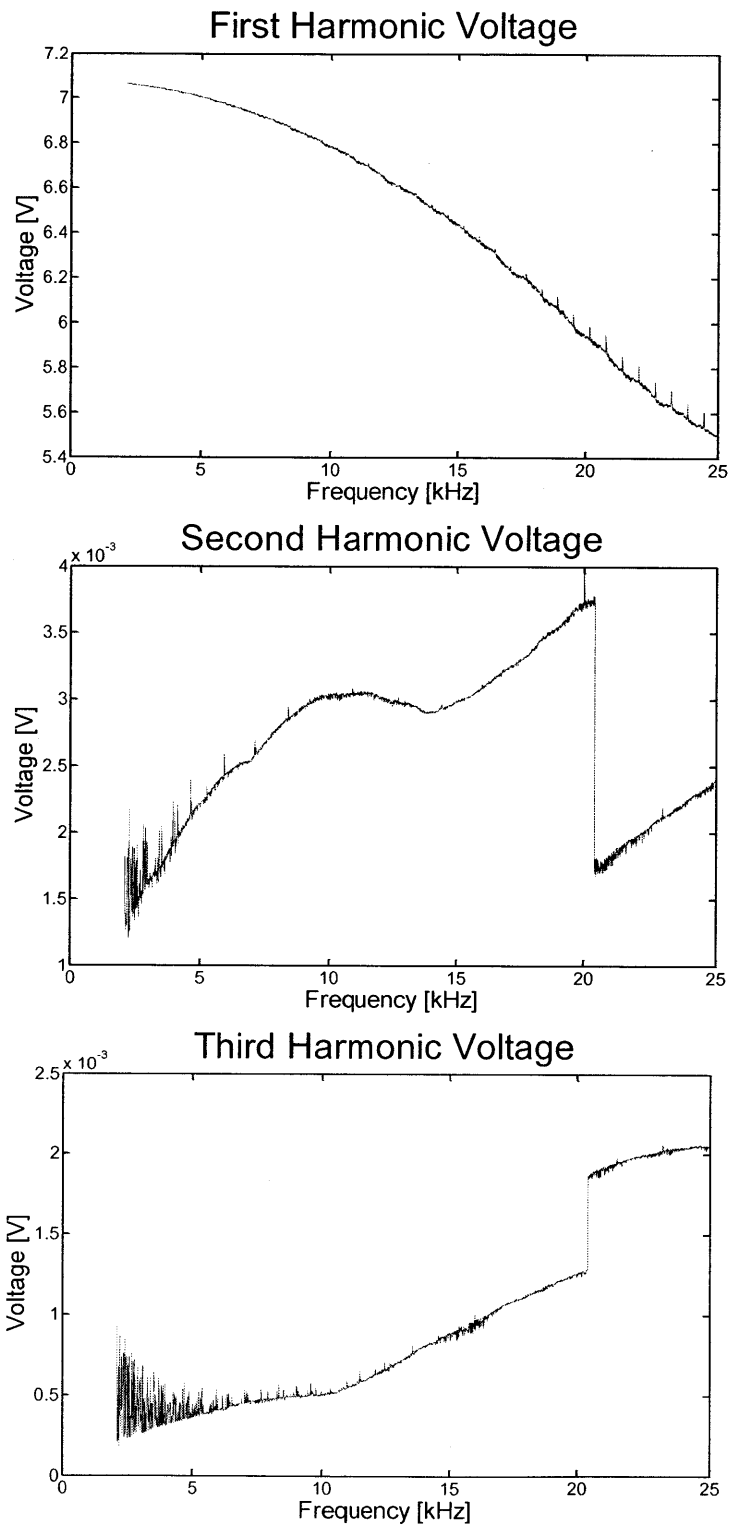

Figure 5-26– Comparison of the first three harmonics of the lock-in amplifier actuation voltage. The frequencies shown are always the first harmonic frequency, so the actual second harmonic frequency is twice that shown on the axis. There is a change in the way the signal is created at 20.4kHz that is visible by a drop in the second harmonic and a rise in the third.

The total second or third harmonic current though the parasitic leakage paths can be found at each frequency with Ohm's law. The second and third harmonic current due to the cantilever motion is a bit more complex because it still depends on both frequency and AC voltage. This could be analyzed multiple ways, but it can be seen from the equations for i_2 and i_3 that the amplitudes of each can be written as:

$$i_{2,3} = f_{2,3}(V_{AC})i_1 \tag{5.15}$$

where $f_{2,3}$is a scaling function that depends solely on the AC voltage:

$$f_3(V_{AC}) = \frac{i_3}{i_1} = \frac{{V_{AC}}^2}{2(V_{AC} + V_{DC})^2}\frac{U_{max}(V_{AC} + V_{DC})}{g} \tag{5.16}$$

$$f_2(V_{AC}) = \frac{i_2}{i_1} = \frac{2V_{AC}V_{DC}}{(V_{AC} + V_{DC})^2}\frac{U_{max}(V_{AC} + V_{DC})}{g} \tag{5.17}$$

For already fabricated devices, the only thing that changes here is the voltage. If we say that U_{max} is constrained by pull-in, then the displacement is now limited by the new maximum voltage, $V = V_{AC} + V_{DC}$. As discussed before in section 3.1.3.2, the maximum beam displacement is bounded by two simpler static beam bending expressions. Concentrating the entire electrostatic force in a point load at the tip forms an upper bound, while distributing the force over the entire beam forms a lower bound.

With the scaling function, the best case (lowest) parasitic current due to second and third harmonics in the actuation signal can be directly compared to the predicted best case (highest) second and third resonator currents. The scaling function is shown in Figure 5-27 and the currents are plotted in Figure 5-28 below.

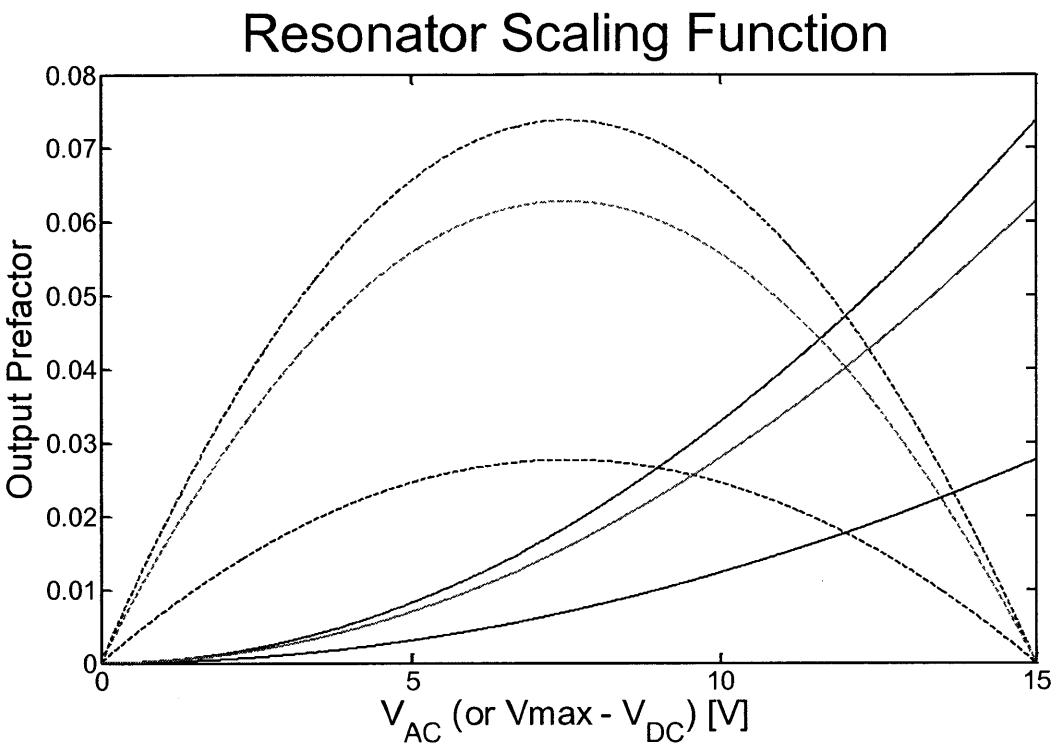

Figure 5-27 – The scaling function is shown here for a total voltage of 15V (almost pull-in). Dotted lines corresponds to the second harmonic, solid lines are the third harmonic. The black lines are the lower bounds where displacement was determined with a distributed actuation force along the entire beam. The blue lines are the upper bound where the entire actuation force on the capacitor is concentrated at the tip of the beam. The red lines in the middle show the actual situation where the beam is actuated over length l at the tip.

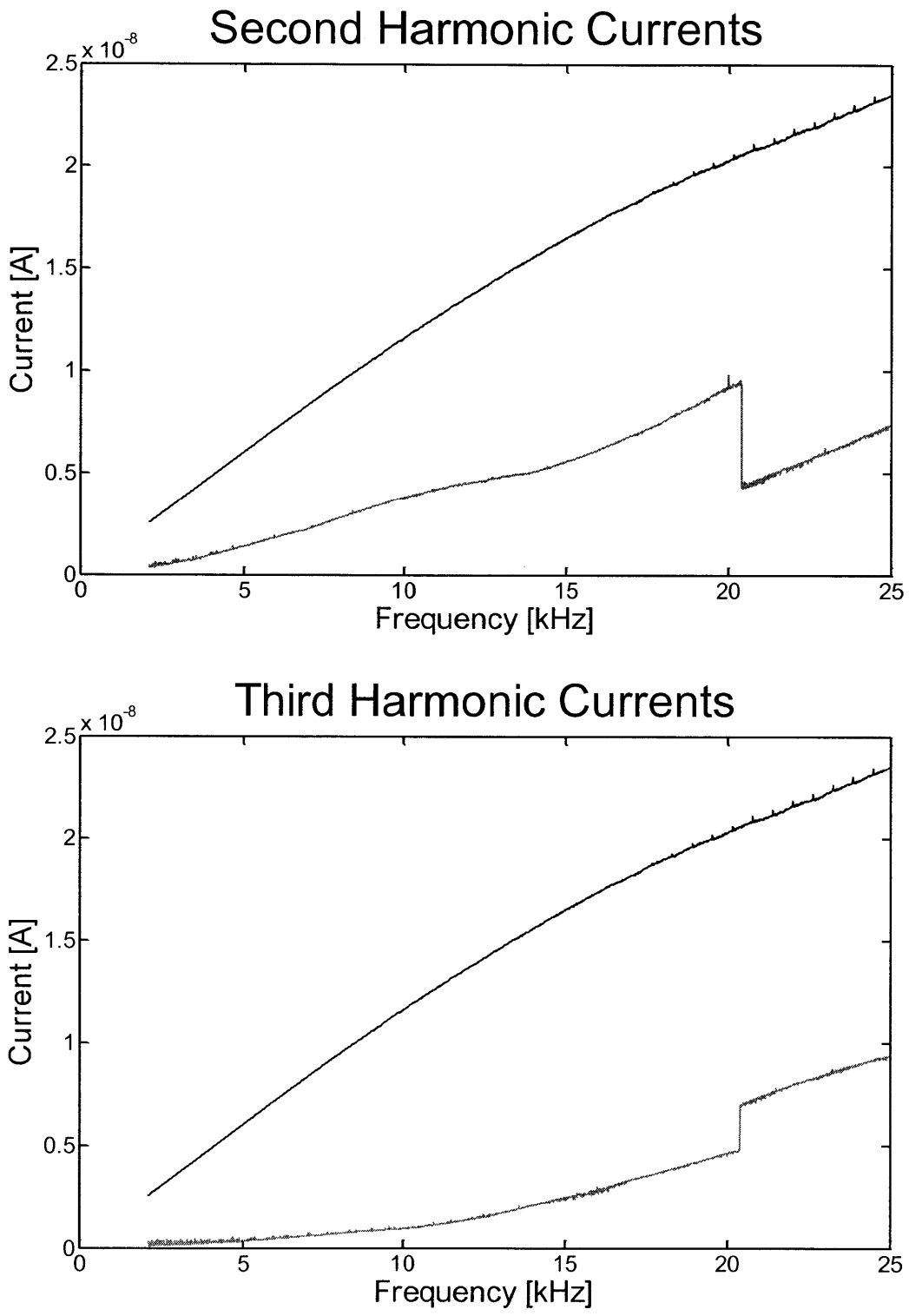

Figure 5-28 – Parasitic currents (shown in red) compared with the first harmonic current (black) through the resonator.

To find the actual second and third harmonic currents, the first harmonic must be multiplied by the prefactor shown in Figure 5-27 above. Diode effects limit $V_{AC} \leq 7.5V$, and it can be seen that this value produces the highest prefactors in the allowable range. For these values, the actual second and third harmonic currents with a V_{AC} =7.5V are shown in Figure 5-29 below.

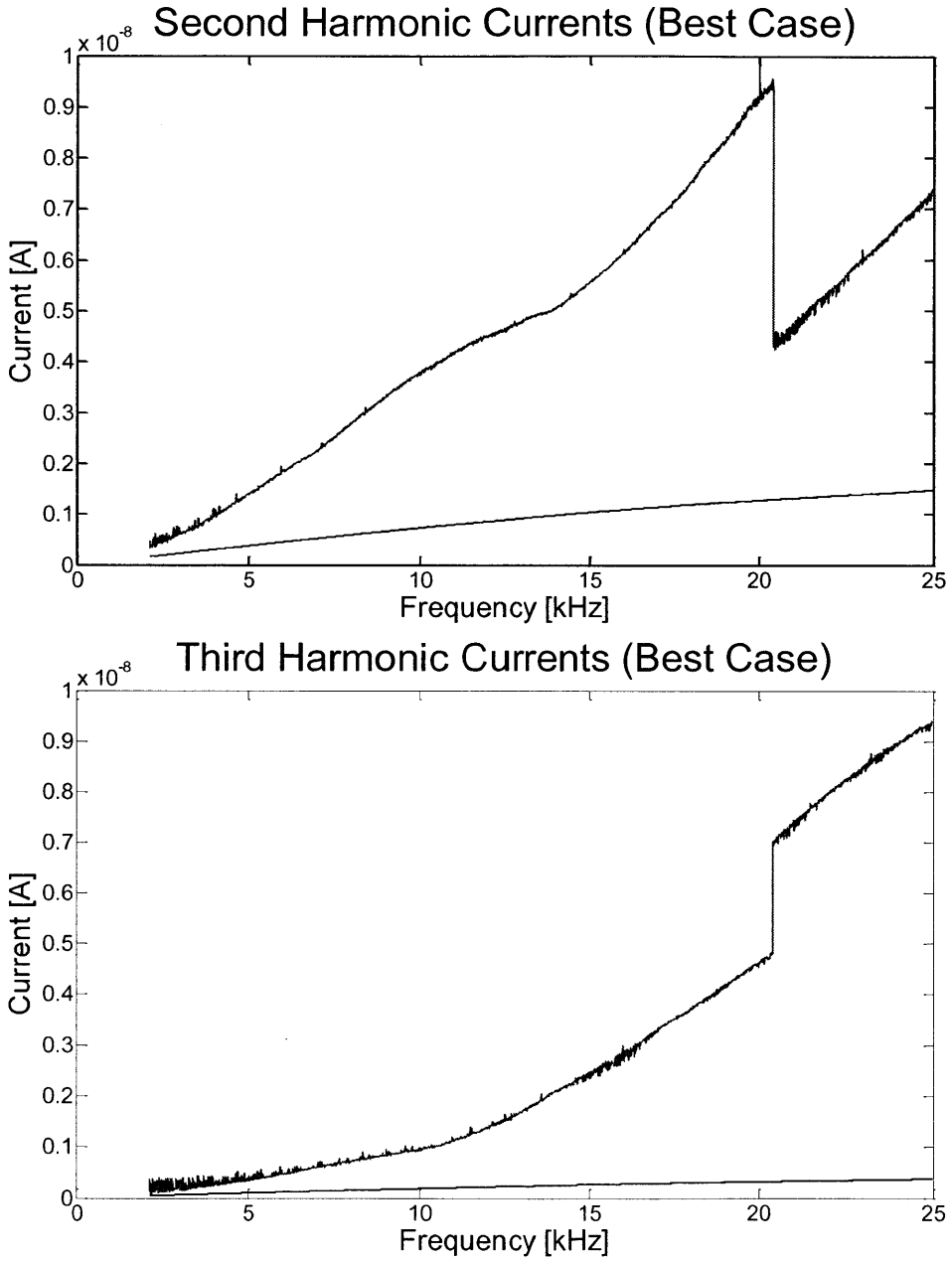

Figure 5-29 - Actual second and third harmonic current (shown in black) compared to the corresponding parasitic current (blue) for V_{AC} = 7.5V.

It can be seen that over most of the frequency range, the magnitude of desired third harmonic signals is at least an order of magnitude less than the parasitic current from the lockin amplifier. The second harmonic comes closer to being measurable, but still falls well short. Without rectification, the full AC range would be available, increasing the prefactor for the third harmonic from ~0.1 to ~0.7. However, even increasing the third harmonic output by seven times does not make it measurable. The leakage through the parasitic capacitance paths is still greater.

A cursory review of other lock-ins shows that several claim to have filters that may be able to remove this from the output.

5.3.5 Summary of Device Flaws

There were several design flaws that prevented this device from producing a measurable signal. Several problems were solved (at least to a degree). The etch undercut produced shorting until it was peeled back with tape.

Since the resonance peaks at lower pressures have much higher Q, they are very narrow and take a long time to reach the maximum displacement. Since small variations in fabrication and the release etch can cause variations in the resonance frequency, resonance must first be found at higher pressures where the peaks are broader before there is any chance that that the resonance peaks can be found at lower pressures.

Even though the unexpected rectification was partially solved by biasing the signal, it greatly reduced the output third harmonic. The fatal flaw was the parasitic current from the lock-in amplifier signal that swamped the desired second and third harmonics to such a degree that patching the other holes in the design couldn't save the device.

6 Future Work

The previous section details several design flaws that prevented the current design from producing a measurable third harmonic signal showing resonance. This section describes several improvements that can be made to the design and fabrication process that should fix these flaws. An improved bonding procedure will alleviate the peeling at the device edges by preventing deep undercuts during the release etch. Isolation between the two electrodes has been greatly increased with a few mask changes and an isolation trench. The cantilever dimensions will be altered to ensure a lower resonance frequency and quality factor. Finally metal will be added to the contact pads to remove the Schottky barrier and rectification effect.

6.1 Improved Bonding

Improving the quality of the bond is paramount to improving the quality of the final devices for several reasons, beyond the obvious observation that fewer devices would reside in unbonded regions.

First, it is likely that the peeling and shorting at the edge of each device could be avoided. As discussed before, the unexpectedly high etch rate of the oxide at the bond interface suggests poor adhesion between the two bonding surfaces. While it was possible to solve the shorting problem on a device by device basis with tape, this was far from an ideal solution. Additionally, if the device layer at the edge is intact, then it is unlikely that the device layer supporting the base of the cantilever will be undercut as well.

Second, better bonding will improve the thermal contact between the wafers. This will lead to better cooling during the final DRIE etches, extending the life of the protective resist while etching and increasing device yield.

Third, and perhaps most importantly, better bonding can allow for smaller wafer caps. As originally designed, the caps extend 2mm beyond the edge of the access via to ensure that the interface was hermetic. This is a big problem because that large cap area creates a large parasitic capacitance. A high quality bond should provide a similarly leak-free seal with a much smaller contact area. Decreasing the contact area to a 0.5mm ring around the via should yield marked improvements in isolation between the two electrical terminals.

6.1.1 How to improve bonding

In order to improve the quality of the fusion bond, two areas need to be addressed: surface preparation and bonding conditions.

The cleanest bond surfaces are those that have had a film protecting them right until the bonding process starts. This partially explains why the wafers used in the final devices, which had been sitting around (albeit in clean boxes) for months before bonding did not have great

adhesion. However there are some changes to the original process that can help provide additional adhesion.

The original 100nm thermal oxide on the top wafer does not need to be removed, and the subsequent PECVD oxide growth and anneal can be taken out as well (remove step 3 in Figure 4-16). 100nm is thick enough to provide a hard mask as part of the nested mask process (steps 4-8 in Figure 4-16) that creates the resonator cavity. In this way, the bonding silicon of the top wafer is not exposed to any chemicals or the air until moments before bonding.

The bottom wafer cannot be kept entirely free from chemicals before bonding because CMP and the required wafer clean are necessary to create a PECVD oxide surface smooth enough to bond. However, the subsequent photolithography step need not be done on the bonding surface. A thin layer of silicon nitride should be grown on the oxide surface and can be used as a hard mask for the dry etch that defines the cantilever. This silicon nitride will protect the oxide until the bonding step when it can be removed with hot phosphoric acid.

Cleaner wafers will improve adhesion, but another significant factor in bond quality is the conditions under which the bond is performed. The wafers were pressed under vacuum for 30 minutes for initial adhesion and then annealed at 850°C for 3 hours. A better bond can be formed by increasing all of three of these parameters. Increasing the press time raises the contact area between the wafers. Increasing the temperature and time gives the oxide at the interface enough time to diffuse and form a high quality bond with the silicon. A suggested protocol would include a 1 hour initial press, followed by an anneal at 1000°C overnight (approximately 12 hours).

6.2 Metal Contacts

One of the initial problems diagnosed with the devices was rectification of the actuation voltage. Biasing the actuation voltage solved the rectification problem but created its own problems. The AC component was limited to half of its previous magnitude to prevent pull-in, which decreased the output signal drastically.

A simple fix would be to add a thin metal film to the contact pads, along with a short anneal to prevent the same Schottky barrier. This can be done by adding a few steps between DRIE etching the caps (step 3 in Figure 4-25) and dicing the wafers (step 4 in Figure 4-25).

1) Use a dry anisotropic oxide etch to remove the oxide from the top side to expose electrodes.
2) Create a shadow mask, basically a full wafer stencil, for the electrodes. The shadow mask wafer is patterned with thick resist, exposing the area directly above the electrodes, and etched completely through using a DRIE etch.

3) Align the shadow mask to the wafer stack, and use photoresist to glue it down.
4) Evaporate a thin film of platinum (as an adhesion layer) followed by gold through a shadow mask.
5) Remove the shadow mask in acetone.
6) Rapid thermal anneal to remove Schottky barrier.

6.3 Better isolation

One of the largest problems with the current design is that it allows large portions of silicon adjacent to the device electrodes to act as capacitive pathways for current. This issue will be solved using two approaches that both lower the capacitance of the neighboring pathways. First, the overall area will be decreased by changing the device geometry. Second, the resonant frequency of the beam will be lowered, further increasing the impedance of the parasitic paths. Since the resonance frequency depends on many on several design parameters and affects the overall operation of the device, it will be discussed in more detail in Section 6.4.

6.3.1 Decrease the area of parasitic capacitors

A few slight changes to the masks can drastically decrease the parasitic current.

- Improved bonding allows the cap size to be decreased from a 2mm ring surrounding the via to a 0.5mm ring. This decreases the length for the path through the cap from 2mm to 0.5mm. This also allows the contact pads to be moved closer, decreasing the area of the doped leads and possible leakage through the substrate.
- Since the resistance in the doped leads is insignificant compared to the impedance from the resonator, the width of the doped region can be reduced from 1mm to 0.2mm without adding much to the resistance of the intended path. This decreases the width for the parasitic losses through the cap from 1mm to 0.2mm
- Etching a trench through the device layers around the exposed electrodes and cap isolates the electrodes and cap from the surrounding silicon. This can easily be added into the current process with two changes.
  1) Etch a trench through the device later of the bottom wafer at the same time as the cantilever and holes in steps 4-5 in Figure 4-9.
  2) Etch a trench in the top wafer during the second nested mask etch (patterned in step 4, etched in step 8 of Figure 4-16).

  It is tempting to extend the trench under the cap, but this would compromise the hermetic seal. Trenching decreases the area available for the capacitors in the paths around the via and through the bulk.

- The trenches mean that the overall size of the chip has no impact on the parasitic current. Leaving it the same size ensures easy handling with tweezers and enables the same test apparatus to be used (with a new acrylic cap to move the pogo pins).

These changes are shown in Figure 6-1.

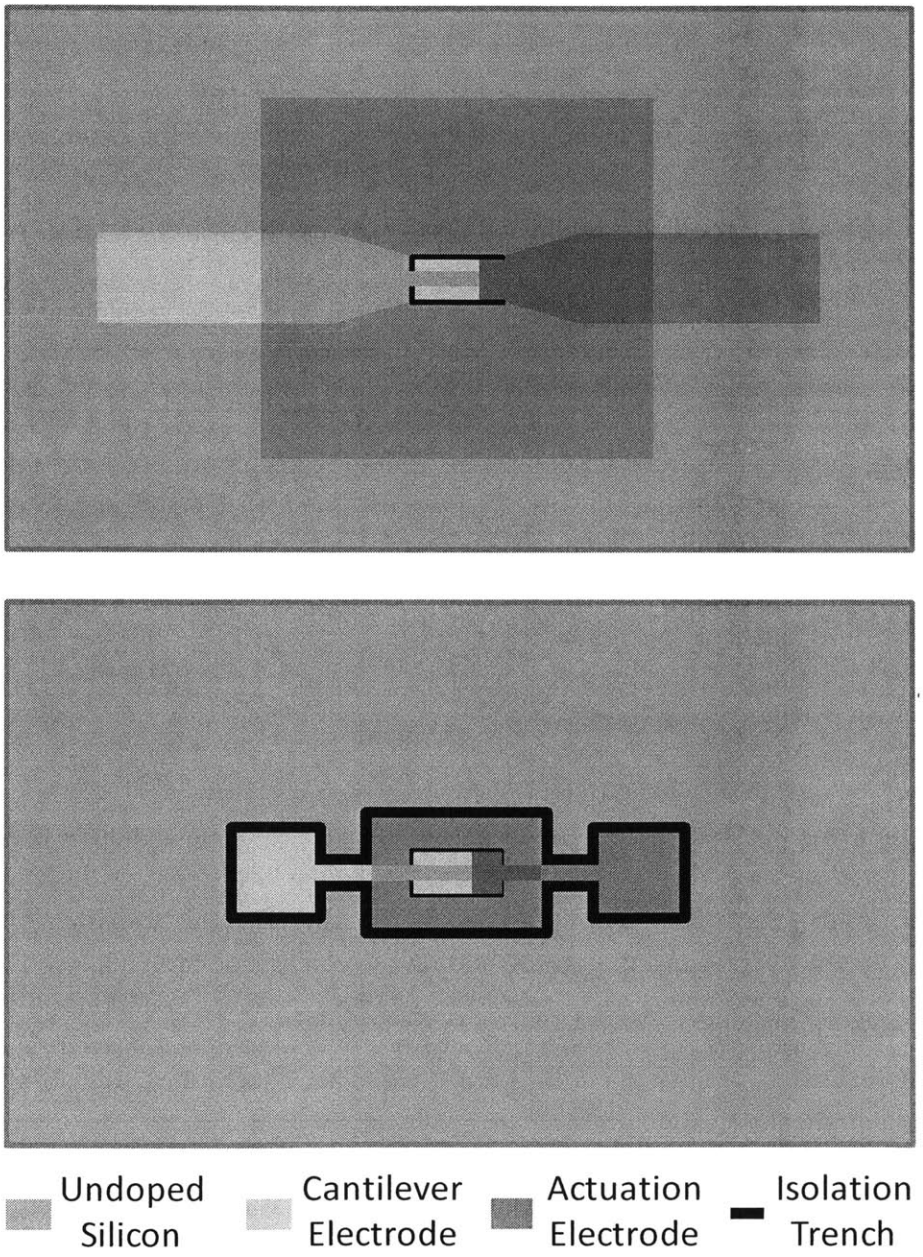

Figure 6-1 - The old design is shown on the top with a 2mm cap ring and 1mm wide electrodes. The suggested design with improved isolation is shown below with a 0.5mm cap ring, 0.2mm electrodes, and an isolation trench through both device layers surrounding electrodes and cap.

These isolation changes drastically cut down on the parasitic current. If no other changes were made, the isolation would increase the equivalent impedance at the third harmonic of resonance (45kHz) by more than an six times, from 114kΩ to 687kΩ. The changes are summarized in Table 6-1 below.

Table 6-1 – Summary of Isolation Changes

Resistance Path	Old Value	New Value
Over the top	703kΩ	26.5MΩ
Around the side (x2)	432MΩ	2.21MΩ
Around the side through bulk (x2)	730MΩ	3.92MΩ
Equivalent Parasitic Impedance	**114kΩ**	**687kΩ**
Intended Path	130MΩ	130MΩ

This effect can be further amplified if necessary by choosing more resistive substrates. The current devices were built with a starting resistivity of order 10Ω-cm, but wafers with device layer resistivity as high as 100 or even 1000Ω-cm are readily available. A 1000Ω-cm device layer would bring the around the side impedance to a very respectable 8.14MΩ (each side), and the overall parasitic impedance to 2.06MΩ.

While the parasitic and intended third harmonic currents are dependent on the actuation voltage and the precise device dimensions, an estimate of the relative magnitudes can be made at this point. If the same device dimensions and actuation voltage are used, the isolation improvements are made, and the contacts are metallized, then the parasitic current drops by 6x and the third harmonic current increases by 7x (because the full 14V can be AC, rather than DC biased). Instead of a 3 nA parasitic signal with a 0.3 nA target signal, there is a 0.5 nA parasitic signal with a 2.1 nA target signal.

This shows that improved isolation should make the signal visible, but one further change, lowering the resonance frequency, should allow for amplification of the small signal. Additionally, lower actuation voltages are required by the low frequency design. The third harmonic in the actuation voltage is decreased proportional to the actuation voltage, so the parasitic current will be considerably lower than the above estimate.

6.4 Lower resonance frequency

The resonance frequency f of the final devices has a theoretical value of ~15kHz depending on the device, and quite a high quality factor (just under 1000 at 1atm, much larger as pressure decreased). This ended up being more of a liability than a benefit. It is almost impossible to amplify a small signal at these frequencies. Additionally, the high quality factor translates into a very sharp resonance peak, which necessitated long frequency sweeps in an attempt to even find resonance. Lowering the frequency will allow amplification of the signals, while lowering the quality factor could broaden the resonance peaks.

As described before, frequency for the first mode of oscillation can be defined as:

$$\omega_0 = 2\pi k_1^2 \sqrt{\frac{E}{12\rho}}\left(\frac{t}{L^2}\right) \tag{6.1}$$

Spring softening has been ignored for this calculation. Since softening causes lower frequencies, this simplification provides a conservative overestimate for the frequency.

If we target a particular cutoff frequency (ω_{max}), then this provides a relationship between the thickness (t) and length (L) of the cantilever. Let ω_{max} = 10^4 rad/s, a reasonable radial frequency that allows for amplification with commercial preamplifiers. The other required relation is that the beam must not pull in, or (with a factor of safety of 2):

$$U_{max} = \frac{\varepsilon_0 w l V^2}{2g^3}\frac{1}{k} \leq \frac{g_0}{6} \tag{6.2}$$

where k is the stiffness of the beam. As discussed before, a simple expression that overestimates the deflection assumes the entire force is applied as a point load at the tip. Therefore:

$$k = \frac{3EI}{L^3} \tag{6.3}$$

The moment of inertia is linear in width, as is the actuation force, so width cancels and has no effect on the actuation frequency or displacement. However, the output current depends on the capacitance of the actuation area, so larger width leads to larger signal. Width will again be fixed at $L/5$, to ensure the motion behaves as a beam rather than a plate.

One critical change from the earlier analysis is realizing that allowing the actuation length (l) to vary adds a crucial control over the actuation force without affecting the resonance frequency. Let $l = \gamma L$, so that once a ratio is set, varying one affects the other. The pull-in constraint can be solved for γ:

$$\gamma \leq \frac{g^3 E t^3}{12\varepsilon_0 V^2 L^4} \tag{6.4}$$

The parameters t and L are no longer independent once the frequency has been set. Substituting that into the above relationship:

$$\gamma \leq \frac{g^3 t}{\varepsilon_0 V^2}\rho\left(\frac{\omega_{max}}{2\pi k_1^2}\right)^2 \tag{6.5}$$

A larger gap is extremely beneficial because it allows larger voltages and displacements before pull-in, so the gap will be at the maximum value allowed in fabrication, 2.5μm. This leaves only a few independent variables remain: V, t, and γ. This is plotted in Figure 6-2 for voltages between 1 and 5V (rms).

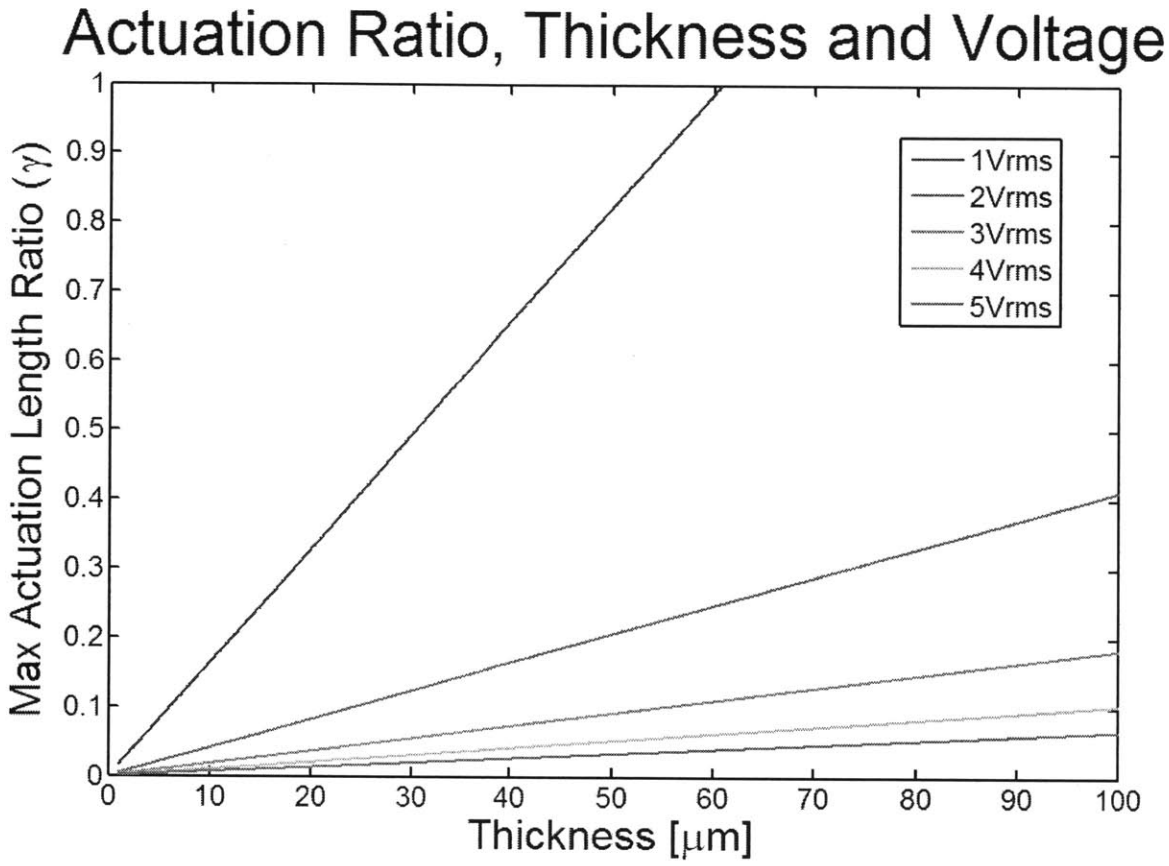

Figure 6-2 – Relationship between actuation length and thickness for select voltages between 1 and 5V (rms)

For three values of γ, the thickness, length, and resulting third harmonic current are given in Table 6-2.

Table 6-2 – Thickness and output current for several length ratios. The proposed design is highlighted with a thicker box.

Length ratio (γ) / Voltage (rms) [V]		0.2	0.1	0.05
1	Thickness [μm]	12.2	6.10	3.00
	Length [μm]	3160	2230	1570
	Third Harm Current [nA]	2.81	0.756	0.200
2	Thickness [μm]	48.6	24.3	12.2
	Length [μm]	6310	4460	3160
	Third Harm Current [nA]	22.5	6.00	1.59
3	Thickness [μm]	109	54.7	27.3
	Length [μm]	9460	6690	4730
	Third Harm Current [nA]	76.3	20.6	5.37
4	Thickness [μm]	194	97.2	48.6
	Length [μm]	12620	8920	6310
	Third Harm Current [nA]	181	48.8	12.7
5	Thickness [μm]	303	152	75.9
	Length [μm]	15770	11150	7880
	Third Harm Current [nA]	353	95.2	24.8

The importance of varying the actuation area can already be seen. For γ=0.2, V=1 and γ=0.05, V = 2 the length and thickness are identical, but the output current is higher for the larger voltage. This means that changing the actuation length can produce higher voltages with similar cantilever dimensions.

These results show that output currents as high as 353nA can be achieved at lower frequencies, but the necessary cantilever dimensions are extremely large – the beam must be more than 1.5cm long. Rather than seek the largest possible signal, it makes more sense to choose a reasonable minimum current and then choose reasonable dimensions from there. For 5V (rms) actuation, the third harmonic component from the lock-in is <1mV for frequencies <15kHz, and this voltage is even lower with for smaller actuation voltages. With the improved isolation, 1mV corresponds to 1.45nA of parasitic current. A reasonable measurable signal must be higher than this value.

Long cantilevers also require larger caps and longer distances between electrodes. This increases the parasitic capacitance of the leak paths and decreases isolation. Therefore, the smallest possible cantilever that meets the minimum signal requirements was chosen. This

cantilever will have a thickness of 12.2μm, actuation ratio of 0.05, length of 3160μm, and actuation voltage of 2V(rms).

While the resonance frequency and output current of this design are improved, the quality factor is actually higher at low pressures. This has both problems and benefits. Since the intrinsic losses (those that are independent of pressure) are lower, the theoretical lower sensing limit is now around 10^{-6} Torr. However, the resonance peak width is still very narrow at lower pressures, down to a mHz at the lower limit. This is illustrated in Figure 6-3 below.

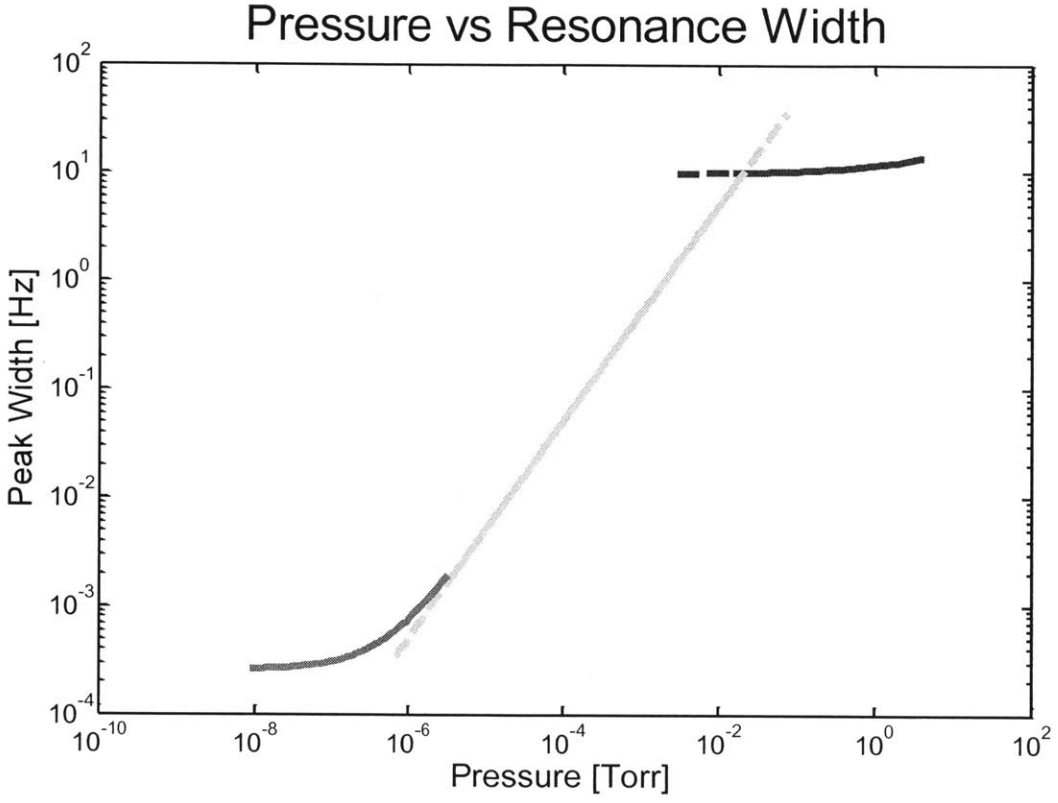

Figure 6-3 - Relationship between pressure and peak width for new design

While this design did not lower the quality factor, it did not change it much in the upper range and therefore the new peak widths are comparable to the previous design. While not ideal, it should be possible to narrow the frequency sweep range once resonance has been located at higher pressures. Additionally, the frequency shift is much lower at high Q, so the new resonance peak should be close to the previously measured value.

To verify the displacements, the full Euler-Bernoulli beam solutions were plotted, as shown in Figure 6-4. While the displacement for the dynamic point load is significantly higher

than the static case, it must be mentioned that this is both an overestimate to provide an upper bound, and still below $g_0/3$, the pull-in displacement.

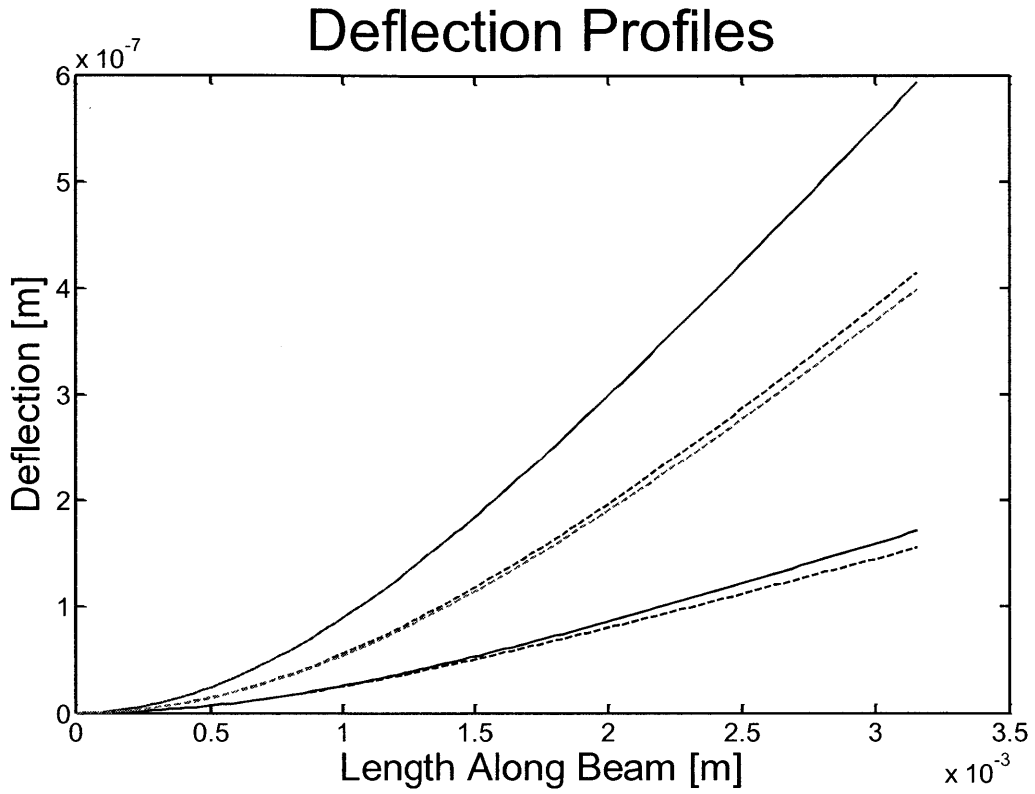

Figure 6-4 - Deflection of cantilever beams under various loading conditions. Solid lines are solutions to the Euler-Bernoulli equation, dashed lines are static solutions using basic beam theory with a constant force (no voltage dependence). Blue indicates a point load at the end, red is the realistic situation with a distributed load over the actuation region, and black is a fully distributed load. The total force applied is the same across all loading conditions, so the distributed load for the black curves was l/L times the actual distribution

New device dimensions and critical parameters are summarized in Table 6-3 below.

Table 6-3 - Final dimensions and critical parameters for optimized device

Parameter		Value
Length (L)		3160μm
Width (w)		630μm
Thickness (t)		12.2μm
Gap (g_0)		2.5μm
Actuation Voltage (V_{AC})		2V
Hole spacing ($2r_c$)		6.3μm
Frequency (ω_0)		9.94rad/s
Frequency (f)		1.58kHz
Third Harmonic Current (i_3)		1.59nA
Max Deflection (u_{max})	Static Point Load: (used for optimization)	0 .415μm
	Dynamic Point Load: (upper bound)	0.594μm

6.5 Summary of changes

A new design has been proposed that makes changes in the fabrication process and device dimensions to remove many of the problems affecting the original design. Improved bonding will reduce peeling and shorting at the edges. Mask changes to add isolation trenches and decrease the cap size will decrease the parasitic currents that currently mask the desired signal from the resonator. Changes to the dimensions will lower the resonance frequency so that the signal can be properly amplified rather than using a resistor, and have the added benefit of increasing the theoretical sensing range. Finally, metal contacts will remove the rectifying behavior at the contact pads. These changes are summarized in Table 6-4 below.

Table 6-4 – Summary of changes in new design

Change	Impact on Parasitic Currents	Impact on Signal	Other comments
Improved bonding	• No effect by itself, but allows for better isolation	• None	• Removes edge peeling
Metal Contacts	• None	• Higher AC signal allows **7x** increase in output third harmonic	• No rectification effect
Improved Isolation	• Decreases parasitic currents by **~6x** (depending on frequency)	• None	
Lower Resonance Frequency	• Slightly more isolation at lower frequencies, but insignificant compared to isolation	• Lower signal by **14.5x**	• Allows amplification • Increases lower sensing range to 10^{-6} Torr

References

[1] R. Bogue, "MEMS sensors: Past, present and future," *Sensor Review*, vol. 27, no. 1, pp. 7-13, 2007.

[2] F. R. Blom, S. Bouwstra, M. Elwenspoek, and J. H. J. Fluitman, "Dependence of the quality factor of micromachined silicon beam resonators on pressure and geometry," *Journal of Vacuum Science & Technology B: Microelectronics and Nanometer Structures*, vol. 10, no. 1, p. 19, Jan. 1992.

[3] P. Bruschi, A. Nanninim, and F. Pieri, "Electrical measurements of the quality factor of microresonators and its dependence on the pressure," *Sensors and Actuators A: Physical*, vol. 114, no. 1, pp. 21-29, 2004.

[4] A. I. Akinwande, L.-Y. Chen, L. F. Velasquez-Garcia, X. Wang, and K. Teo, "A Micro Ionizer for Portable Mass Spectrometers using Double-gated Isolated Vertically Aligned Carbon Nanofiber Arrays," *2007 IEEE International Electron Devices Meeting*, pp. 843-846, Dec. 2007.

[5] C.-J. Lu et al., "First-generation hybrid MEMS gas chromatograph," *Lab on a Chip*, vol. 5, no. 10, pp. 1123-1131, 2005.

[6] N. V. Lavrik, M. J. Sepaniak, and P. G. Datskos, "Cantilever transducers as a platform for chemical and biological sensors," *Review of Scientific Instruments*, vol. 75, no. 7, p. 2229, 2004.

[7] K. Wang, A.-chew Wong, S. Member, and C. T. Nguyen, "VHF Free – Free Beam High- Q," vol. 9, no. 3, pp. 347-360, 2000.

[8] C. T. Nguyen and R. T. Howe, "An Integrated CMOS Micromechanical Resonator High-Oscillator," vol. 34, no. 4, pp. 440-455, 1999.

[9] H. J. Mamin and D. Rugar, "Sub-attonewton force detection at millikelvin temperatures," *Applied Physics Letters*, vol. 79, no. 20, p. 3358, 2001.

[10] K. Jensen, K. Kim, and a Zettl, "An atomic-resolution nanomechanical mass sensor.," *Nature nanotechnology*, vol. 3, no. 9, pp. 533-7, Sep. 2008.

[11] K. L. Ekinci, X. M. H. Huang, and M. L. Roukes, "Ultrasensitive nanoelectromechanical mass detection," *Applied Physics Letters*, vol. 84, no. 22, p. 4469, 2004.

[12] S. Bianco et al., "Silicon resonant microcantilevers for absolute pressure measurement," *Journal of Vacuum Science & Technology B: Microelectronics and Nanometer Structures*, vol. 24, no. 4, p. 1803, 2006.

[13] M. Cocuzza, I. Ferrante, A. Ricci, E. Giuri, and L. Scaltrito, "Silicon laterally resonant microcantilevers for absolute pressure measurement with integrated actuation and readout," *Journal of Vacuum Science & Technology B*, pp. 541-550, 2008.

[14] J. Melin, P. Enoksson, T. Corman, and G. Stemme, "A low-pressure encapsulated deep reactive ion etched resonant pressure sensor electrically excited and detected using 'burst' technology," *J. Micromech. Microeng.*, vol. 10, pp. 209-217, 2000.

[15] C. J. Welham, J. W. Gardner, and J. Greenwood, "A laterally driven micromachined resonant pressure sensor," *Sensors And Actuators A*, vol. 52, pp. 86-91, 1996.

[16] J. C. Greenwood and D. W. Satchel, "Miniature silicon resonant pressure sensor," *IEEE Proceedings*, vol. 135, no. 5, pp. 369-372, 1988.

[17] J. C. Greenwood, "Etched Silicon Vibrating Sensor," *J. Phys. E: Sci. Instrum.*, vol. 17, pp. 4-6, 1984.

[18] G. Stemme, "Resonant Silicon Sensors," *J. Micromech. Microeng.*, vol. 1, no. 1 & 991, pp. 113-125, 1991.

[19] E. Stemme and G. Stemme, "A balanced dual-diaphragm resonant pressure sensor in silicon," *IEEE Transactions on Electron Devices*, vol. 37, no. 3, pp. 648-653, Mar. 1990.

[20] R. A. Buser and N. F. D. Rooij, "Very High Q-factor Resonators in Monocrystalline Silicon," *Sensors and Actuators,*, vol. 23, pp. 323-327, 1990.

[21] S. Pourkamali, a. Hashimura, R. Abdolvand, G. K. Ho, a. Erbil, and F. Ayazi, "High-Q single crystal silicon HARPSS capacitive beam resonators with self-aligned sub-100-nm transduction gaps," *Journal of Microelectromechanical Systems*, vol. 12, no. 4, pp. 487-496, Aug. 2003.

[22] C. Zuo, J. Van der Spiegel, and G. Piazza, "1.05-GHz CMOS oscillator based on lateral-field-excited piezoelectric AlN contour- mode MEMS resonators.," *IEEE transactions on ultrasonics, ferroelectrics, and frequency control*, vol. 57, no. 1, pp. 82-7, Jan. 2010.

[23] W. P. Eaton and J. H. Smith, "Micromachined pressure sensors : review and recent developments," *Smart Mater. Struct.*, vol. 6, pp. 530-539, 1997.

[24] F. A. Ghavanini, H. Rödjegård, and P. Enoksson, "An easy-to-implement method for evaluation of capacitive resonant sensors," *Journal of Micromechanics and Microengineering*, vol. 16, no. 6, p. S156-S160, 2006.

[25] K. Y. Yasumura et al., "Quality factors in micron- and submicron-thick cantilevers," *Journal of Microelectromechanical Systems*, vol. 9, no. 1, pp. 117-125, Mar. 2000.

[26] K. Kokubun, M. Hirata, M. Ono, H. Murakami, and Y. Toda, "Unified formula describing the impedance dependence of a quartz oscillator on gas pressure," *J. Vac. Sci. Technol. A*, vol. 5, no. 4, 1987.

[27] D. J. Bell, T. J. Lu, N. a Fleck, and S. M. Spearing, "MEMS actuators and sensors: observations on their performance and selection for purpose," *Journal of Micromechanics and Microengineering*, vol. 15, no. 7, p. S153-S164, Jul. 2005.

[28] S. M. Spearing, "MATERIALS ISSUES IN MICROELECTROMECHANICAL SYSTEMS (MEMS)," *Acta Materialia*, vol. 48, pp. 179-196, 2000.

[29] "Piezoceramic Materials Specifications." [Online]. Available: http://www.piezotechnologies.com/materialssheet.htm. [Accessed: 12-Jan-2012].

[30] R. C. Batra, M. Porfiri, and D. Spinello, "Review of modeling electrostatically actuated microelectromechanical systems," *Smart Materials and Structures*, vol. 16, no. 6, p. R23-R31, Dec. 2007.

[31] P. R. Scheeper et al., "A New Measurement Microphone Based on MEMS Technology," vol. 12, no. 6, pp. 880-891, 2003.

[32] M. Bao and H. Yang, "Squeeze film air damping in MEMS," *Sensors and Actuators A: Physical*, vol. 136, no. 1, pp. 3-27, May 2007.

[33] X. Zhang et al., "Characterization of silicon wafer bonding for Power MEMS applications," *Sensors And Actuators A*, vol. 103, pp. 1-8, 2003.

Appendix A: Stationary Beam Bending Solution

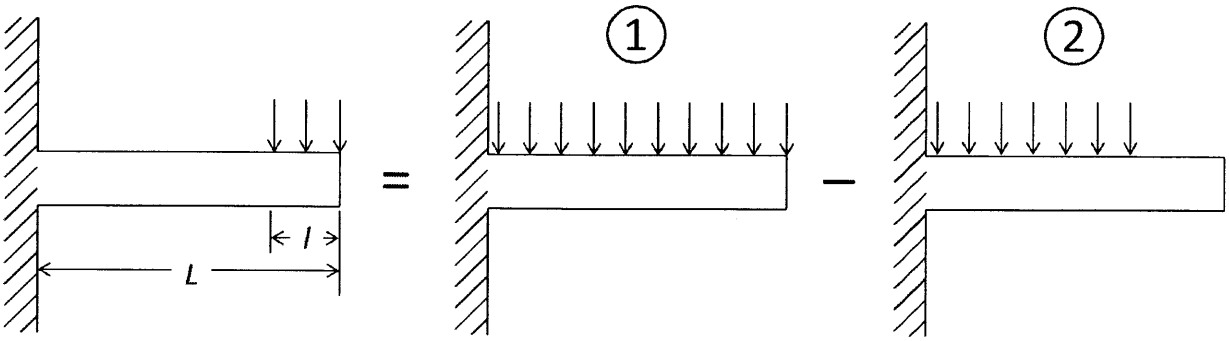

Figure 0-1 Visualization of superposition used to determine beam deflection

Case 1: Uniform load F_e over entire length L

$$u_1(x) = -\frac{F_e x^2(6L^2 - 4xL + x^2)}{24EI}$$

Case 2: Uniform load F_e over length $(L - l)$, angle and displacement continuous at $x = (L - l)$

$$u_2(x) = \begin{cases} -\dfrac{F_e x^2(6(L-l)^2 - 4x(L-l) + x^2)}{24EI}, & x < L - l \\ -F_e\left(\dfrac{(L-l)^3}{6EI}(x - (L-l)) + \dfrac{(L-l)^4}{8EI}\right), & x \geq L - l \end{cases}$$

Superposition: $u(x) = u_1(x) - u_2(x)$ (with considerable simplification)

$$u(x) = \begin{cases} -\dfrac{F_e x^2 l}{12EI}(6L - 3l - 2x), & x < L - l \\ -\dfrac{F_e}{24EI}(x^4 - 4x^3L + 6x^2L^2 + 4x(L-l)^3 - (L-l)^4), & x \geq L - l \end{cases}$$

This allow us to determine the deflection at the tip, u_{max}

$$u_{max} = \frac{-F_e l}{24EI}(8L^3 - 6L^2 l + l^3)$$

Appendix B: Fabrication Process

MEMS Resonant Pressure Sensor Process Flow							
Purpose: To fabricate an encapsulated cantilever that measures pressure via changes in air damping and resonant frequency							
Starting Materials: Two DSP 6" SOI wafers (650um handle Si, 1um oxide, 15um device layer) with 100nm thermal oxide on both sides							
Wafer 1,2,3							
Feature	**Step#**	**Lab**	**Process step**	**Machine**	**Chemicals**	**Color**	**Comments**
Alignment marks	1	TRL	HMDS	HMDS-TRL		green	thin resist recipe
	2	TRL	Spin on resist (front)	coater	OCG 825-20CS	green	1 um, positive resist
	3	TRL	prebake	oven		green	90C, 15 min
	4	TRL	expose front	EV1		green	**Resonator_Alignment** mask
	5	TRL	develop	photo-wet	OCG-934	green	
	6	TRL	postbake	oven		green	90C, 30 min
	7	ICL	front oxide etch	AME5000		green	Chamber A, 0.1 um oxide etch
	8	ICL	front Si etch	AME5000		green	Chamber B, 0.25 um Si etch
	9	TRL	ash resist	asher-TRL		green	
	10	TRL	piranha + rinse + spin dry	ah2	sulfuric acid, peroxide	green	piranha clean
	11	TRL	HMDS	HMDS-TRL		green	thin resist recipe
	12	TRL	Spin on resist (back)	coater	OCG 825-20CS	green	1 um, positive resist
	13	TRL	prebake	oven		green	90C, 30 min
	14	TRL	expose back	EV1		green	**Resonator_Alignment** mask
	15	TRL	develop	photo-wet	OCG-934	green	
	16	TRL	postbake	oven		green	90C, 30 min
	17	ICL	back oxide etch	AME5000		green	Chamber A, 0.1 um oxide etch
	18	ICL	back Si etch	AME5000		green	Chamber B, 0.25 um Si etch
	19	TRL	ash resist	asher-TRL		green	
	20	TRL	piranha + rinse + spin dry	ah2	sulfuric acid, peroxide	green	piranha clean
Wafer 1							
Feature	**Step#**	**Lab**	**Process step**	**Machine**	**Chemicals**	**Color**	**Comments**
Cantilever electrode	21	TRL	HMDS	HMDS-TRL		green	thin resist recipe
	22	TRL	Spin on resist (front)	coater	OCG 825-20CS	green	1 um, positive resist
	23	TRL	prebake	oven		green	90C, 15 min
	24	TRL	Spin on resist (back)	coater	OCG 825-20CS	green	1 um, positive resist
	25	TRL	prebake	oven		green	90C, 30 min
	26	TRL	expose front	EV1		green	**Cantilever_Electrode** mask
	27	TRL	develop	photo-wet	OCG-934	green	
	28	TRL	postbake	oven		green	90C, 30 min
	29	Innovion	ion implantation			green	Send to Innovion for dose = 10^20/cm^3 boron
	30	TRL	ash resist	asher-TRL		green	
	31	TRL	double piranha + rinse + spin dry	ah2	sulfuric acid, peroxide	green	double piranha clean
	32	TRL	Anneal dopants	TubeB3		green	
	33	TRL	BOE	ah2	BOE	green	2 min, for oxide removal
	34	ICL	Pre-metal clean	pre-metal		green	
	35	ICL	PECVD oxide (front)	Concept1		green	3 um PECVD oxide

	36	TRL	Densify oxide	TubeB3		green	
	37	ICL	CMP	diel-CMP		green	leave 2.5 um thick oxide (check with metrology)
	38	ICL	double piranha+rinse+spin dry	pre-metal		green	double piranha clean
Cantilever + holes	39	TRL	HMDS	HMDS-TRL		green	thin resist recipe
	40	TRL	Spin on resist (front)	coater	OCG 825-20CS	green	1 um, positive resist
	41	TRL	prebake	oven		green	90C, 15 min
	42	TRL	Spin on resist (back)	coater	OCG 825-20CS	green	1 um, positive resist
	43	TRL	prebake	oven		green	90C, 30 min
	44	TRL	expose front	EV1		green	**Cant_Plus_Holes** mask
	45	TRL	develop	photo-wet	OCG-934	green	
	46	TRL	postbake	oven		green	90C, 30 min
	47	ICL	front oxide etch	AME5000		green	Chamber A, 2.5 um oxide etch
	48	TRL	front Si etch	STS2/3		green	15 um Si etch, oxide etch stop
	49	TRL	ash resist	asher-TRL		green	
	50	TRL	piranha + rinse + spin dry	ah2	sulfuric acid, peroxide	green	piranha clean
Wafer 2							
Feature	**Step#**	**Lab**	**Process step**	**Machine**	**Chemicals**	**Color**	**Comments**
Cap electrode	51	TRL	HMDS	HMDS-TRL		green	thin resist recipe
	52	TRL	Spin on resist (front)	coater	OCG 825-20CS	green	1um, positive resist
	53	TRL	prebake	oven		green	90C, 15 min
	54	TRL	Spin on resist (back)	coater	OCG 825-20CS	green	1um, positive resist
	55	TRL	prebake	oven		green	90C, 30 min
	56	TRL	expose front	EV1		green	**Actuation_Electrode** mask
	57	TRL	develop	photo-wet	OCG-934	green	
	58	TRL	postbake	oven		green	90C, 30 min
	59	Innovion	ion implantation			green	Send to Innovion for dose = 10^20/cm^3 boron
	60	TRL	ash resist	asher-TRL		green	
	61	TRL	double piranha + rinse + spin dry	acidhood/ah2	sulfuric acid, peroxide	green	double piranha clean
	62	TRL	Anneal dopants	TubeB3		green	
	63	TRL	BOE	ah2	BOE	green	2 min, for oxide removal
	64	ICL	pre-metal clean	pre-metal		green	
	65	ICL	PECVD oxide (front)	Concept1		green	3 um PECVD oxide
	66	TRL	Densify oxide	TubeB3		green	
Nested mask	67	TRL	HMDS	HMDS-TRL		green	thin resist recipe
	68	TRL	Spin on resist (front)	coater	OCG 825-20CS	green	1um, positive resist
	69	TRL	prebake	oven		green	90C, 15 min
	70	TRL	Spin on resist (back)	coater	OCG 825-20CS	green	1um, positive resist
	71	TRL	prebake	oven		green	90C, 30 min
	72	TRL	expose front	EV1		green	**Nested** mask
	73	TRL	develop	photo-wet	OCG-934	green	
	74	TRL	postbake	oven		green	90C, 30 min
	75	TRL	oxide etch (BOE)	ah2	BOE	green	1um deep thermal oxide etch
	76	TRL	piranha + rinse + spin dry	ah2	sulfuric acid, peroxide	green	piranha clean
Cap cavity	77	TRL	HMDS	HMDS-TRL		green	thin resist recipe

	78	TRL	Spin on resist (front)	coater	OCG 825-20CS	green	1 um, positive resist
	79	TRL	prebake	oven		green	90C, 15 min
	80	TRL	Spin on resist (back)	coater	OCG 825-20CS	green	1 um, positive resist
	81	TRL	prebake	oven		green	90C, 30 min
	82	TRL	expose front	EV1		green	**Cavity** mask
	83	TRL	develop	photo-wet	OCG-934	green	
	84	TRL	postbake	oven		green	90C, 30 min
	85	TRL	Si etch	STS2/3		green	15 um Si etch, oxide etch stop
	86	TRL	oxide etch (BOE)	ah2	BOE	green	2um through oxide etch
	87	TRL	piranha + rinse + spin dry	ah2	sulfuric acid, peroxide	green	piranha clean
	88	TRL	Si etch	STS2/3		green	50 um deep Si etch
	89	TRL	BOE	ah2	hydrofluoric acid	green	remove oxide
Wafers 1, 2							
Feature	**Step#**	**Lab**	**Process step**	**Machine**	**Chemicals**	**Color**	**Comments**
Bonding wafers	90	TRL	ash wafers	TRL-asher		green	1 hour each wafer
	91	TRL	piranha + rinse	ah2	sulfuric acid, peroxide	green	piranha clean
	92	TRL	RCA clean *without* HF dip (only wafer 1)	RCA		green	
	93	TRL	RCA clean *with* HF dip (only wafer 2)	RCA		green	
	94	TRL	Align wafers	EV620		green	
	95a	TRL	Silicon direct bonding	EV620		green	(while EV501 down)
	95b	TRL	Fusion bonding	EV501		green	(intended process step)
	96	TRL	Anneal	TubeB3		green	
Wafers 1, 2							
Feature	**Step#**	**Lab**	**Process step**	**Machine**	**Chemicals**	**Color**	**Comments**
Via	97	TRL	HMDS	HMDS-TRL		green	thick resist recipe
	98	TRL	Spin on resist (front)	coater	AZ4620 resist	green	10um, positive resist
	99	TRL	prebake	oven		green	90C, 30 min
	100	TRL	Spin on resist (back)	coater	AZ4620 resist	green	10um, positive resist
	101	TRL	prebake	oven		green	90C, 30 min
	102	TRL	Spin on resist (back)	coater	AZ4620 resist	green	10um, positive resist (20um total)
	103	TRL	prebake	oven		green	90C, 30 min
	104	TRL	expose (back)	EV1		green	**Via** mask 15s on, 15s off, repeat 8 times
	105	TRL	develop	photo-wet	AZ440 developer	green	
	106	TRL	postbake	oven		green	90C, 30 min
	107	TRL	Mount on quartz wafer (topside down)	coater		green	
	108	TRL	Si etch back	STS2/3		green	510 um Si etch, oxide etch stop
	109	TRL	acetone dismount of wafer handle	photo-wet	acetone	green	
	110	TRL	ash resist	asher-TRL		green	
	111	TRL	piranha + rinse + spin dry	ah2	sulfuric acid, peroxide	green	piranha clean

Wafers 1, 2							
Feature	**Step#**	**Lab**	**Process step**	**Machine**	**Chemicals**	**Color**	**Comments**
Define cap	112	TRL	HMDS	HMDS-TRL		green	thick resist recipe
	113	TRL	Spin on resist (front)	coater	AZ4620 resist	green	10um, positive resist
	114	TRL	prebake	oven		green	90C, 30 min
	115	TRL	Spin on resist (front)	coater	AZ4620 resist	green	10um, positive resist (20um total)
	116	TRL	prebake	oven		green	90C, 30 min
	117	TRL	Spin on resist (back)	coater	AZ4620 resist	green	10um, positive resist
	118	TRL	prebake	oven		green	90C, 30 min
	119	TRL	expose front	EV1		green	**Expose_Electrodes** mask 15s on, 15s off, repeat 8 times
	120	TRL	develop	photo-wet	AZ440 developer	green	
	121	TRL	postbake	oven		green	90C, 30 min
	122	TRL	Si etch front	STS2/3		green	510 um Si etch, oxide etch stop
	123	TRL	ash resist	asher-TRL		green	
Wafers 1, 2							
Feature	**Step#**	**Lab**	**Process step**	**Machine**	**Chemicals**	**Color**	**Comments**
Dice and release	124	ICL	Dice wafers	Diesaw		red	
	125	TRL	piranha + rinse + spin dry	ah2	sulfuric acid, peroxide	red	piranha clean
	126	TRL	oxide etch (BOE)	acidhood	BOE	red	Release cantilever, ~5um etch
	127	TRL?	soak in ethanol			red	necessary for crit pt dry
	128	Whitehead	Critical point dry			red	Whitehead Institute